UNIVERSITÀ DEGLI STUDI DI CATANIA
FACOLTÀ DI SCIENZE MATEMATICHE, FISICHE E NATURALI
DOTTORATO DI RICERCA IN FISICA

CLAUDIA AGLIOZZO

LUMINOUS BLUE VARIABLE STARS: EXPLORING THE MASS-LOSS HISTORY THROUGH A MULTIWAVELENGTH ANALYSIS OF THEIR EJECTA

PH.D. THESIS

Supervisor:
Prof. F. Leone

Tutor:
Doct. G. Umana
Doct. C. Trigilio

Coordinator:
Prof. F. Riggi

XXV CICLO (2009-2012)

Ai mie cari nonni

Contents

List of Tables

Introduction

Massive stars play a fundamental role in the evolution of galaxies. They are *major contributors to interstellar UV radiation* and, via their strong stellar winds, provide *enrichment of processed material* (gas and dust) and *mechanical energy to the interstellar medium*. Despite their importance, the details of post-Main Sequence (MS) evolution of massive stars are still poorly understood. Recent evolutionary models suggest that Luminous Blue Variable (LBV) stars and related transition objects may play a key role in massive star evolution, representing a crucial phase during which a star loses most of its H envelope (Lamers & Nugis 2002).

LBV stars are intrinsically bright objects, exhibiting different kinds of photometric and spectroscopic variabilities. They are massive post-MS stars, characterized by intense mass-loss rates, which can also occur in the form of eruptive events. As a result, they are often surrounded by extended, dusty circumstellar nebulae. Although eruptive events have been witnessed very rarely (i.e., η Carinae and P Cygni) the presence of these nebulae in most of the known objects suggests that these are a common aspect of the LBV behaviour (Weis 2008). There are, however, many aspects of the LBV phenomenon that are not completely understood. Among these are the total mass lost during the LBV phase (a key parameter necessary to test evolutionary models), the origin and shaping of the LBV nebulae (LBVNe), and how the mass-loss behaviour (single versus multiple events, bursts) is related to the physical parameters of the central object.

Humphreys & Davidson (1994) and later Smith & Owocki (2006) have suggested that eruptive episodes, which must form the bulk of a LBVN, are *metallicity independent*. If this is true, LBVs may have had a role in the evolution of the early Universe, when massive stars would have been more numerous than in the present epoch, and may have provided processed material and dust for future generations of stars.

More recently, it has also been pointed out that LBVs might be *direct Supernovae*

(SNe) *progenitors* (Kotak & Vink 2006; Smith et al. 2008), enhancing their importance in the framework of stellar evolution.

LBVs have also been considered as possible *dust producers* in high-redshift galaxies (Gall, Hjorth, & Andersen 2011), where the significant amount of dust observed in the sub-mm remains as yet an unanswered question. To explain the observations, a fast and efficient dust production mechanism is needed and, together with Core-Collapse Supernovae (CCSNe) and Asymptotic Giant Branch (AGB) stars, LBVs are promising channels for producing dust in the early Universe (Gall, Hjorth, & Andersen 2011).

Finally, LBVs could be *cosmological distance indicators* (Wolf 1989), thanks to the relationship between their variability amplitude and luminosity.

All these possibilities make LBVs important and fascinating objects to study.

The evolution of massive stars is influenced by the mass-loss during their lifetime, which also determines the stellar remnant (neutron star, black hole, or no remnant at all, Heger et al. 2003). Also the LBV evolution is strongly influenced by the mass-loss which the star undergoes during its post-MS phase.

The mass-loss archaeology of the central object can be recovered from an analysis of its associated nebula. A successful approach is based on a synergistic use of different techniques, at different wavelengths, that allows one to analyse the several emitting components coexisting in the nebula (Umana et al. 2011a). In particular, a detailed comparison of the optical, IR and radio emissions provide estimates of both ionized gas and dust masses and allow us to identify morphological differences in the maps which can be associated with mass-loss behaviour during the LBV phase (Buemi et al. 2010; Umana et al. 2010).

Some galactic LBVNe have been recently studied following this multi-wavelength approach (Umana et al. 2011a), aimed at tracing both the gas and the dust components coexisting typically in LBVNe. Among the most interesting aspects highlighted in these studies, there are: the morphology of the gas and the dust, which can be differently distributed (IRAS 18576+034, Buemi et al. 2010); the chemistry in the nebula, which can be rich in complex molecules, such as Polycyclic Aromatic Hydrocarbons (PAHs) (e.g. HD 168625, Umana et al. 2010), evidence that dust can survive despite the hostile environment due to the UV radiation from the star.

LBVs are quite rare objects: a census of known confirmed and candidate LBVs reports 35 objects in our Galaxy and 25 in the Magellanic Clouds (Clark, Larionov, & Arkharov

2005; van Genderen 2001). Hence our knowledge of LBVNe is still very limited due in part to the small number of known LBVs and in part to the short lifetime ($t \sim 10^{-5} - 10^{-4}$ yr) of the LBV phase. Despite this, the characterization of LBVNe is fundamental to understand the evolution of massive stars.

Adopting the multiwavelength approach mentioned above, we have selected a subsample of known LBVs and candidate LBVs (cLBVs) as follows.

We have chosen a galactic cLBV, namely G79.29+9.46, for which a huge amount of data at different wavelengths are available in the archives and new high-resolution, high-sensitivity observations were scheduled at the Expanded Very Large Array (EVLA) (P.I. Umana G.) during the first year of this PhD program. With its properties, this object appeared to be a good template for studying other LBVs.

To extend the study of the LBV phenomenon in environments different from the galactic one, i.e. in galaxies with different metallicity, we have searched in the data archive for LBVNe in the Large Magellanic Cloud (LMC), which is the nearest galaxy (with an accepted distance of ~ 48.5 kpc) and with half the solar metallicity ($Z \sim 0.5 Z_{\odot}$). We found that for LBVs in the LMC very few observations were performed so far in the the mid-IR wavelengths, while no information in the radio were available at all. However, evidence of extended nebulae around LBVs and cLBV in the LMC were reported from a study in the optical. Weis (2003) and Weis, Duschl, & Bomans (2003) performed high-resolution observations of 9 LBVs and cLBV in the LMC with the Hα filter using the *Hubble Space Telescope* and the EMMI instrument at ESO. In particular, they found that 5 of these objects show a very well defined shell in Hα, with sizes in the range 5" $-$ 18", indicating the presence of a nebula around them.

Based on these studies we have selected a group of LVBNe that could be detected at radio wavelengths (which allow us to probe the properties of the ionized gas) through the estimation of the radio free-free emission from the observed hydrogen Hα recombination-line. Hence first radio observations of a small sample of LBVs in the radio have been obtained with the Australia Telescope Compact Array (ATCA) during this PhD program in the 3+6 cm band (P.I. Agliozzo C.). Further higher-resolution observations of the detected systems have been performed in January 2012 in the 1.5 cm band (P.I. Agliozzo C.). In this work we present the first radio observations of four LBVNe in the LMC, namely: cLBVs S61 and S119, plus LBVs R127 and R143.

The thesis is organized as follows:

In **Chapter 1** we present a review of the literature: LBVs are described in terms of their post-MS evolutionary track and their observed properties. The most important

mass-loss mechanisms proposed in the literature are discussed as well as the open issues. Finally a section is dedicated to the motivations of this thesis.

After this general introduction, we describe the investigations performed in this work. The thesis is then organized in two parts:

Part 1 is dedicated to the study of the galactic cLBV G79.29+0.46, for which we obtained initial observations at the Expanded Very Large Array (EVLA), followed by observations at the Green Bank Telescope (GBT). These works are discussed in **Chapter 2**. First results of these studies have already been published in Umana et al. (2011b). **Chapter 3** contains a study performed with archival data, at different wavelengths in the IR domain, that permit us to compare different emitting components in the ejecta and to derive physical parameters related to the dust and the gas in the nebula. A model obtained with the photo-ionization code CLOUDY is also discussed.

Part 2 addresses the study of four LBVs in the LMC (S61, S119, R127 and R143). **Chapter 4** contains the first radio detection of LBV nebulae in the LMC obtained with Australia Telescope Compact Array (ATCA) observations. This work has been published in MNRAS (Agliozzo et al. 2012). In **Chapter 5** further high-resolution radio observations are presented, together with a morphological and photometric comparison with the *Hubble Space Telescope* (*HST*) optical images.

We present out final remarks in the **Discussion and Conclusions**.

Chapter 1

Luminous Blue Variable stars

The Luminous Blue Variable stars (LBVs) are evolved, luminous ($L \sim 10^5 - 10^{6.3}\,L_\odot$), massive ($M_{ZAMS} > 22\,M_\odot$) and hot ($T \sim 7000 - 35000\,K$) stars, characterised by spectroscopic and photometric variability, and by moderate or extreme mass-loss ($\dot{M} \sim 10^{-6} - 10^{-4}\,M_\odot\,yr^{-1}$). As a result of the mass-loss, these stars are surrounded by a large mass (some $M_\odot$) of dust and gas, forming spectacular and huge nebulae (typical sizes range from 0.2 to 2 pc). A review of LBVs was presented first by Humphreys & Davidson (1994) and later by van Genderen (2001) and Vink (2009).

The ejection of the outer envelopes of the star is a necessary condition before they evolve as Wolf-Rayet stars (WRs). In fact, it has been believed that LBVs are progenitors of the hot stars known as WRs, whose destiny is to explode as SN (type Ib/c), but recently it has been proposed that LBVs may skip the WR stage and experience directly the SN event (Kotak & Vink 2006; Vink et al. 2008).

Famous LBVs are η Carinae (η Car), P Cygni (P Cyg) and S Doradus (S Dor).
S Dor is widely considered the prototype of photometric and spectroscopic variability and many LBVs are often referred as *S Dor variables* for this reason. Conversely, P Cyg and η Car are the only two case of eruptive events witnessed in our Galaxy. They suffered such violent eruptions that were observed with naked-eyes, P Cyg in AD 1600 and η Car in the XIX century.

In this chapter we briefly review the LBVs in term of their evolutionary track on the Herzsprung-Russel (H-R) diagram and we describe the physical and observational properties of both the star and the ejected nebula, the open issues related to the mass-loss mechanism and we report the current proposed explanation for it. We also give a glimpse of the aspects that make these stars an intriguing and important object of study. Finally, we dedicate a section to the motivations of this thesis.

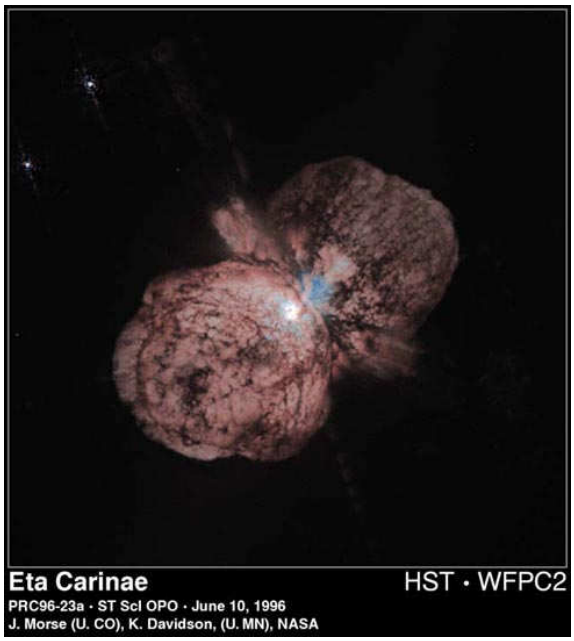

Figure 1.1: The Homunculus Nebula around η Car as seen with the *Hubble Space Telescope* in the optical light (Morse et al. 1998).

1.1 Evolutionary track on the H-R diagram

The evolution of massive stars is believed to be driven by mass-loss. In fact, the reduction of a star mass profoundly affects the size of its convective core, its core temperature, its angular momentum evolution, its luminosity as a function of time, and hence its evolutionary track on the H-R diagram and its MS lifetime (Chiosi & Maeder 1986; Smith & Owocki 2006).

As described in Conti & Frost (1976), the main steps in the life of a massive star can be represented with the the following scheme

$$O \rightarrow LBV \rightarrow WR \rightarrow SN$$

At the end of its MS life, when the convective core has exhausted the H-burning, the star begins to expand and becomes a blue supergiant with a radius $\sim 10^2\,R_\odot$ and an enhanced He and N surface abundance (Lamers & Nugis 2002). In the H-R diagram, the star moves to the right (cooler temperatures, till $T \sim 8 \times 10^3$ K), with moderate mass-loss (see Fig. 1.2).

At some point the star becomes unstable, because it approaches the limit for stability (the Eddington limit): the gravity can not contrast the radiation pressure and, as a consequence, the star suffers high mass-loss. This causes the star to move toward the warmer temperatures ($T \sim 3.5 \times 10^4$ K), until it temporarily stabilizes again. In the meanwhile, the rapid mass-loss increases the star L/M ratio, which reduces its stability. Therefore the

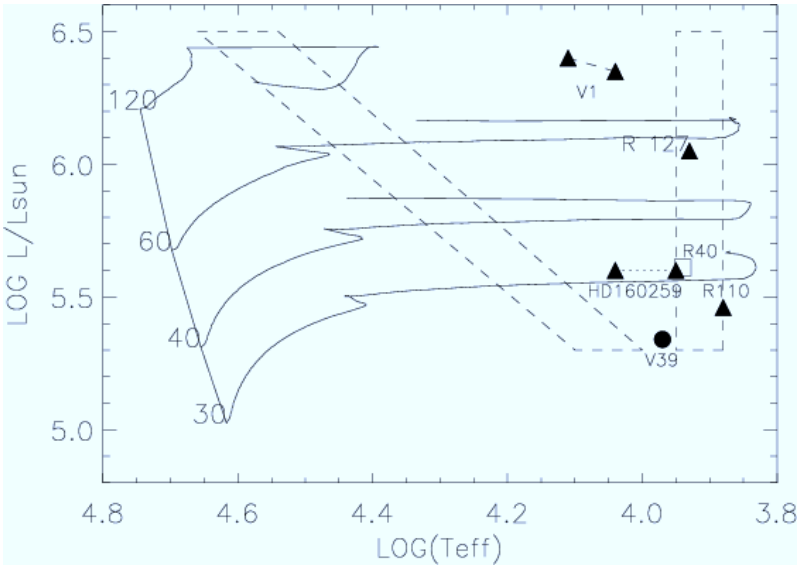

Figure 1.2: Evolutionary track for LBVs, from Herrero et al. (2010). There are marked the region occupied by LBVs during outburst (vertical box) and the one occupied by LBVs during visual minimum (slanted strip, both from Smith, Vink, & de Koter 2004).

instabilities soon recurs when the star evolves toward cooler temperatures again. At this point the star has become a LBV.

Empirically it was found that for the hottest stars, the luminosity limit for the stability depends not only on the mass, but also on the temperature. This new stability limit is an extension of the Eddington limit and in the H-R diagram can be represented by a locus known as "Humphreys and Davidson strip" (or even "S Dor variability strip", Humphreys & Davidson 1994, slanted line in Fig. 1.2 and 1.3).

Once the star has become a LBV, it has been believed that the star fluctuates in the H-R diagram around small temperature variations, at constant luminosity. These changes of the effective temperatures are only apparent. In fact, when the LBV approaches the limit for stability, it suffers enhanced mass-loss episodes ($\dot{M} \sim 10^{-5} - 10^{-4}\,\mathrm{M_\odot\,yr^{-1}}$). As a consequence, it forms an optically thick pseudo-photosphere, which absorbs the hot radiation from the star and re-emits it at longer wavelengths, causing an apparent temperature decreasing (*active state*). While the star declines toward the *quiescent state*, with more moderate mass-loss rate ($\dot{M} \sim 10^{-7} - 10^{-5}\,\mathrm{M_\odot\,yr^{-1}}$), the pseudo-photosphere previously formed becomes a circumstellar envelope that evolves from an optically thick to an optically thin nebula. Thus the star surface is again exposed and it appears hot ($T \sim 3.5 \times 10^4\,\mathrm{K}$) again (quiescent state).

After the LBV phase, when the star has ejected its H-envelope, the star contracts and becomes a WR ($M \sim 20\,\mathrm{M_\odot}$), with higher mass-loss rate ($\dot{M} > 10^{-5}\,\mathrm{M_\odot\,yr^{-1}}$) and higher wind velocity ($v_\infty \sim 10^3\,\mathrm{km\,s^{-1}}$, while for LBVs it is typically $v_\infty \sim 10^2\,\mathrm{km\,s^{-1}}$).

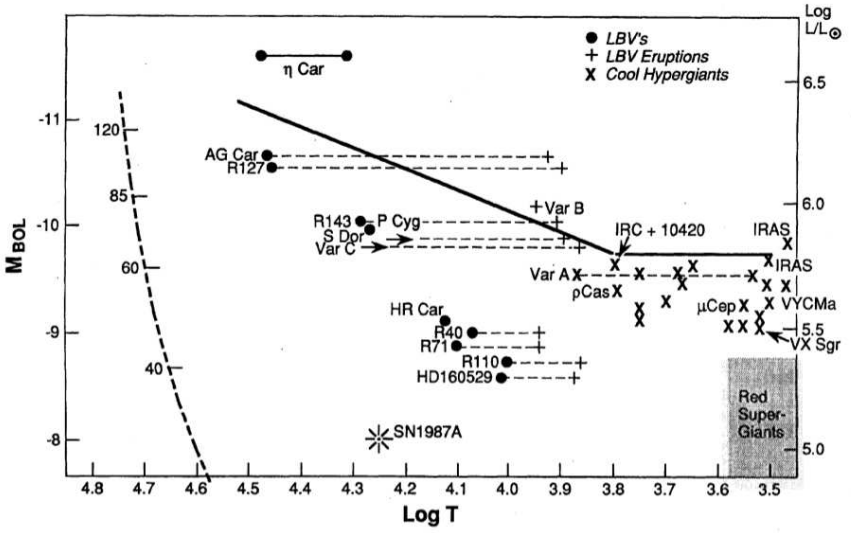

Figure 1.3: A schematic H-R diagram for the most luminous stars (Humphreys & Davidson 1994). The dashed lines represent observed transit in the H-R diagram of some LBVs, while the solid lines the empirical upper luminosity boundary.

However, as proposed by various authors (e.g. Kotak & Vink 2006; Smith et al. 2008; Vink 2009), LBVs may not be always traditional objects between O and WR stars and may suffer a final explosion during or at the end of the LBV phase (Vink 2009).

1.2 Observed properties

In this section we give a description of the stellar parameters changes during the LBV excursion in the H-R diagram.

1.2.1 Luminosities and Temperatures

The classical LBVs have $\log(L/L_{\odot})$ greater than 5.8, with bolometric magnitudes in the range M_{bol} -8 to -11. One of the most important properties of LBVs is their closeness[1] to the Eddington limit for stability against radiation pressure for their luminosities and current masses. Historically the Eddington luminosity L_e was defined as

$$L_e = \frac{4\pi GcM}{\kappa_F} \tag{1.1}$$

where κ_F is the opacity for electron scattering and the other symbols have their usual meaning.

The dimensionless Eddington parameter for electron scattering Γ_e is defined as the ratio between the outward radiation force and the inward gravity force:

$$\Gamma_e = \frac{L\sigma_e}{4\pi cGM} \tag{1.2}$$

[1] Due in part to the core evolution and in part to the mass-loss in precedent phases.

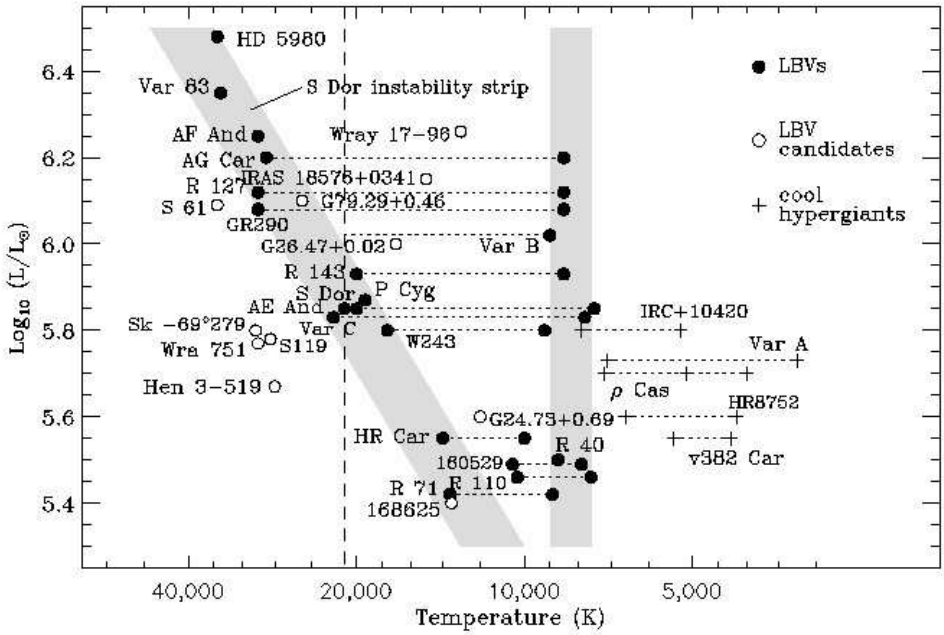

Figure 1.4: The LBVs in the H-R diagram. The shaded areas represent the S Dor instability strip (visual minimum, diagonal) and the position of the LBVs during outburst (vertical). The dashed vertical line at 21000 K indicates the bi-stability jump (described in Section 1.3), while the horizontal ones the observed transit of known LBVs. Figure in Vink et al. (2008) adapted from Smith et al. (2004).

where σ_e is the electron scattering cross-section. This ratio can not exceed unity, implying an upper limit to L/M.

LBVs are generally close to the Eddington limit, so radiation pressure reduces their stability.

To explain the observed behaviour of LBVs, Humphreys & Davidson (1984) proposed a *modified* Eddington limit, where they considered an opacity κ dependent on the effective temperature and on the density. Hence the luminosity is not independent of the temperature and in the H-R diagram the instability limit appears as a slanted line (the so-called *Humphreys and Davidson instability strip*).

The apparent changes of the effective temperature during the excursion between the quiescent (or else *visual minimum*) and active (*outburst* or *visual maximum*) states move in the range from 35000 K (corresponding to spectral type late O/early B) to 8000 K (spectral types A-F).

Fig. 1.4 shows known confirmed and candidate LBVs on the H-R diagram, with their transit (the dotted horizontal lines) between their quiescence and active states. The slanted band is the "S Dor instability strip", indicating the quiescent state, or visual minimum. The amplitude of the S Dor excursions (dashed horizontal lines) becomes larger with increasing luminosity: Wolf (1989) proposed hence that the most LBVs could be used as

cosmological distance indicators.

1.2.2 Photometric and Spectroscopic variability

One of the properties of LBVs is their variability at constant bolometric luminosity. Even though a general classification based on LBVs properties has not been defined as yet, it is possible to distinguish between at least three types of LBV, depending on the variability cycles and the visual magnitudes changes (Humphreys & Davidson 1994; Vink 2009):

(i) the *normal LBV variability cycles* (S Dor variables) with visual magnitudes changes of 1-2 magnitudes at constant luminosity (e.g. S Dor in the LMC), on timescales of years (short S Dor phases) to decades (long S Dor phases);

(ii) *eruptions* with visual magnitudes changes of 1-2 magnitudes or more, on timescales of 10-40 years. At visual maximum the star atmosphere is greatly expanded and the bolometric magnitude is unchanged. The visual brightening is due to a redshift of the UV radiation to the optical, caused by the pseudo-photosphere;

(iii) the *giant eruption* LBVs (e.g. η Car and P Cyg) with visual magnitudes changes of 3 magnitudes or more. This is the only case where the total bolometric luminosity increases.

Fig. 1.5 shows the visual light curve of η Car in the last five centuries. The peak of visual magnitude is the famous "Great Eruption", occurred between 1837-1860, when the object could be observed easily with naked eyes.

At the photometric variations also correspond variations in the spectra. At the visual minimum the spectrum is dominated by emission-lines of H, HeI, FeII and [FeII], resembling a hot supergiant, while at the visual maximum the FeII is weaker and the optically thick expanded atmosphere resembles a cool supergiant of spectral type A of F.

An important spectroscopic feature observed in the emission-lines of these objects is the P-Cygni profile, as shown in Fig. 1.6. In particular, it consists of two components in the Hα line, one in absorption and one in emission. The emission component traces the systemic velocity (Castor & Lamers 1979), the blue-ward part of the absorption component relates to the velocity of the moving envelope from the star.

1.2.3 Abundances

During the evolution of a massive star, the atmospheric abundances of He and CNO cycle products change, once that the nuclear reactions products have reached the stellar surface.

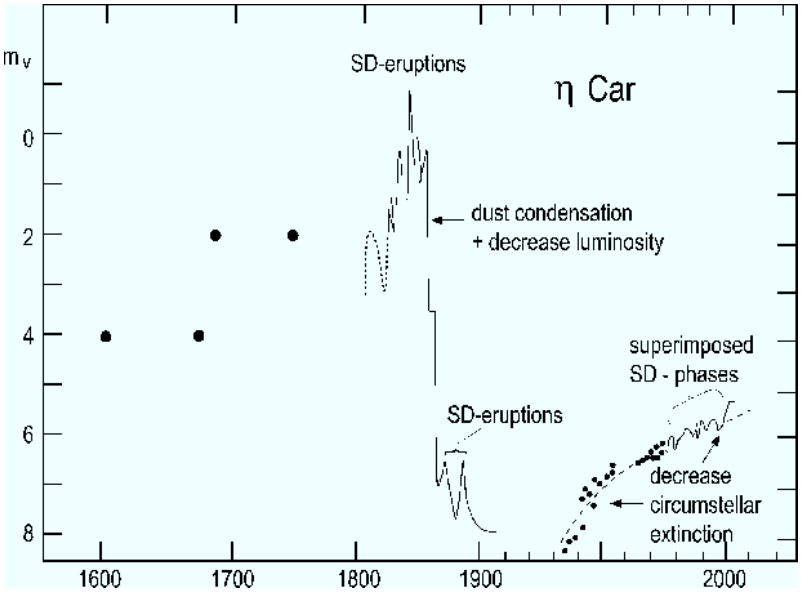

Figure 1.5: Visual light curve of η Car (van Genderen 2001).

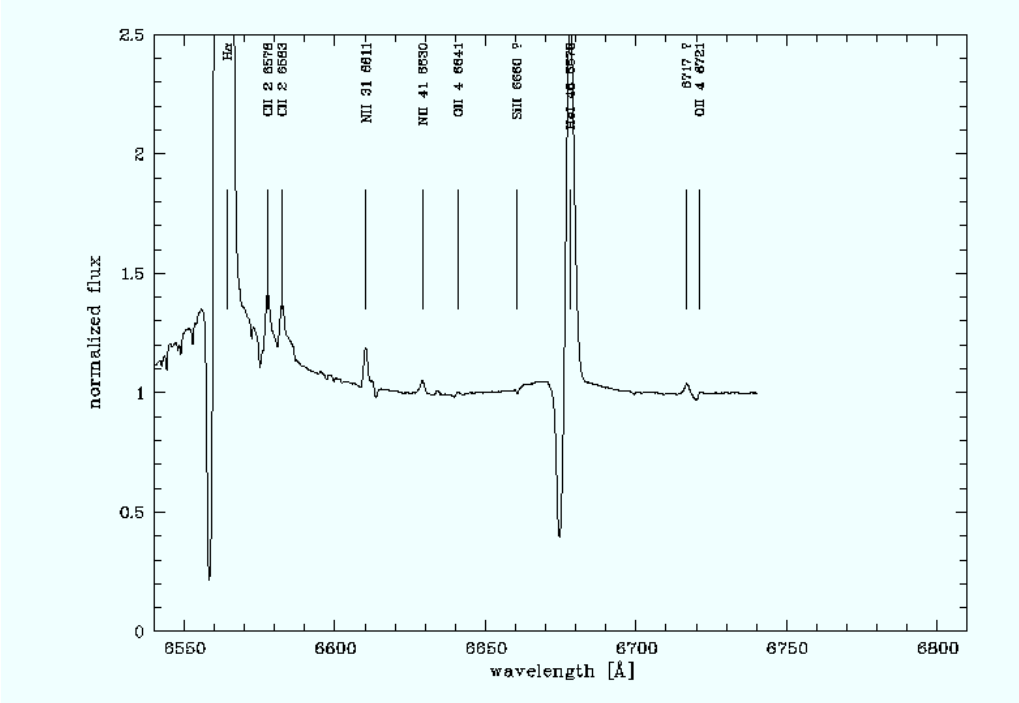

Figure 1.6: Spectrum of P Cyg in the wavelengths range 6550-6800 Å (`http://maps.seds.org/Star_sen/Spectra/pcyg.html`).

LBVs show a wide span of CNO ratios. Although most LBVs have He and N enhanced atmospheres, it seems unlikely that all of them have reached equilibrium CNO values in their outer atmospheres (Vink 2009).

Najarro, Hillier, & Stahl (1997) found a He atmospheric abundance n(He)/n(H) ranging between 0.25-0.55 in P Cyg, while for a typical LBV nebula Lamers et al. (2001) provide n(He)/n(H)$\sim$0.1-0.2.

1.2.4 Membership and recent census of LBVs

To officially qualify as LBV, an object should at least have shown the combination of spectroscopic/photometric variations, which are characteristic of S Dor-type variability due to changes in the apparent temperature of the star. Together with the variability, van Genderen (2001) included also other two criteria: the evidence of ejecta and high luminosity, coupled to high mass-loss rates (Sterken et al. 2008).

Depending on these criteria, catalogues in the literature contain two kind of objects: confirmed LBVs and candidate LBVs. Two main catalogues have been considered up to now: van Genderen (2001) and Clark, Larionov, & Arkharov (2005) counted 35 objects in the Milky Way (12 LBVs and 23 cLBVs) and 25 in the Magellanic Clouds (MCs).

Based on the discovery of many ring nebulae surrounding luminous stars, through observations with the space telescope *Spitzer*, Wachter et al. (2010) and Gvaramadze, Kniazev, & Fabrika (2010) have investigated the nature of such stars and proposed new objects as cLBVs in our Galaxy.

Considering the new entries, Nazé, Rauw, & Hutsemékers (2012) have updated the cLBVs catalogue, that now counts 67 objects in the Milky Way (see Table 1 in Nazé, Rauw, & Hutsemékers 2012). The confirmed galactic LBVs stay 12, as in Clark, Larionov, & Arkharov.

Summarizing, at the moment the known galactic cLBVs are 67, the magellanic cLBVs and LBVs are 25 and a few are known in other nearby galaxies (M31 and M33).

1.3 Proposed mass-loss mechanisms

To become a WR star (with $M < 20\,\mathrm{M}_\odot$), a massive ($22 < \frac{\mathrm{M_{ZAMS}}}{\mathrm{M}_\odot} < 150$) star has to shed its H envelope (Abbott & Conti 1987; Crowther, Lennon, & Walborn 2006). *Stellar winds* during the MS life of a star are not sufficient to strip off the H envelope and also moderate winds during the LBV phase could not be intense enough. For example, considering a mass-loss rate of $10^{-5} - 10^{-4}\,\mathrm{M}_\odot\,\mathrm{yr}^{-1}$ in a lifetime of a few times $10^4 - 10^5\,\mathrm{yr}$, a LBV star can lose between $0.1 - 10\,\mathrm{M}_\odot$, which is a substantial amount in the case of the lowest

massive stars to reach the WR phase, but not enough for the most massive stars. Hence, higher mass-loss rates are needed to reduce the star total mass and possibly through short-duration giant eruptions or explosions (Smith & Owocki 2006; Humphreys & Davidson 1994), like the outburst experienced by η Car in the 19th century, during which about $12 \sim 20\,M_{\odot}$ (Humphreys, Davidson, & Smith 1999; Smith et al. 2003) were ejected[2]. However, such events have been witnessed very rarely (e.g, η Car[3] and P-Cyg[4]). Hosted by nearby galaxies, other examples of eruptive events are known: for example, SN 1954J and SN 1961V, which were initially mistaken for SN events and later renamed as *SN impostors* (Humphreys, Davidson, & Smith 1999; van Dyk 2005).

Which mechanism drives the drastic events suffered by *giant* and *normal eruption LBVs* and the high or moderate mass-loss experienced by *S Dor-type variables* is not well-established. Moreover, whether and how the S Dor-type variables change the mass-loss via optically thin line-driven winds in optically thick winds (or in pseudo-photosphere) is also not clear (Vink 2009).

We give a brief summary of the main mass-loss mechanisms proposed until now in the literature.

Line-driven winds and the Bi-stability Jump Mass-loss in massive stars is generally due to optically thin line-driven winds, where the driving is caused by the radiation pressure on millions ionic spectral lines. The first description of the mechanism was proposed by Castor, Abbott, & Klein (1975) and then improved by Puls, Vink, & Najarro (2008), Lucy (2007), Vink (2000). Metal ions are efficient photon absorbers at specific line-frequencies, and where the resulting radiative acceleration dominates on the inward pointing gravitational acceleration, an outflow results (Vink 2008; Vink & de Koter 2002). In particular, the most efficient absorber in stellar winds is Fe, thanks to its highly complex atomic structure, with millions of line transitions[5], which make it an efficient absorber of radiation. However, line-driven winds are not sufficient to explain the mass ejecta (some $\sim M_{\odot}$) observed around different LBVs, in typical LBV timescales ($10^4 - 10^5$ yr).

Moreover, it has been noticed (e.g. the galactic LBV AG Carinae, hereafter AG Car) and then predicted that $\dot{M}$ changes drastically during the LBV excursion between the quiescent and the active phases (between the maximum and minimum apparent effective

[2]By proper-motion measurements it was found that the *Great Eruption*, observed visually in the 1840s, gave origin to the Homunculus nebula around η Car (Fig. 1.1).

[3]η Car must be considered an extreme example of LBV star, with the highest mass-loss rate derived, $\dot{M} \sim 10^{-3}\,M_{\odot}\,\mathrm{yr}^{-1}$ (van Boekel et al. 2003).

[4]It has been believed that the XVII century outburst, during which P-Cyg brightened several times, was characterized by an astonishing mass-loss rate, of the order of $\sim 10^{-2}\,M_{\odot}\,\mathrm{yr}^{-1}$.

[5]Thanks to these line transitions, Fe results a better absorber in respect to H, despite this in the Milky Way is 2500 times more abundant than the iron.

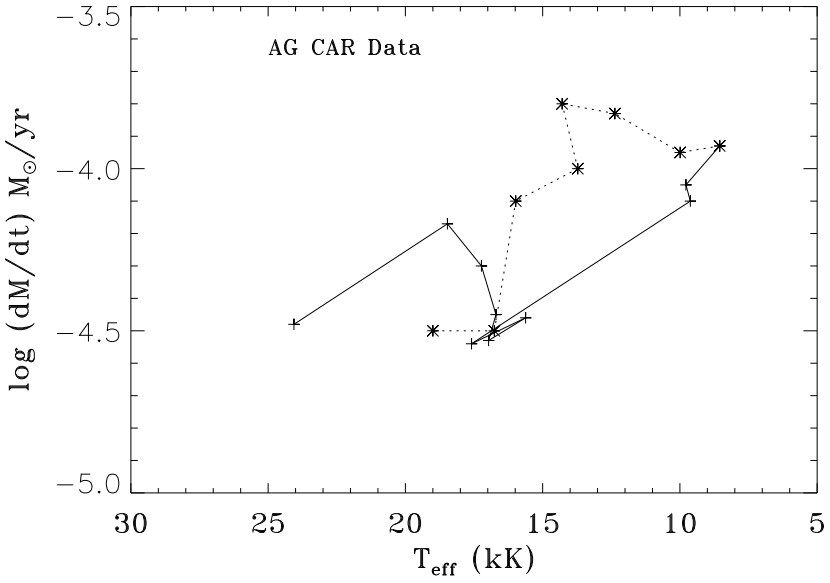

Figure 1.7: Empirical (dashed line) and predicted (dotted line) mass-loss rates for AG Car as a function of T_{eff}, as analysed by Stahl et al. (2001) and Vink & de Koter (2002) respectively. Figure taken from Vink & de Koter (2002).

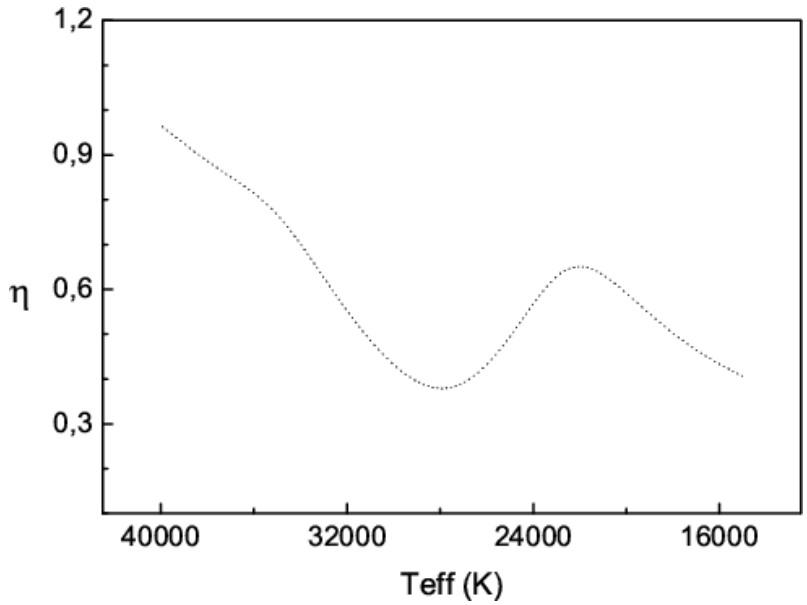

Figure 1.8: The predicted wind efficiency number $\eta = (\dot{M}v_\infty)/(L_*/c)$ as a function of effective temperature (from Vink, de Koter, & Lamers 2000). Note the presence of a local maximum at the position of the bi-stability jump around $T_{eff} = 21000\,\mathrm{K}$.

temperature, see Fig. 1.4 and 1.7). More specifically, $\dot{M}$ would increase strongly when stars evolve towards the B supergiant regime. This phenomenon is known as the *bi-stability mechanism*.

The cause of the *bi-stability jump*[6] in the mass-loss rate (in Fig. 1.4 the dashed vertical line and in Fig. 1.7 the jump in $\dot{M}$) is that the most important line-driving element, Fe, recombines from FeIV to FeIII at 21000 K and that suddenly the Fe lines become much more effective, as they fall in the wavelengths range where the flux distribution is maximal (Vink 2011) and more lines are available to drive the wind. The result is an increase in $\dot{M}$ and a drop in terminal velocity[7] (see Fig. 1.7 and 1.8). The latter has been confirmed in observed data (e.g. Lamers, Snow, & Lindholm 1995) but, as pointed out by Vink (2011), the jump in mass-loss rate is still controversial (e.g. Crowther, Lennon, & Walborn 2006; Benaglia et al. 2007).

The relevance is that LBVs brighter than $\log(L/L_{\odot})$=5.8 are expected to encounter the jump continuously, on timescales of their photometric variability, inducing variable mass-loss rates (Vink 2011).

The mass-loss rate modelled by Vink, de Koter, & Lamers (1999, 2000) can be written as a function of the stellar parameters

$$\dot{M} \propto L^{2.2} M^{-1.3} T_{eff} (v_{\infty}/v_{esc})^{-1.3} \tag{1.4}$$

where v_{∞} and v_{esc} are respectively the terminal flow and the effective escape velocities. This model is valid in the range T_{eff}=12500-5000 K, except for the bi-stability jump around 21000 K, where the predicted mass-loss properties change drastically, with a drop of v_{∞} and a jump of $\dot{M}$ by a factor of five (Vink, de Koter, & Lamers 1999; Vink 2011).

Metallicity independent mechanisms Recently, Smith & Owocki (2006) showed that high or even extreme mass-loss rates, needed to explain the observed nebulae, would cause heavy saturation for the line opacity and hence lines could not drive the wind. This means that if mass-loss during these eruptions occurs via a wind, it must be a super-Eddington wind driven by continuum radiation pressure (Thomson scattering opacity) from the stellar surface.

[6]The bi-stability jump was first discussed by Pauldrach & Puls (1990) in the context of their model calculations of the LBV P Cygni. The first empirical work on the bi-stability jump for a sample of stars was that by Lamers, Snow, & Lindholm (1995).

[7]The wind characteristics as a function of stellar spectral type are described also in terms of the wind efficiency number η (see Fig. 1.8):

$$\eta = \frac{\dot{M} v_{\infty}}{L/c} \tag{1.3}$$

a measure for how much momentum from the photons is transferred to the ions of the outflowing wind.

An alternative proposed by Smith & Owocki (2006) to the continuum-driven wind is a deep-seated hydrodynamic explosion. They explain that it may be due to inefficiency of the convection when the star is near the Eddington limit, generating a density inversion which leads to a violent explosion (Joss, Salpeter, & Ostriker 1973; Arnett, Meakin, & Young 2005; Young et al. 2005). In this case, unlike steady winds which are driven by lines, the driving in these eruptions may be independent of metallicity (Smith & Owocki 2006).

This must be yet established. However, very recently, a very interesting study of light echoes of the XIX century η Car Great Eruption seems to support the hydrodynamic explosion theory as mechanism responsible for the famous outburst (Rest et al. 2012).

What we know at the moment is that when a LBV is in the quiescent phase line-driven winds can justify the estimated mass-loss rate, but to explain the mass in the observed nebulae an extreme mass-loss mechanism must occur during the active phase. Which mechanism (an optically thick continuum-driven wind or a hydrodynamic explosion) cause the ejection of a huge amount of mass is not yet clear. Further, the duration and the frequency of these events in the lifetime of a massive star are also poorly understood. Concerning this, we know from the observations that both η Car and P Cyg, among the most studied LBVs, are surrounded by multiple shells, indicating that LBVs can suffer different extreme mass-loss episodes during their life (Walborn 1976; Meaburn 2001).

Among the most appealing explanations (e.g. Humphreys & Davidson 1994; Smith et al. 2011)for deep-seated hydrodynamic explosions there are:

> **Critical rotation limit**. A star may reach instability because of rapid rotation. However, it is not clear how reaching this critical rotation will induce a sudden outburst of mass-loss, and it does not explain the observed increase in the bolometric luminosity of giant eruptions.
>
> **Shell-burning explosions**. Explosive burning may be triggered by mixing of fresh H-rich fuel into deeper and hotter layers of the star. The mixing may be due to oscillations in the outer envelopes of the star.
>
> **Close-binary interaction events.** It has been suspected that some LBVs are in a binary system with a companion (e.g. η Car, HR Car). Increasing of the stellar radius during the post-MS evolution may cause collisions with the companion surface. It is possible that η Car XIX outburst was due to such kind of collision.

Implications If the only mechanism responsible for the mass-loss is the line-driven wind, then low-metallicity leads to less mass-loss in low-metallicity environments, per-

haps resulting in a preference of long Gamma-Ray Burst (GRB) in the early Universe (Vink 2011). In low-metallicity environments the efficiency of Fe drops drastically. Objects that are born with fewer Fe atoms may lose less matter by the time they reach the end of their lives, despite their longer contents of CNO material (Vink 2011). In this case host galaxy metallicity may play a crucial role for the evolution of massive stars.

Conversely, if the bulk of the mass ejected by the star is due to hydrodynamic explosions, rather than steady winds, as proposed by Smith & Owocki (2006), then the LBV phenomenon is independent of the metallicity and gives LBVs a great relevance in the evolution of the early Universe.

1.4 LBV Nebulae

The evolution of LBV stars is strongly influenced by the mass-loss during their post-MS life. As a result of intense and possible multiple mass-loss episodes (eruptions and/or stationary winds), LBVs are generally surrounded by circumstellar nebulae of gas (ionized, atomic, and maybe molecular) and dust (thermal, possibly PAHs...) that emit at different wavelengths. These nebulae represent, therefore, a fossil record of the most important mass-loss phase experienced by stars (Smith 2011). This is one of the reasons that make them interesting objects to study.

Based on the very limited number of LBVNe studied in detail, we present here some common aspects and possible similarities.

LBVNe are very massive. Fig. 1.13 shows nebular massed deduced by various authors (Fig. 1 in Smith & Owocki 2006). Not all LBVNe are massive as the one of η Car or Pistol star ($\sim$10-20 $M_\odot$). Some are only about $\sim$0.1 $M_\odot$[8]. Usually these nebulae are few solar masses.

These ejecta are typically 0.2-2 pc sized and ring-like or shell-like shaped (for example AG Car - Fig. 1.10 - and He3-519 - Fig. 1.12 - respectively), but many appear bipolar or hourglass-shaped (remember η Car - Fig. 1.1 and compare with Sher 25[9] - Fig. 1.11), and one is irregular (R143).

The dust and gas morphologies are sometimes very similar (co-spatial), but often very different (see for e.g. IRAS 18576+0341, Fig. 1.9). Some cases have shown the presence of different epoch shells (e.g. AG Car[10], Sher 25), implying the question: *how many*

[8]This is sometimes even seen in the same star: after ejecting $\sim$15 $M_\odot$ in its 1840s eruption, η Car subsequently ejected $\sim$0.1-0.2 $M_\odot$ in its smaller 1890 eruption (Smith 2005).

[9]cLBV Sher 25 has a circumstellar ring of gas that is considered the galactic twin of the ring surrounding the LMC SN 1987A. It also presents a bipolar outflows, as visible in Fig. 1.11.

[10]The AG Car nebula show two nested, concentric shells, which display differences in their expansion velocities (Nota et al. 1996a).

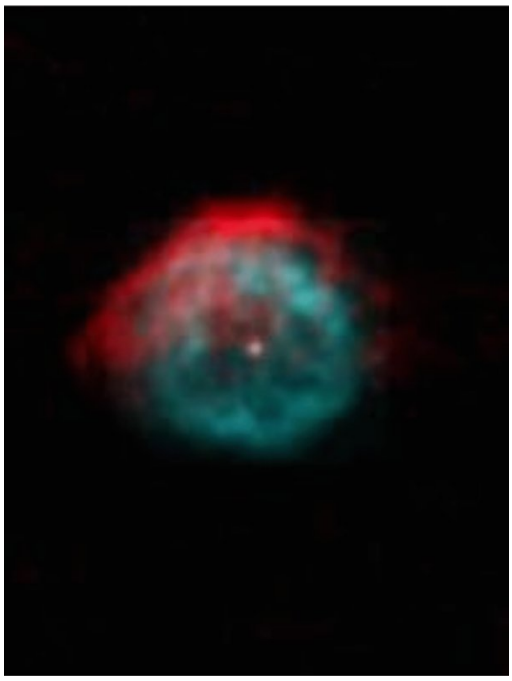

Figure 1.9: Composite image of IRAS 18576+0341 obtained by superposition of VLA radio images at 6 cm (red) and VISIR 17.65 μm (blue). Figure taken from Buemi et al. (2010).

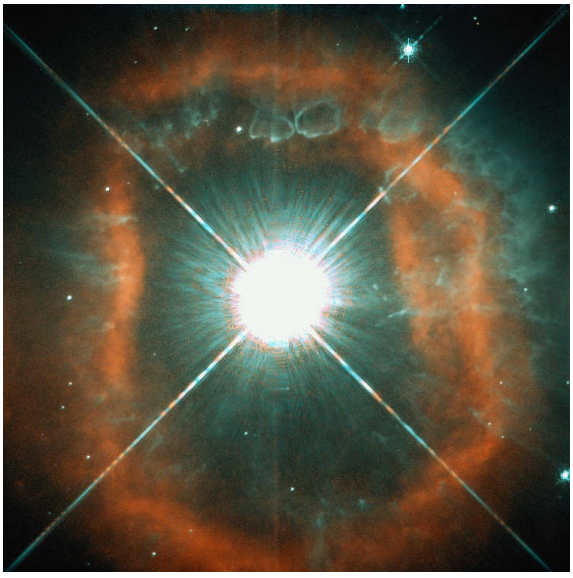

Figure 1.10: *HST* color image of the nebula around AG Car (Weis 2011).

Figure 1.11: Hα *HST* image of Sher 25.

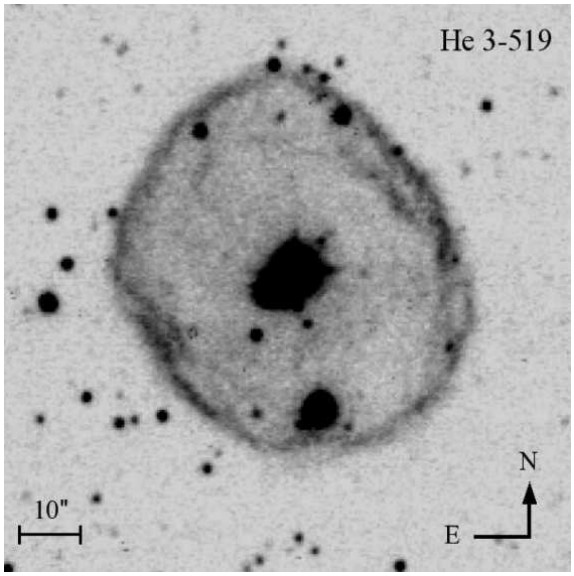

Figure 1.12: Hα *HST* image of He3-519. Figure taken from Weis (2011)

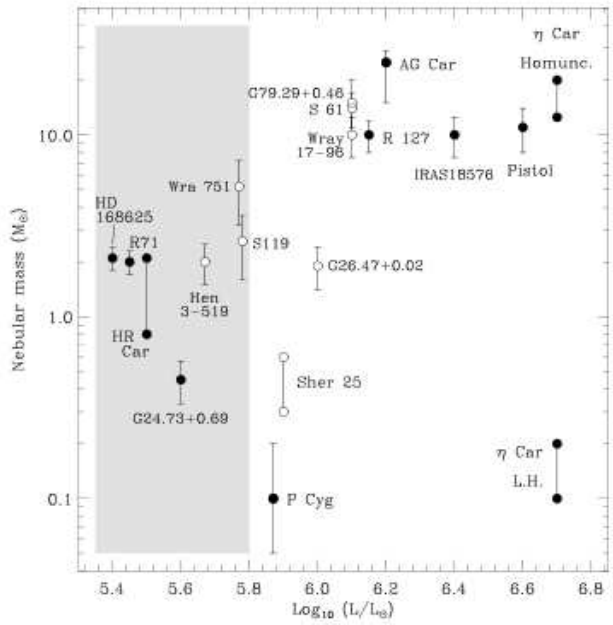

Figure 1.13: Deduced masses of LBV (filled circles) and cLBV nebulae (open circles) as a function of the central star bolometric luminosity. Luminosity are taken from Smith, Vink, & de Koter (2004), while references for the masses are given in Smith & Owocki (2006). The shaded part corresponds to luminosity of stars that may be post-RSGs. Figure taken from Smith (2008).

violent eruptions LBVs pass through? (Humphreys & Davidson 1994).

Quantitative analysis of the ejecta shows that they are N and He rich, indicating that nuclear material processed through the CNO cycle has risen to the surface and has been ejected (e.g. Davidson et al. 1986; Lamers et al. 2001; Smith 2011).

Among the open issues, there is the question whether Photo-Dissociation Region (PDR) are present in such ejecta. In fact, some LBV nebulae show complex molecules (e.g., PAHs), or other features typical of PDRs (e.g low-excitation fine structure lines), but if this is common to all the LBVs it is not yet established.

Several aspects of the LBV evolution can be investigated analysing the LBV ejecta, most of these aspects are linked to the mass-loss archaeology of the star. Among the most interesting aspects are the following:

- the total mass lost during the LBV stage. This can be recovered if one knows its duration and a time-averaged mass-loss rate (Humphreys & Davidson 1994). Or, better, one can evaluate the current mass-budget by observing the different emitting components;

- the geometry of the mass-loss, through a morphological study of the ejecta. For example, the bipolar nature of the Homunculus nebula (Fig. 1.1) shows that the Great Eruption must have been strongly aspherical.

- the epoch of the mass-loss episodes and the timespan between the most important events. The kinematical age can be directly determined knowing the nebula expansion velocity and radius.

- the origin of bipolarity. This may be attributed to mass-loss from a rapidly rotation star (e.g. Smith 2006), or to various degrees of asymmetry in the pre-existing environment (Frank, Balick, & Davidson 1995).

- the frequency of the outbursts.

1.4.1 The dust

Most well known galactic LBVNe contains dust. Formation of grains in LBVNe is yet unclear, as well as their capacity to survive despite the strong UV field from the star.

Infrared spatial observatories (*IRAS*, *ISO*, *MSX*, *Spitzer*) have shown very often an excess IR or, even, spatially resolved circumstellar material around these stars (e.g. Clark et al. 2003). In most cases, this emission is attributable to thermal graphite and silicates.

Spectroscopic studies revealed amorphous silicates in some LBVNe (for example, HR Car, Lamers et al. 1996; Umana et al. 2009).

In the case of HR Car, Umana et al. (2009) found that these silicates are distributed in the inner nebula and suggested that the dust formation during the LBV phase is possible. Crystalline dust features (e.g. AG Car, WRA 751, R71, Waters et al. 1998; Boyer et al. 2010) have also been observed, with similarity to dust found in Red Super Giant (RSG) stars, suggesting that the conditions in the dust forming layers (density, temperature, chemical composition) of these objects have been similar (Waters et al. 1998). Waters et al. hence proposed that AG Car and WRA 751 may have been RSG stars when they expelled the observed mass ejecta. However, this is still controversial (Lamers et al. 2001).

Complex molecules such as PAHs have been observed in some LBVNe (for example, in AG Car, Trams, Waters, & Voors 1997). PAH emission has been also indicated in R71 and in HD 168625 (Fig. 1.14, Umana et al. 2010).

AG Car and HD 168625 also show reflection nebulae, suggesting the presence of large grains. The nebula of HD168625 extends beyond the Hα ring; this is also the case in some parts of the AG Car nebula and of the HR Car nebula (Voors et al. 1997).

Dust temperature in LBVNe is generally between 50 and few hundreds K. Interesting is the correlation between the dust temperature and the optical nebular radius, as Hutsemekers (1997) noticed in its study of a sample of LBV stars (Fig. 1.16). This result is not strange, as the inner dust receives more heat from the star than the outer one.

What allows dust formation? Conditions for the dust formation depend on the environment where it forms, in particular the chemical composition of the gas phase and the

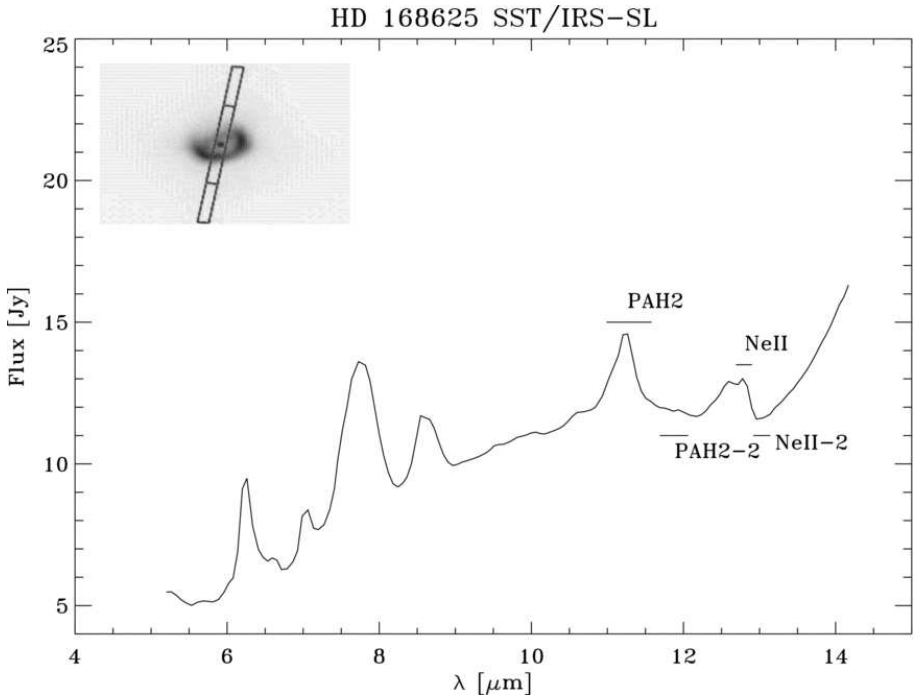

Figure 1.14: IRS-SL spectrum and in the upper left the fraction of the nebula sampled by the module. Figure as in Umana et al. (2010).

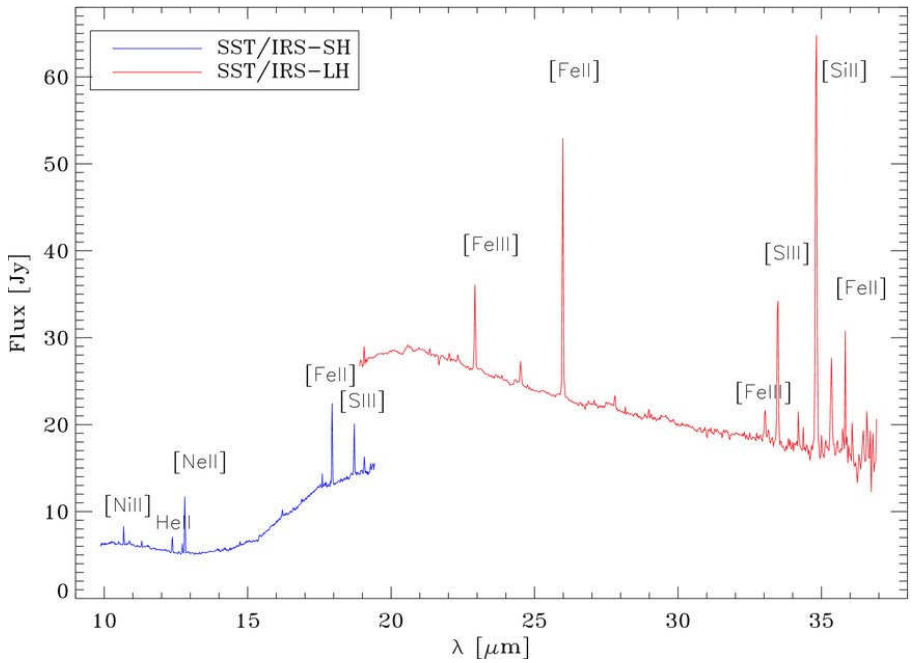

Figure 1.15: IRS high-resolution spectrum of HR Car (Umana et al. 2009).

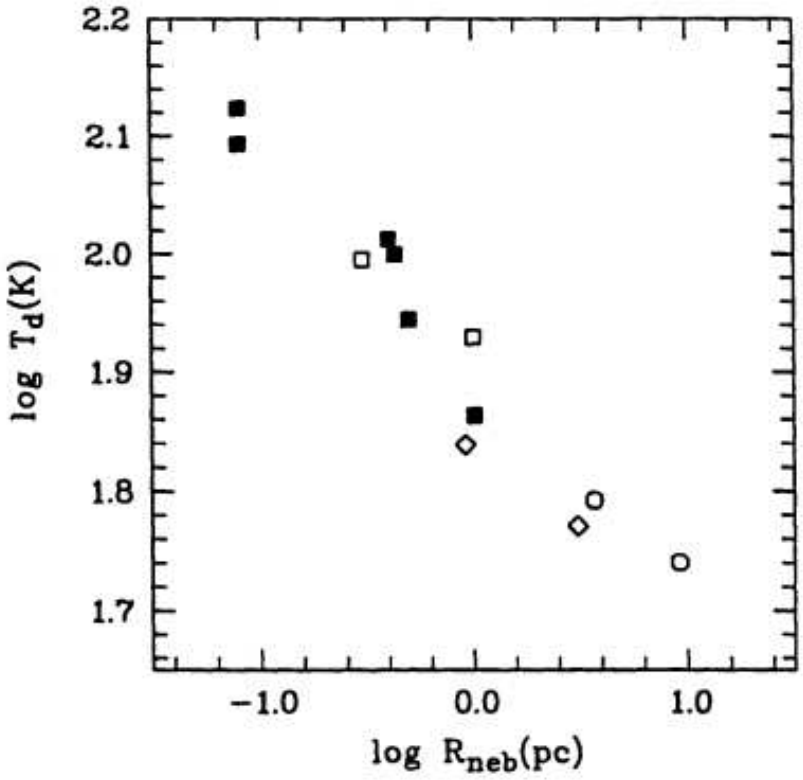

Figure 1.16: The nebular dust temperature as a function of the optical nebular radius of a sample of galactic LBVs (filled squares), LMC LBVs (open squares), WN8 and WN5-6 (losanges and circles).

internal energy of the grain just formed. In general, the ideal gas temperature must range from $\sim 700\,\mathrm{K}$ to $\sim 2000\,\mathrm{K}$, while the density between $\sim 10^{-13} - 10^{-15}\,\mathrm{g\,cm^{-3}}$ (Feder et al. 1966; Clayton 1979; Sedlmayr 1994; Gall, Hjorth, & Andersen 2011).

LBVs stars are late O, early B stars and have hence a strong ultraviolet radiation field that should prevent dust formation. Also the low-particle density environment should inhibit the dust growth. But it is evident that LBVs form considerable amount of dust, probably during the eruptive phase.

In fact, as discussed recently by Kochanek (2011), LBVs can expel enormous amount of material under conditions favourable to the growth of dust grains. For example, this is illustrated by the massive ($\sim 10\,\mathrm{M_\odot}$), optically thick dusty shell surrounding η Car. The phenomenon is more common than previously thought, since many 24 μm shells have been discovered with *Spitzer* around massive stars (e.g. Gvaramadze, Kniazev, & Fabrika 2010).

An explanation could be that high mass-loss rates favour particle growth and an optically thick environment (as the pseudo-photosphere) can shield the dust formation region.

1.4.2 The gas

In LBVNe the gas is almost ionized by the ultraviolet radiation from the star. The gas is hence observed mainly through continuum free-free emission in the centimetric and

millimetric range, or through the optical Hα recombination-line emission, if not extinguished[11] by dust or obscured by strong stellar radiation (as HR Car, Nota et al. 1997).

Radio emission from LBVNe has been already detected in AG Car, He3-519, WRA 751, HR Car (Duncan & White 2002), in IRAS 18576+0341 and HD168625 (Umana et al. 2005; Buemi et al. 2010; Umana et al. 2010), in Pistol Star (Lang et al. 2005).

Mid-IR and far-IR line emission from ionized elements are, for example, [NiII] 8.68 and 12.77 μm, [NeII] 12.81 μm, [CoII] 14.74 μ, [FeII] 17.93 μm, [SIII] 18.71 and 33.48 μm, [FeIII] 22.92 μm, [SiII] 34.81 μm, [OIII] 51.81 and 88.36 μm. Low-excitation fine structure lines ([FeII] and [SiII]) are indicative of the presence of a PDR, as pointed out by Umana et al. (2009) studying the mid-IR spectrum of HR Car (see Fig. 1.15).

Rotational lines of CO have been detected by Nota et al. (2002) in AG Car, but whether molecules are common features in LBVNe is an open question.

1.5 Motivations of this thesis

The number of known LBVs is still limited. The reasons are several. First of all, their are transition objects with a short lifetime ($\sim 10^4$ yr), as a consequence most of them evolved very rapidly. And a massive star itself is short-lived in comparison to the solar system timescale. Another reason is that these objects must experience spectroscopic and photometric variability to be members of the LBVs class. In the catalogues, most of the known objects are only candidate LBVs, probably because they were observed in the dormant phase (quiescence) and they did not experience outbursts during the observations. However, it has been proposed (van Genderen 2001) that a requirement to classify a star as LBV could be the presence of a nebula with properties that appear to be very common in the known LBVs.

One of the purpose of this thesis is to study, through a detailed multiwavelength analysis, the different emitting components in the ejecta of one among the most significant cLBV (G79.29+0.46) in our Galaxy. This analysis has the goal to better understand the physical and chemical properties of the nebula. Another goal is to recover the mass-loss history through analysis of the multiple-shells, indicative of different mass-loss episodes, and of the current-day mass-loss. Similar investigations may be then used as template to identify new objects through analysis of their ejecta and of the mass-loss phenomenon.

Until few years ago it has been believed that, being metal-free, the first stars would not have experienced mass-loss[12] before to explode as SNe. However, if the driving

[11] As the most LBVs in our Galaxy.

[12] Through the known line-driven mechanism.

mechanism for the outburst which LBVs seem to suffer is not sensitive to metallicity, as suggested by Smith & Owocki (2006), then the first massive star evolution must be revisited. As pointed out by the authors of the mentioned work, since we do not know yet what triggers LBV eruptions, we can not claim that these eruptions occurred in the first stars.

A way to understand the phenomenon, from an observational point of view, is to study the LBVs in environments with a metallicity different from the solar one. The intriguing aspect of this study is the cosmological implication that would have. In fact, if the LBVs outbursts occurred also in the early Universe, when massive stars would have been more numerous, with a flatter initial mass function than stars at the present epoch (Bromm & Larson 2004), then they could have had a paramount importance providing the necessary processed material and mechanical energy to the interstellar medium for future generations of stars.

Studying LBV nebulae in an environment different from those galactic is one of the purpose of this work. Here we provide a pilot study at the radio wavelengths of LBV ejecta in the LMC, which is the closest galaxy to the Milky Way and has half the solar metallicity. The goals of this pilot study are: to detect for first time LBVNe in the LMC at centimetric wavelengths; to study the nature of the radio emission; to recover the ejecta mass and size and the mass-loss history, through analysis of the current-day mass-loss rate and of possible multiple shells in the selected targets; to compare these properties with galactic examples.

LBVs have also been considered as possible *dust producers* in high-redshift galaxies (Gall, Hjorth, & Andersen 2011), where the significant amount of dust observed in the sub-mm is yet unexplained. To explore this possibility, we should understand how much dust LBVs produce. Most of the galactic objects has already shown the presence of dusty nebulae. Instead, observations in the IR have not been performed so far in LMC objects (except few cases), in part because of unsuitability of the current instruments.

Therefore, another goal of this work is to explore the dust content in the LMC's LBVNe, by comparing high-resolution radio maps obtained during this PhD program with H_α *HST* images. This analysis may be then used as starting point to plan high-resolution observations with the upcoming Atacama Large Millimeter/submillimeter Array (ALMA).

Part I

A galactic template: the candidate LBV G79.29+0.46

Figure 1.17: Three-colour image of the galactic cLBV G79.29+0.46 in the *Spitzer*/IRAC bands. Red: 8 μm; Green: 5.4 μm; Blue 3.6 μm. Maps provided by the *Cygnus-X Legacy Survey* (`http://www.ipac.caltech.edu/spitzer2008/proceedings.html`).

G79.29+0.46 is a candidate LBV located in the Cygnus-X ($D \sim 1.7$ kpc, Schneider et al. 2006), one of the richest star forming regions in our Galaxy. Thanks to its location and also to its beautiful aspect and intriguing nature, this star and its associated nebula have been widely observed in the spectral domains, ranging between the optical and the radio, with plenty of instruments. This makes this source a perfect object to study applying a multiwavelength approach. The advantage of the former is that it permits the study of different aspects and different emitting components related to the LBV phenomenon, useful to constrain fundamental parameters in the context of the massive star evolution.

This work started with the observations on G79.29+0.46 performed at EVLA (P.I. Umana G.), which we present in Chapter 3 together with the infrared images taken by the satellite *Spitzer*. This investigation was followed hence by further radio observations at GBT (P.I. Trigilio C.) and by the analysis of almost all the data available in the archives, as illustrated in Chapter 4.

Park of this work has been performed thanks to a collaboration between INAF/OACT

and NASA/IPAC and was supported by a grant from JPL/Caltech that allowed the author of this thesis to spent four months in Pasadena, CA.

Chapter 2

EVLA and GBT observations of the nebula around G79.29+0.46

Abstract

We have observed the nebula around the candidate LBV G79.29+0.46 with the EVLA at 20 and 6 cm, using the array in the configurations D and C. The maps of the radio nebula have an angular resolution of $\sim$ 3.1" at 6 cm and of $\sim$ 25" at 20 cm and sensitivities ranging between 0.07-2.6 mJy beam^{-1}.

We have also performed GBT observations of the radio nebula, in order to complement the interferometric datasets with the most extended emission. At GBT we used the same bands (L and C) as at EVLA and got a sensitivity of 20 Jy beam^{-1} in band L and of 5 Jy beam^{-1} in band C, with the beams respectively 8.4' and 2.4'.

Analysis of the radio maps provides us with: the spectral type, the current-day mass-loss and the spectral index of the central object; the spectral index map and the ionized mass of the nebula around G79.29+0.46.

The radio maps are then compared with the *Spitzer* IRAC (8 μm) and MIPS (24 μm and 70 μm) images, which we retrieved from the data archive and reprocessed. We confirm the presence of a second shell at 24 μm and provide evidence of its detection at 70 μm.

The comparison between the radio emission, which traces the ionized gas, and the IR emission, which traces the dust, shows that different emitting components are distributed in different shells. Moreover, there are at least two populations of dust: the warmer one, at shorter distances from the star, emitting in the IRAC bands, and the colder dust, which is distributed in two shells at bigger radii and emits in the MIPS bands.

We also estimate the kinematical age of the nebula and the timespan between the two great eruptions occurred in the past. All the parameters found in this work are consistent

with previous estimates and with values of other galactic LBVs.

Finally, we discuss finer details of the ionized gas distribution, which can be appreciated thanks to the improved quality of the new 6 cm image, for example brighter features associated with the interaction between the nebula and the surrounding interstellar medium. In particular, the brighter filaments in the south-west region appear to frame the shocked south-western clump reported from CO observations. These filaments show to be related to the shock also in our spectral index map.

Part of this work has been published in a special edition of the Astrophysical Journal Letters (Umana et al. 2011b).

2.1 Introduction

G79.29+0.46 is a galactic candidate LBV placed in the Cygnus-X star forming region. It has been discovered in the radio by Wendker, Higgs, & Landecker (1991), which found a highly symmetric ring-like nebula surrounding the star, after DRAO Synthesis Telescope observations. Later Higgs, Wendker, & Landecker (1994) performed high-resolution interferometric VLA observations and attributed to the continuum radio emission a thermal nature. They suggested that the ring-like nebula is an ionized shell of swept-up interstellar material. The real nature of the nebula was determined by Waters et al. (1996) which, by examining infrared IRAS images, pointed out that the ring-like structure is a detached shell formed during an epoch of high mass-loss ($\sim 5 \times 10^{-4} \mathrm{M}_{\odot}\mathrm{yr}^{-1}$) and followed by a more quiet period.

G79.29+0.46 was hence proposed to be a LBV, but it is still a candidate because its observed properties to date do not satisfy the spectral and photometric variability needed to be accepted as LBV (see Sections 1.2.2 and 1.2.4 for further details). However, recently Vink et al. (2008) found Hα variations, suggestive of mass-loss variability during S-Dor variations.

More recently, the space telescope *Spitzer* provided high-sensitivity, high-resolution InfraRed Array Camera (IRAC) (Fig. 1.17) and Multiband Imaging Photometer for *Spitzer* (MIPS) maps (The Cygnus-X *Spitzer* legacy program, Hora et al. 2010) which provided a better understanding of the dust properties (Kraemer et al. 2010).

Based on observations made with the Submillimeter Telescope (SMT), Rizzo, Jiménez-Esteban, & Ortiz (2008) investigated the molecular gas surrounding the nebula. They detected CO millimeter emission in large-scale features, which are probably background and/or foreground emission associated with the star forming region DR15, but also in minor-scale high density features, coincident with more than half the IRAS nebula. They

also reported the presence of a shock front, interpreted as a natural consequence of different wind regimes during the central object's evolution. The observed clumps may have been formed during a mass-eruption occurred about $10^3 - 10^4$ yr ago.

Our knowledge of the radio emission has been limited to the 1988 VLA data reported by Higgs, Wendker, & Landecker (1994) and to the 1400 and 350 MHz Westerbork observations, carried out between 1996 and 1997 and reported by Setia Gunawan et al. (2003). These observations were limited in resolution and especially in sensitivity.

For this reason we performed new Expanded Very Large Array (EVLA) observations with sufficient dynamical range, sensitivity, and angular resolution to provide a good match to the *Spitzer* images. The EVLA observations allow, for the first time, a detailed morphological comparison with other maps tracing the different components of the nebula.

However, a problem typical of interferometers is related to the short spacing in the *uv*-plane. In fact, an array does not provide the "zero baseline". When a source is very extended, it has much more power at the short spacing. If these spacing are unsampled the result is that it is impossible to interpolate the total flux, i.e. the extended emission. In principle the appropriate value would be that measured by a single element of the array, but in practice, single array elements rarely have sufficient sensitivity to provide this estimate accurately (Cornwell, Braun, & Briggs 1999). To overcome this problem, we carried out observations with a single, big and sensitive radiotelescope, the Green Bank Telescope.

In order to study the nature of the central object, previously detected by Higgs, Wendker, & Landecker (1994), we have also retrieved and analysed VLA archive data at 8.46 GHz.

In Section 2.2 we describe our radio observations and data reduction processing, together with the *Spitzer* images, which we reprocessed for a comparison of the IR emission with that radio. We show the obtained radio maps in Section 2.3, followed by the analysis of the ionized gas emission (Section 2.4). In Section 2.5 we compare the gas distribution versus the dust components present in the nebula. Finally, we present our final remarks in Section 2.6.

2.2 Observations and Data Reduction

In this section we describe our EVLA and GBT observations, together with the data reduction process made in this work. Tables 2.1 and 2.2 summarize the observational strategy adopted. A subsection is dedicated to the archival VLA data at 8.46 GHz and to the

Table 2.1: EVLA observational summary.

Observing dates	Configuration	Frequency (GHz)	Integration time on-source (min)	Phase Cal
2010 June 1	D	1.391	75	J2052+3635
2010 June 11	D	4.959	75	J2015+3710
2010 December 1	C	1.391	75	J2015+3710
2010 December 5	C	4.959	75	J2015+3710

Table 2.2: GBT observational summary.

Observing dates	Frequency (GHz)	Integration time (s)
2011 June 4-6	1.475	97.2
2011 June 4-6	5.100	97.2

Spitzer images that we reprocessed for a comparison with our radio maps.

2.2.1 EVLA observations

Observations of the radio nebula surrounding G79.29+0.46 were made at 1.4 and 5 GHz with the EVLA in two configurations (D and C, respectively on 2010 June 1 and 11 and 2010 December 1 and 5) and a total bandpass of 256 MHz (P.I. Umana G.). The observations consisted in 5-min scans on the target (centred at RA 20:31:42.0, Dec +40:21:59.0, J2000), preceded and followed by 1-min scans on the phase calibrator, for a total of 75 minutes on-source integration time. J0137+3309 was pointed to obtain both the bandpass and flux calibrations.

Dadasets were edited and reduced by using the **C**ommon **A**stronomical **S**oftware **A**pplications (CASA) package, version 3.0.2. Bad baselines and channels were removed when noisy or not properly working. After applying the bandpass and time-based gain corrections, the datasets were imaged adopting a natural weighting scheme to the visibilities and using the *Clark* algorithm for the dirty image deconvolution. The cleaned images were therefore convolved with a 2D-Gaussian, with the Half Power Beam Width (HPBW) reported in Table 2.3. Following this scheme, we have obtained four maps,

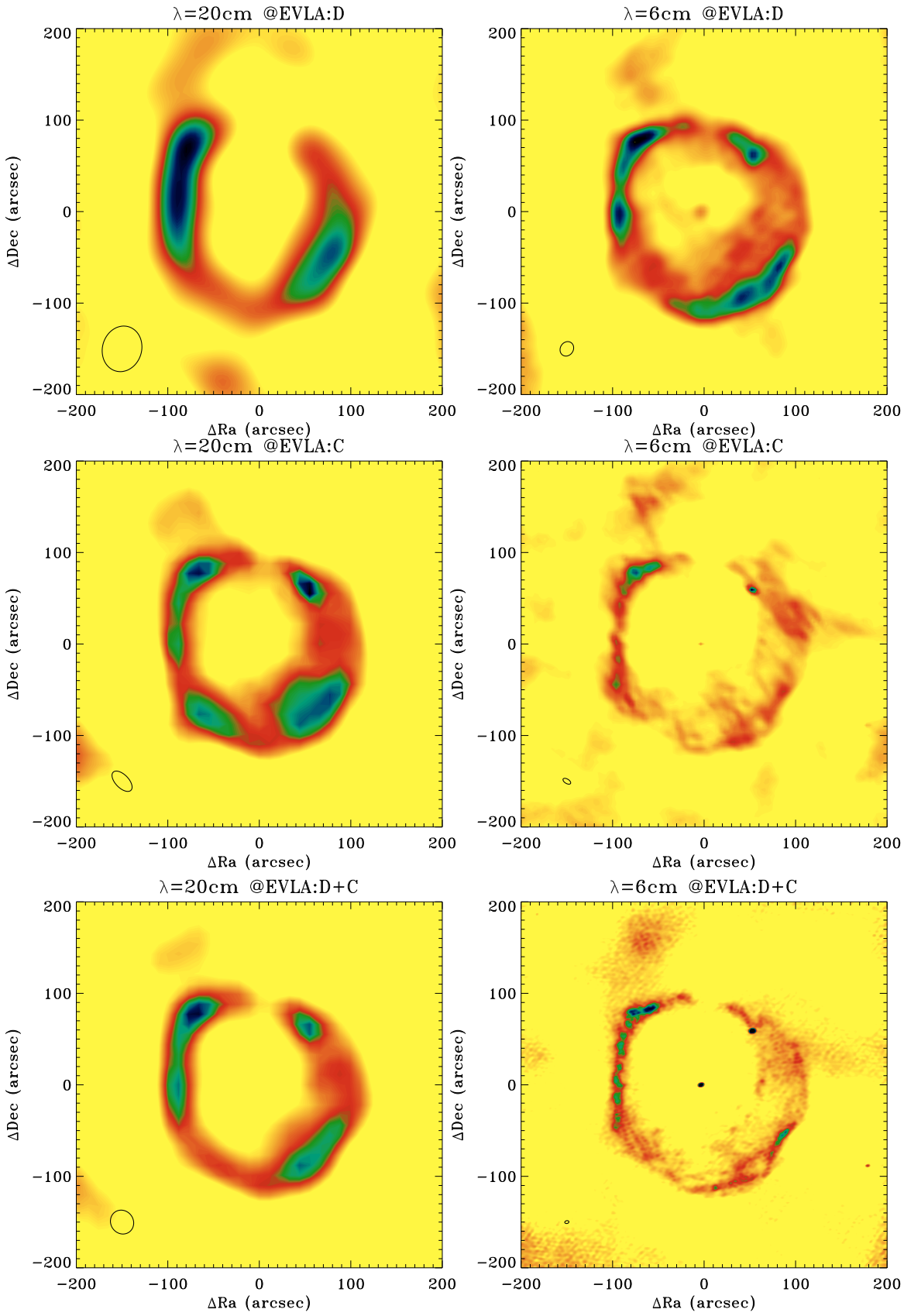

Figure 2.1: EVLA radio maps obtained in this work. On the left: 20 cm maps at three different resolutions. On the right: 6 cm maps. In the bottom-left corner of each panel the synthetic beam is shown, i.e. the resolution in the map. The map in the bottom-right corner has already been published in Umana et al. (2011b).

Table 2.3: Properties of the radio maps.

Configuration & frequency	HPBW (arcsec)^2	PA (deg)	LAS (arcsec)	Peak on-source (mJy beam^{-1})	rms (mJy beam^{-1})
EVLA:D, 1.4 GHz	50.40×42.83	163.6	129	26.0	2
EVLA:D, 5 GHz	16.46×14.16	-33.2	88	6.8	0.7
EVLA:C, 1.4 GHz	27.72×14.44	44.4	258	9.6	2.5
EVLA:C, 5 GHz	9.41×4.84	58.7	124	2.11	0.18
EVLA:D+C, 1.4 GHz	26.84×24.65	36.1	129	13.17	2.6
EVLA:D+C, 5 GHz	4.56×3.09	101.16	124	1.76	0.07
GBT, 1.4 GHz	504×504	0	4500	19.83×10^3	10.9×10^3
GBT, 5 GHz	144×144	0	1500	14.27×10^3	10.66×10^3
GBT&EVLA:D+C, 1.4 GHz	26.84×24.65	36.1	4500	17.5	4.3
GBT& EVLA:D+C, 5 GHz	4.56×3.09	101.16	1500	3.07	0.63

which we present in the top and middle panels of Fig. 2.1. In the table we also report the peak flux density (on-source) and the rms evaluated on the map.

The corrected visibilities at 1.4 and 5 GHz in both the two configurations were then combined, in order to increase the *uv*-coverage[1]. This consists in the concatenation of data with different spatial frequency in the visibility plane. Once we got a single dataset per frequency, we performed a new imaging process, with the *Clark* algorithm. This time we chose a Briggs-type weighting scheme for visibilities for the map at 6 cm, by setting the robust parameter equal to 0, a compromise between uniform weighting of the baseline for highest-resolution and natural weighting for highest-sensitivity. To achieve high-resolution images that are also sensitive to extended structure (Brogan et al. 2006), we used the multi-scale CLEAN method. At 5 GHz the resulting image rms-noise is 0.07 mJy beam^{-1} and the synthetic beam 4.56"$\times$3.09". At 1.4 GHz the rms-noise is 2.6 mJy beam^{-1} and the synthetic beam is 26.84"$\times$24.65". Peak on-source is listed in Table 2.3 for all the maps.

The final images are shown in the last two panels of Fig. 2.1 and are described in Table 2.3. The best image obtained is the 6 cm map, which offers the highest-resolution and the best sensitivity.

2.2.2 GBT observations and data processing

As shown in the figures, the radio nebula is about $2' \times 2'$ sized. The Largest Angular Scale (LAS) of EVLA (see column 2 in Table 2.3) filters out the extended emission. Hence we expect that diffuse emission from the nebula is not detected.

In order to complement the EVLA dataset, single-dish observations were performed at the Green Bank Telescope (GBT) at 1.4 and 5 GHz and G79.29+046 was observed as target within the project "Unveiling the nature of Galactic Bubbles" (P.I. Trigilio, C.). The sensitivity achieved is 20 mJy beam^{-1} at 1.4 GHz and 5 mJy beam^{-1} at 5 GHz, where the beam is respectively $(8.4')^2$ and $(2.4')^2$. The field of fiew of the maps, which were obtained running 30 scans on both RA and DEC directions, is $1^\circ 15'$ at 1.4 GHz and $25'$ at 5 GHz. Calibration and imaging processing of the GBT data are not the goal of this work and are described in the PhD thesis of Adriano Ingallinera. The maps are shown in Fig. 2.2 and 2.3. White circles in the figure centre represent position and size of the radio nebula as observed with the EVLA. Black circles in the left bottom corner represent instead the GBT beam.

The GBT maps were reprocessed in this work in order to be comparable to the EVLA maps, as in the following discussion.

[1] I.e. the sampling in the visibility plane (focal plane) of the interferometer.

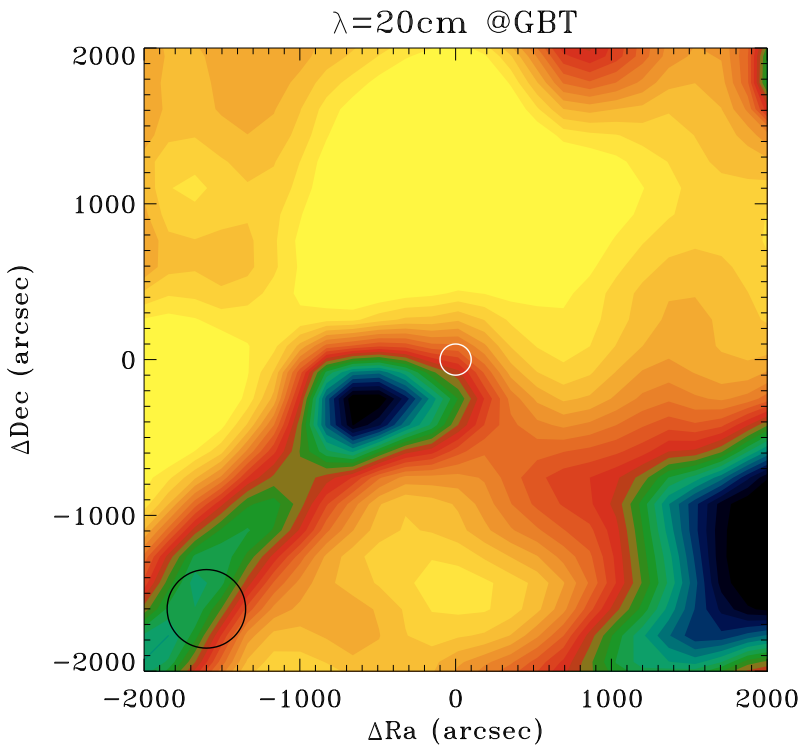

Figure 2.2: GBT image at 1.4 GHz. The white circle represents size and position of the radio nebula observed with EVLA, while the black one the GBT beam.

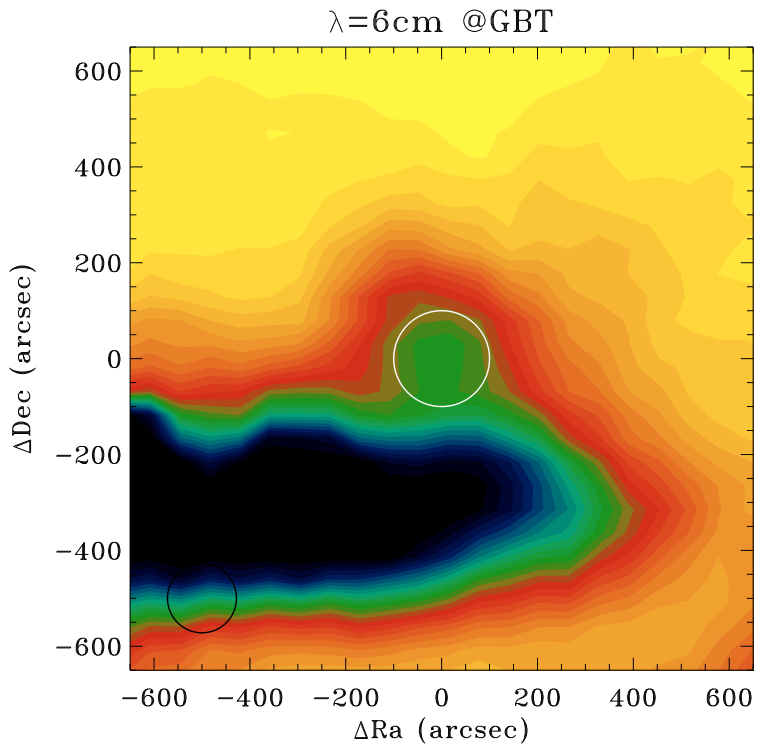

Figure 2.3: GBT image at 5 GHz. The white circle represents size and position of the radio nebula observed with EVLA, while the black one the GBT beam.

The process of combining single-dish and interferometric data has the advantage to recover the zero baseline (i.e. the largest angular scale visible by a single telescope), but also to maintain the high-resolution provided by the maximum baseline of the interferometer (corresponding to the smallest angular scales resolved and the fine details in the nebula).

Before combining the two datasets, we processed them at the same units. In fact, the GBT map is in unit of the antenna temperature T_A. Therefore, first we converted in Jy beam^{-1} according to the formula

$$S = \frac{T_A}{G}\,[\mathrm{Jy\,beam^{-1}}] \tag{2.1}$$

where the GBT antenna gain is $G = 2.84\eta_A$, with the antenna efficiency $\eta_A = 0.72$, valid at both the frequencies 1.4 GHz and 5 GHz (see observing manual for the GBT at `www.gb.nrao.edu/gbtprops/man/GBTpg.pdf`).

The maps were then rescaled to the same central frequency of the EVLA data (being in origin the GBT central frequencies 1.475 and 5.100 GHz and the EVLA ones 1.391 and 4.959 GHz). This conversion was performed assuming that the emission is almost due to optically thin free-free ($\alpha \sim -0.1$), valid assumption in LBVNe. The resulting peak flux density and rms-noise in the maps are: 19.83 Jy beam^{-1} and 10.09 Jy beam^{-1} at 1.4 GHz; 14.27 Jy beam^{-1} and 10.66 Jy beam^{-1}. The dynamical range in both the maps is limited by the background diffuse emission in the whole area covered by the GBT observations.

The new single-dish maps were then imported into the CASA 3.4 format and processed together with the EVLA maps at 1.4 and 5 GHz (left and right respectively of bottom panels in Fig. 2.1), using the task `feather`, which is an algorithm for combining two images with different spatial resolution. It consists in: regrid the low-resolution image to the same grid of the high-resolution image; Fourier transform each image to the gridded visibility plane; sum the gridded visibilities; transform back to the image plane (`http://casaguides.nrao.edu/`).

The final maps at both the frequencies 1.4 and 5 GHz are shown in Fig. 2.4 and 2.5. As we are interested only in the nebula of G79.29+0.46 we plot a zoom of the maps. In the bottom left corner the black circle represents the size and shape of the interferometric beam. At 1.4 GHz the peak flux density on the nebula is 17.5 mJy beam^{-1} and the rms-noise is 4.3 mJy beam^{-1}, where we remember that the beam is 26.84"$\times$24.65". At 5 GHz instead the peak is 3.07 mJy beam^{-1} and corresponds to the background point-source projected on the nebula in the north-west direction. In this case the rms-noise is about 0.63 mJy beam^{-1}, where the resolution is the synthetic beam obtained with EVLA:D&C configurations.

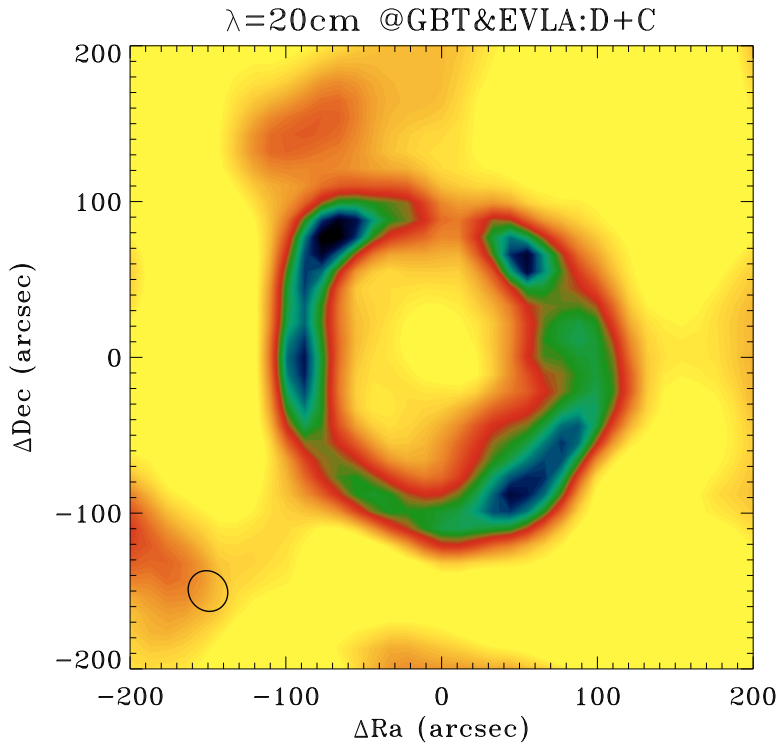

Figure 2.4: Final image at 1.4 GHz, after combining GBT and EVLA images. In the bottom-left corner the synthetic beam (provided by the EVLA maximum baseline) is shown.

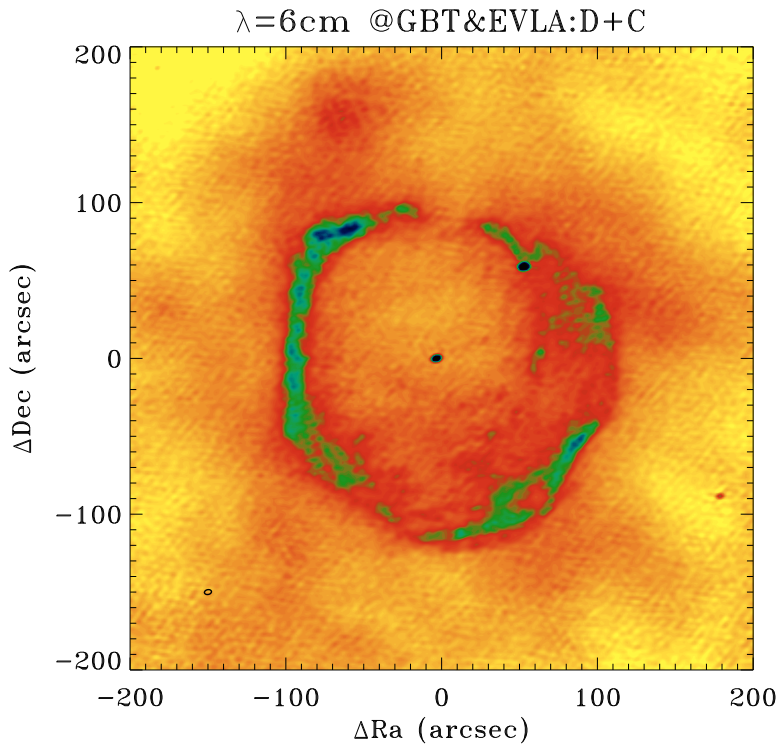

Figure 2.5: Final image at 5 GHz, as before.

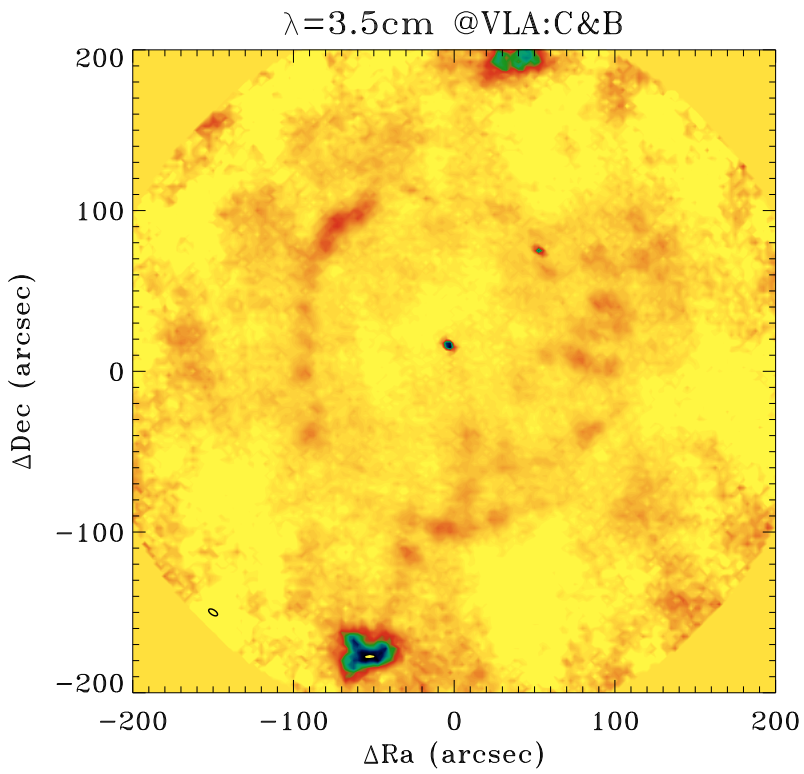

Figure 2.6: VLA map at 8.46 GHz. The black circle in the bottom-left corner is the synthetic beam.

These new values can be compared to the measurements listed in Table 2.3. After the combination with the single-dish data, the result is that the flux density has slightly increased (few mJy beam^{-1}), as well as the rms-noise. The former may be overestimated because of the diffuse emission region.

2.2.3 Archival VLA data

Exploring the VLA data archives, we have found further data at 8.46 GHz. The observations were performed in May and August 2005, using the configurations C and B (P.I. Lang C.) and a bandwidth of 50 MHz. We have retrieved these datasets and calibrated them adopting the same procedure used for the EVLA data. Hence we have combined both the configurations in order to get the best *uv*-coverage and we obtained a cleaned map, using the natural weighting, the *Clark* algorithm and the multiscale CLEAN method. The resolution of the map is 6.25"×3.12" at position angle (PA) of 57.3 deg. The peak flux density on-source is 1.68 mJy beam^{-1}, and the average rms-noise 0.15 mJy beam^{-1}. The resulting map is in Fig. 2.6.

2.2.4 *Spitzer* data

As already discussed in Umana et al. (2011b), to compare the gas morphology in the G79.29+0.46 LBVN with the dust distribution, we have retrieved and then reprocessed archival data obtained with the instruments IRAC and MIPS on board of *Spitzer*. These images are shown in Fig. 2.11. In the following subsections we report the same description as in the paper.

IRAC data

Infrared imaging of the field including G79.29+0.46 was performed at 3.6, 4.5, 5.8, and 8.0 μm with the instrument IRAC (Fazio et al. 2004) on the *Spitzer* (Werner et al. 2004). All available data for G79.29+0.46 from the cryogenic *Spitzer* mission archive were used, including AORIDs 6050560, 17330688, 27106560, and 27107584. The observations used the 12 and 30 second HDR modes, which obtain integrations with frame times of 0.6 & 12 seconds and 1.2 & 30 seconds, respectively. The Basic Calibrated Data (BCD) were retrieved from the archive (pipeline version S18.18), and additional interactive processing was performed using the `imclean`[2] tools to remove image artefacts from bright sources, including muxbleed, banding, and column pulldown effects (Hora et al. 2004). Mosaics at each wavelength were constructed using IRACproc (Schuster, Marengo, & Patten 2006), combining the data which was taken at different spacecraft orientations and resampling to a final image pixel size of 0.6". Outliers due to cosmic rays or instrument artefacts not previously flagged are removed in this process. The images were combined using a weighting based on the integration time of the frames. In pixels that are saturated in the longer exposures, only the shorter frames are used in the final image.

MIPS data

The MIPS data was taken as part of the Cygnus-X *Spitzer* Legacy program (PID 40184, P.I. J. Hora) in the fast scanning mode with a cross scan step of 148" to fill the 70 μm array, resulting in an integration time of 15.7 seconds per pixel on a single scan leg at both 24 and 70 μm. The 24 μm data were reprocessed using the MIPSGAL (Carey et al. 2009) data processing pipeline (Mizuno et al. 2008). The 70 μm data also used the MIPSGAL pipeline (Paladini et al. 2011) with the exception that the non-linearity correction at 70 μm was performed per pixel using the prescription defined by the SINGS Legacy team (Dale et al. 2007), based on the behaviour of the MIPS 70 μm calibrators.

[2]http://irsa.ipac.caltech.edu/data/SPITZER/docs/dataanalysistools/tools/contributed/irac/imclean/

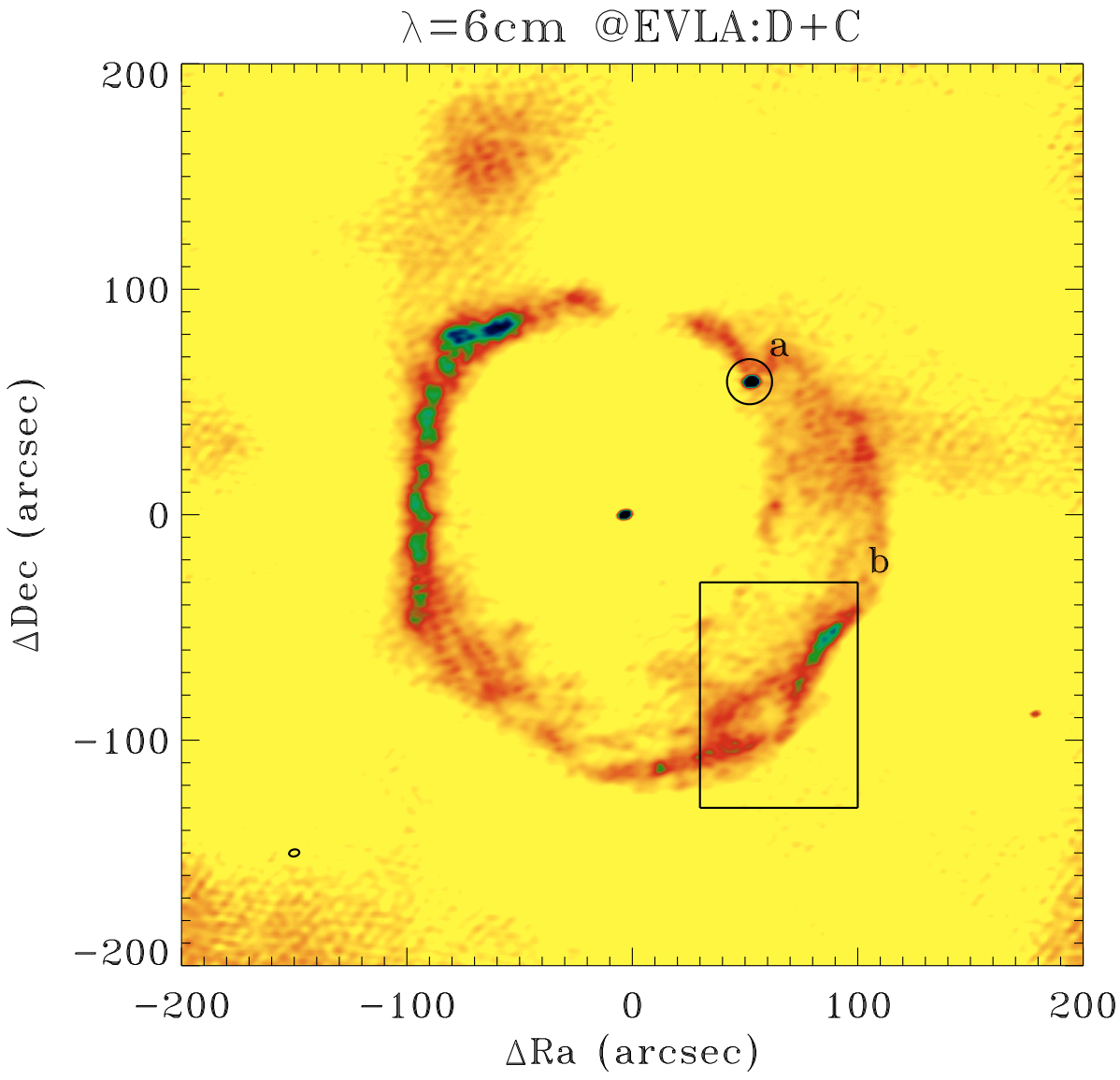

Figure 2.7: 6 cm EVLA map of G79.29+0.46 obtained by combining the data from two different array configurations, C and D. The field of view is $2.5' \times 2.5'$ centred on the LBV position.

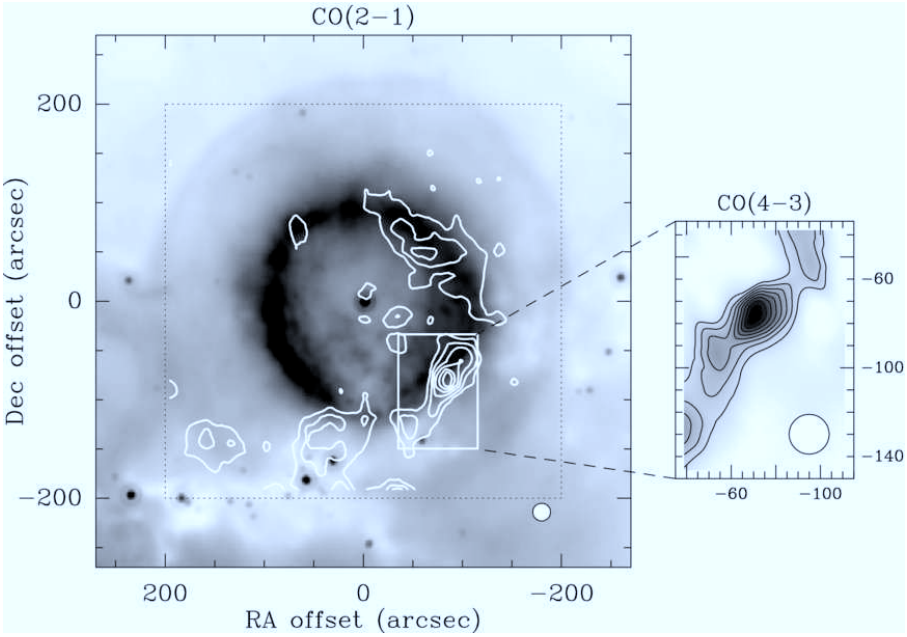

Figure 2.8: Left: CO J = 2 → 1 map around G79.29+0.46, as obtained with the IRAM 30 m radio telescope. Right: CO J = 4 → 3 map, corresponding exactly to the inset in the left panel, as obtained with the SMT 10 m radio telescope. Figure taken from Jiménez-Esteban, Rizzo, & Palau (2010).

2.3 The radio maps

2.3.1 EVLA maps

The obtained maps at 1.4 GHz show that the emission arises mostly from the nebula (see left panels in Fig. 2.1). The central object is not detected. Two are the possible causes: the spectral index of stellar winds ($\alpha_{theoretical} \sim 0.6$) implies low flux density at low frequencies and the confusion limit of the interferometer at this frequency. The spur-emission in the north-east of the nebula first noticed by Higgs, Wendker, & Landecker (1994) is visible.

The lowest-resolution image at 5 GHz shows the emission from the central object, which is likely a stellar wind, as well that from the nebula and from the spur (see Fig. 2.1, top right panel). The highest-resolution maps reveal a highly structured texture of the nebula (see middle and bottom right panels in Fig. 2.1 and again Fig. 2.7). The extragalactic source detected by Higgs, Wendker, & Landecker (1994) is also visible in our maps (circle "a" in Fig. 2.7) and it is overlaid on the nebula in the north-west part of the nebula. Since our final image at 5 GHz has a spatial resolution comparable to that of the *Spitzer* observations, we will refer more often to the 5 GHz dataset for the comparison between the ionized gas and the dust spatial distributions (Section 2.5).

The morphology of the radio nebula is evident in our EVLA multi-configuration image at 6 cm, which reveals a well defined shell-like structure whose overall shape was

previously reported by Higgs, Wendker, & Landecker (1994). Thanks to the improved quality of our image, shown in Figure 2.7, we can discern finer details of the ionized gas distribution. There is evidence of interaction between G79.29+0.46 and the surrounding interstellar medium: i.e., the bright frontal structures in the north-east and the south-west regions of the nebula that delineate regions where the shell structure is locally modified. In particular, the brighter filaments in the south-west region appear to frame the shocked south-western clump observed in CO (compare region "b" in Fig. 2.7 with Fig. 2.8 published by Rizzo, Jiménez-Esteban, & Ortiz 2008; Jiménez-Esteban, Rizzo, & Palau 2010).

The central object is well-detected in the final image, as well as the background object to the north-west (circle "a"). We derived the position, flux density and angular sizes of these components by fitting two dimensional Gaussian brightness distributions. We obtained a flux density of 1.51 ± 0.08 and 1.88 ± 0.09 mJy for the central and background components, respectively. The uncertainty associated with the flux density estimation is given by:

$$\sigma = \sqrt{(RMS_{\rm tot})^2 + (\sigma_{\rm cal} S_\nu)^2} \tag{2.2}$$

where $RMS_{\rm tot}$ is the rms-noise in the map integrated over the area covered by the source, and $\sigma_{\rm cal}$ is the systematic error due to the flux calibrator (typically 3%).

Our derived flux densities are quite similar to those provided by Higgs, Wendker, & Landecker (1994), but our measurements are more sensitive.

The map at 8.46 GHz (Fig. 2.6) obtained using the archival VLA data shows that the array resolved out almost all the extended emission of the nebula: only the most compact nebular features are detected. The central object is bright as expected in the case of a stellar wind at 8 GHz. In order to determine its flux density we have fitted a Gaussian around the source. As a result we found $S(8.46\,\mathrm{GHz}) = 2.35 \pm 0.19$ mJy, where the error is determined as in equation (2.2).

Using this value and the measurement at 6 cm, we derived the spectral index of the central object and its error as in the following

$$\alpha = \frac{\log(\frac{S(8.44\,\mathrm{GHz})}{S(4.96\,\mathrm{GHz})})}{\log(\frac{8.44}{4.96})} \tag{2.3}$$

and

$$\Delta\alpha = \frac{\sqrt{\left(\frac{\sigma(8.44\,\mathrm{GHz})}{S(8.44\,\mathrm{GHz})}\right)^2 + \left(\frac{\sigma(4.96\,\mathrm{GHz})}{S(4.96\,\mathrm{GHz})}\right)^2}}{\log(\frac{8.44}{4.96})} \tag{2.4}$$

Hence we find $\alpha = 0.83 \pm 0.18$, which is consistent with a stellar wind ($\alpha_{theoretical} = 0.6$). With this value we confirm that the central object detected is a stellar wind from the

candidate LBV G79.29+0.46. Previously, through their observations at 8.44 GHz, Higgs, Wendker, & Landecker (1994) derived a spectral index of 1.39 ± 0.14 between 4.86 and 8.44 GHz. They pointed out that, even though this spectral index is steeper than the canonical 0.6, it is still consistent with mass-loss from a stellar object. With our estimate, now we can confirm it.

2.3.2 GBT maps

The map at 1.4 GHz (Fig. 2.2) is strongly limited by confusion: the nebula is not resolved and it is impossible to discern it from the close HII region DR15 in the south of G79.29+0.46. In the 5 GHz map (Fig. 2.3), instead, the nebula is detected and partially resolved.

2.3.3 Final GBT&EVLA maps

The final image at 1.4 GHz, obtained by combining the single-dish and interferometric data (as described in Section 2.2.2 and shown in Figure 2.4), does not show great improvements, possibly because of the confusion limit of the GBT map. As a result, it is a bit more noisy than the EVLA:D&C map.

In terms of dynamical range, the final image at 5 GHz (Fig. 2.5) is also less sensitive than the original EVLA maps. The background emission due to the close HII region DR15 or due to the Cygnus-X complex affects our estimate of the rms-noise in the map. We want to stress the fact that because of the complexity of the map, it is difficult to establish a region where to evaluate the rms-noise. This means that values listed in Table 2.3 are very probably overestimated. Conscious of this, we have measured the flux density over the nebula by using the package *Skyview*, which allows to subtract from the integrated flux density the average background emission that affects the measure. In particular, we integrated over a circle of radius 2.16 arcmin at 1.4 GHz and over a circle of 1.97 arcmin at 5 GHz. We evaluated the background emission in annuli close to the nebula. The uncertainty was derived as the standard deviation (*st dev*) in such annuli multiplied by the area of the source in steradians. The values found are $S(1.4GHz) = 367 \pm 100\,\mathrm{mJy}$ and $S(5GHz) = 298 \pm 131\,\mathrm{mJy}$.

The GBT+EVLA:D&C map at 5 GHz presents the same features already described in Subsection 2.3.1 but together with a diffuse emission, which "fills" empty spaces of the original EVLA maps.

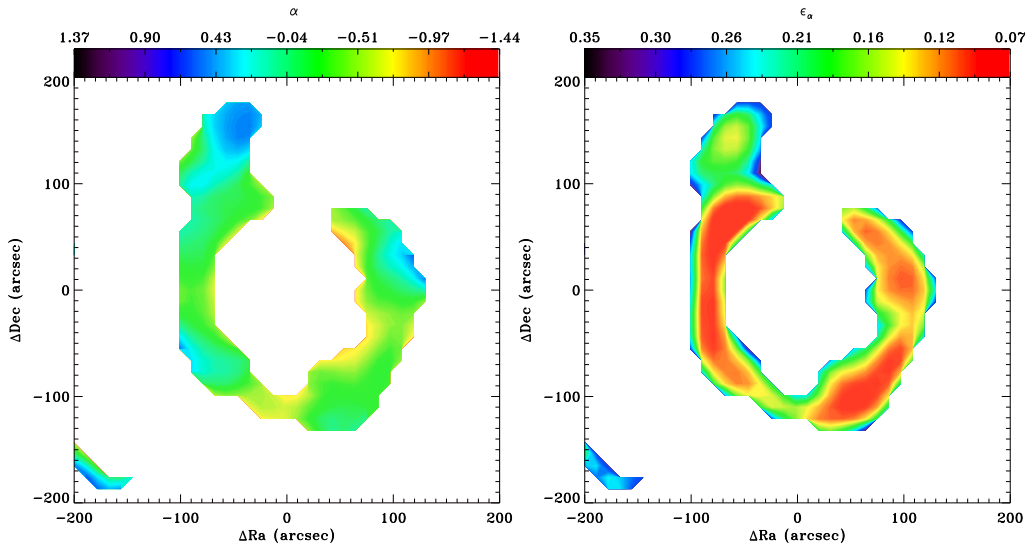

Figure 2.9: Left: Spectral index map of G79 between 1.4 and 5 GHz. Right: Error spectral index map.

2.4 Analysis of the radio continuum

2.4.1 Spectral index

To better understand the nature of the radio nebula, we have created a spectral index map between the EVLA:D&C 1.4 and 5 GHz maps (respectively bottom left and bottom right in Fig. 2.1). We chose these maps because they have comparable LAS (see Table 2.3). Before calculating the spectral indeces, we have re-gridded map at 5 GHz to the same grid of 1.4 GHz. Then we have converted the maps (originally in unit of Jy beam^{-1}) to Jy pixel^{-1}, dividing for the number of pixels contained in the area of a beam:

$$\Omega = \frac{\pi}{4}\frac{(HPBW)^2_{[\mathrm{arcsec}]}}{pixel^2_{[\mathrm{arcsec}]}ln2} \tag{2.5}$$

where $(HPBW)^2$ is 4.56” $\times$ 3.09” in the map at 5 GHz and 26.84” $\times$ 24.65” in the map at 1.4 GHz. The pixel is the same in both the maps after the regridding. Then we deconvolved the maps from their initial beams and reconvolved with a final beam of 27” $\times$ 25”. This operation is equal to the convolution with a gaussian beam with $\sigma^2 = \frac{1}{8ln2}(HPBW_i^2 - HPBW_f^2)$. In each pixel the spectral index map is given by

$$\alpha = \frac{log\left(\frac{imC}{imL}\right)}{log\left(\frac{4.959}{1.391}\right)} \tag{2.6}$$

Considering the error for the flux $\varepsilon = \sqrt{rms^2 + \sigma_{cal}^2 I_\nu^2}$ (in unit of Jy pixel^{-1}), where σ_{cal} is the error due to the uncertainty of the calibrator flux[3], we have also estimated the

[3]Here it was chosen equal to 3% at 5 GHz and 5% at 1.4 GHz.

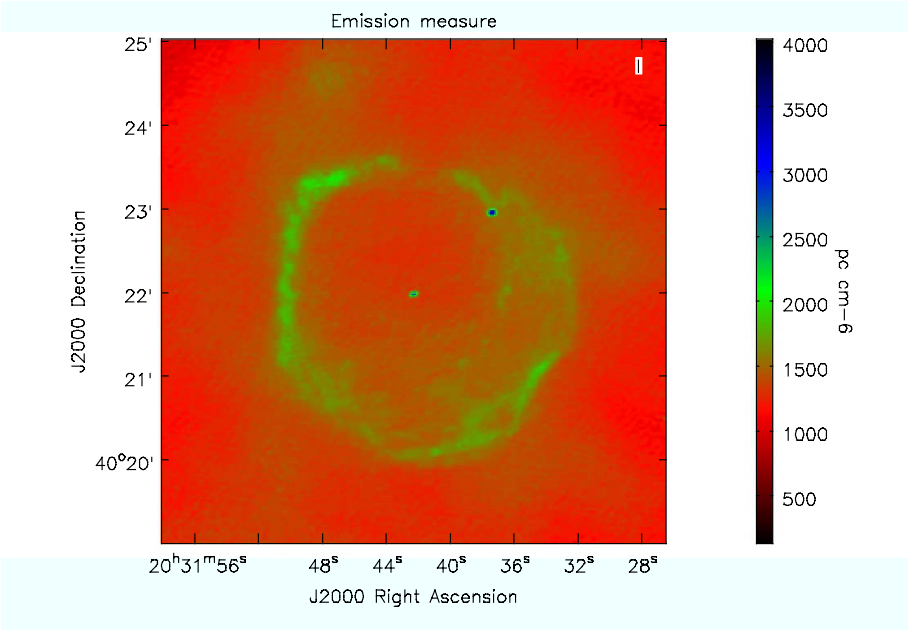

Figure 2.10: Emission measure map from the combined EVLA and GBT 5 GHz data.

error spectral index map, as

$$\varepsilon_\alpha = \frac{\sqrt{(\frac{\varepsilon_C}{imC})^2 + (\frac{\varepsilon_L}{imL})^2}}{log\left(\frac{4.959}{1.391}\right)} \tag{2.7}$$

The spectral index and error maps are plotted in Fig. 2.9.

Over the nebula, the average spectral index $< \alpha >$ is -0.29 ± 0.15[4], consistently with an optically thin nebula emitting free-free radiation. However, it varies slightly in some interesting regions. For example, in the south-west part of the nebula, $\alpha = -0.18 \pm 0.14$, which is still consistent with optically thin free-free but slightly higher than $< \alpha >$ and this is compatible with a modified region due to shock (Fig. 2.8, Jiménez-Esteban, Rizzo, & Palau 2010). On the "spur-region" the maximum value of α is 0.55, with an error of 0.17. This value is usually consistent with stellar winds but in this case it is more likely due to emission from a density clump with a turn-over frequency between the considered frequencies.

2.4.2 EM and ionized mass

Once known the nature of the radio nebula, we can estimate its average electron density and its ionized mass.

In the assumption of optically thin free-free emission not absorbed along the line of sight, the optical depth is given by the ratio between the observed brightness and the

[4]In the lower limit, $< \alpha >$ is -0.44, which indicates very likely that the interferometer filters out flux at 5 GHz.

blackbody emission

$$\tau = \frac{I}{B} \tag{2.8}$$

In the radio domain $h\nu \ll KT$ and the Planckian B is approximated to the Rayleight-Jeans limit

$$B = 2\frac{\nu^2}{c^2}kT_e \tag{2.9}$$

For a nebula of H, with a temperature about 10^4 K, the optical depth is also

$$\tau_\nu = \int \kappa_\nu dl = 8.24 \times 10^{-2} \left(\frac{T_e}{\mathrm{K}}\right)^{-1.35} \left(\frac{\nu}{5\,\mathrm{GHz}}\right)^{-2.1} \frac{EM}{\mathrm{pc\,cm^{-6}}} \tag{2.10}$$

where the Emission Measure (EM) is

$$EM = \int_0^s n_e^2 ds\,[\mathrm{pc\,cm^{-6}}] \tag{2.11}$$

Therefore we can use the optical depth map as determined from equation (2.8) to obtain the emission measure and hence the average electron density from the radio measurements.

In the specific case, B was calculated in Jy pixel^{-1} as

$$B = 2\frac{\nu^2_{[\mathrm{Hz}]}}{c^2}KT_{e[\mathrm{K}]}\frac{(pixel_{[\mathrm{arcsec}]})^2 10^{23}}{206265^2} \tag{2.12}$$

For this analysis we refer to the final image at 5 GHz (Fig. 2.5) obtained by combining the GBT and the EVLA:D&C, as it covers the large and the small angular scales of the region.

Before calculating the optical depth map, we have converted the map from unit of Jy beam^{-1} to Jy pixel^{-1}, dividing for the number of pixels contained in the area of a beam, as in equation (2.5) where in this case $(HPBW)^2$ is 4.56" $\times$ 3.09" and the pixel is 1.3" $\times$ 1.3" in the map at 5 GHz.

The emission measure map obtained with this method is shown in Figure 2.10.

The averaged value for $< EM >$ over the nebula is 1540 pc cm^{-6}. In order to calculate also the electron density is needed to establish the geometrical depth of the nebula.

Considering the shape of the nebula, one possibility is that it is a torus. Since the inner and outer radius vary slightly, we consider average values, for instance $< R_{in} >= 75$" (which corresponds to 0.62 pc at a distance of 1.7 kpc) and $< R_{out} >= 110$" (0.9 pc). Hence we assume a depth of 35" for the shell (0.29 pc). With these values and $< EM >$, we find an average electron density $< n_e >$ of 73 cm^{-3}.

The ionized mass, evaluated as the total amount of particles in the torus volume,

$$M_{ion} = n_e V \frac{m_p}{\mathrm{M_\odot}} \tag{2.13}$$

is 3.84 $M_\odot$, with $V = 6.3 \times 10^{55}\,cm^3$.

If the geometry of the nebula is spherical, with radius $R = 110$", then the electron density is 41 cm^{-3} and the estimated ionized mass is 3.17 $M_\odot$ in a volume of $V = 9.2 \times 10^{55}\,cm^3$.

2.4.3 Current-day mass-loss and spectral type of the star

Since the emission from the central object is due to stellar wind (as shown in Section 2.3.1), from the measured flux density (Section 2.3.1) it is possible to estimate the mass-loss rate of the star, following Panagia & Felli (1975):

$$\dot{M} = 6.7 \times 10^{-4} v_\infty F_\nu^{3/4} D^{3/2} (\nu \times g_{ff})^{-1/2} [M_\odot\,yr^{-1}] \tag{2.14}$$

where full ionization and cosmic abundances have been assumed, F_ν=1.51 mJy is the observed radio flux density at 5 GHz, $v_\infty = 110\,km\,s^{-1}$ (Voors et al. 2000) is the terminal velocity of the wind, $D = 1.7\,kpc$ (Jiménez-Esteban, Rizzo, & Palau 2010) and

$$g_{ff} = 9.77 \left(1 + 0.13 \log \frac{T_e^{3/2}}{\nu}\right) = 5.08 \tag{2.15}$$

at 5 GHz for a gas with electron temperature of $T_e = 10000\,K$. The free-free *Gaunt* factor $g_{\rm ff}$ is approximated as in Leitherer & Robert (1991).

With these values, the mass-loss rate is $1.4 \times 10^{-6}\,M_\odot\,yr^{-1}$. As pointed out by Vink et al. (2008), G79.29+0.46 may be associated with the nearby DR15 region rather than with Cyg OB2. If this is the case, G79.29+0.46 is likely to be closer, at about 1 kpc. Since mass-loss scales with the distance as $D^{3/2}$, this would imply a reduced mass-loss of a factor 0.45. These values are consistent with previous evaluations obtained by other authors using different techniques (e.g., Waters et al. 1996).

Once we have evaluated the ionized mass in the nebula (as in the previous subsection), we can provide an estimate of the ionizing photon flux from the star F_{UV}, as

$$F_{UV} = \frac{M_{ion} < n_e > \beta_2}{m_{p_{[M_\odot]}}} \tag{2.16}$$

Assuming $< M_{ion} >$=3.5 $M_\odot$, $< n_e >= 57\,cm^{-3}$ (average values obtained by the two assumed geometries), $\beta_2 = 3 \times 10^{-13}\,cm^3\,s^{-1}$, $m_{p_{[M_\odot]}} = \frac{1.67 \times 10^{-24}}{1.99 \times 10^{33}}$, we find $\log F_{UV} = 46.85$, which corresponds to a spectral type from B1 to B0.5 (Panagia 1973), consistently with Voors et al. (2000).

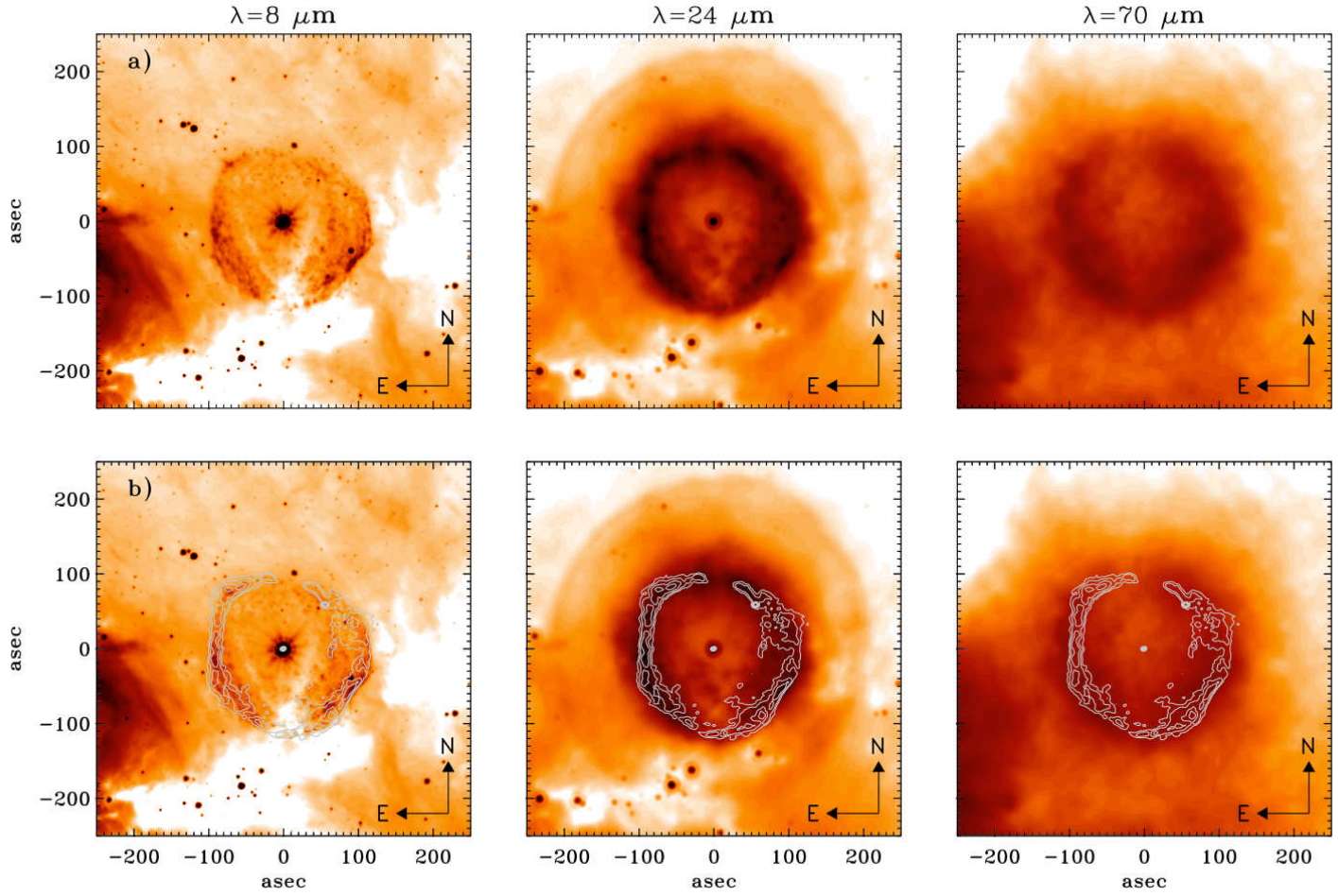

Figure 2.11: Panel a: The 8 μm IRAC (right), the 24 μm (center) and the 70 μm (left) MIPS maps of G79.29+0.46. Panel b): the same as panel a, but the EVLA 6 cm map (white contours) superimposed. To better point out the major radio features, only contours starting from 10% of flux density of the central radio sources have been drawn. For each map, the field of view is $4.2' \times 4.2'$ centred on the LBV position. Figure as in Umana et al. (2011b).

2.5 Ionized component versus dust components

As mentioned before, for the comparison with the *Spitzer* images, we will refer to the 5 GHz map, which has a resolution comparable with the IR images.

The 8 μm IRAC and 24 and 70 μm MIPS images of G79.29+0.46 are shown in Figure 2.11a. Previous versions of these images were presented by Kraemer et al. (2010) and Jiménez-Esteban, Rizzo, & Palau (2010), who both pointed out the presence of a second larger radius shell in the 24 μm image. Our reprocessed maps confirm the existence of the second 24 μm shell and, thanks to our improved reduction, also provide a hint of its presence at 70 μm. The overall distribution of the dust is similar in the 24 and 70 μm maps, consistently with at least two nested dusty shells surrounding the LBV. On the contrary, in the 8 μm map where a major contribution from warm dust is expected, the dust appears to be more concentrated in two south-west and south-east regions.

Our radio observations allow, for the first time, a morphological comparison between the ionized gas and the dust. In Figure 2.11b, the same maps are shown but now with the 6 cm EVLA map superimposed using white contours. We can notice that, while the nebular emission at both 24 μm and 70 μm is more extended than the ionized gas (radio nebula), the 8 μm emission appears well-contained within the ionized part of the nebula. Moreover, while the radio emission from the nebula is incomplete in the north region, the emission at 24 μm and 70 μm has a more uniform distribution.

The apparent lack of dust in the southern regions in both 8 μm and 24 μm are perhaps due to an absorption effect caused by the infrared dark cloud (IRDC) which may be located in front of the the southern region of the nebula. The IRAC and MIPS images appear to probe, then, different populations of dust. To better visualize the spatial distribution of the ionized gas relative to the dust, we have extracted surface brightness profiles along cuts through the nebula from the 6 cm, 24 μm and 70 μm maps. However, a direct comparison can be performed only between the 6 cm and the 24 μm maps, as they share a comparable angular resolution, ~ 4.6" for the 6 cm EVLA versus ~ 6" for the 24 μm MIPS map. A superposition of the 6 cm EVLA map on the 24 μm map is shown in Figure 2.12. We extracted eighteen cuts from each map and determined an azimuthally-averaged source profile, shown in (Figure 2.13). The radio shell has a smaller thickness and a sharp decreasing trend in the outer part of the nebula. The dust nebula is more extended and shows a smoother distribution in the outer regions.

The inner shell peak is at ± 100" from the central object. The second shell is clearly evident in the 24 μm profile, at a distance of about ± 200" from the centre. At the same distance, less defined peaks are visible in the 70 μm profile, smoothed out by the coarser

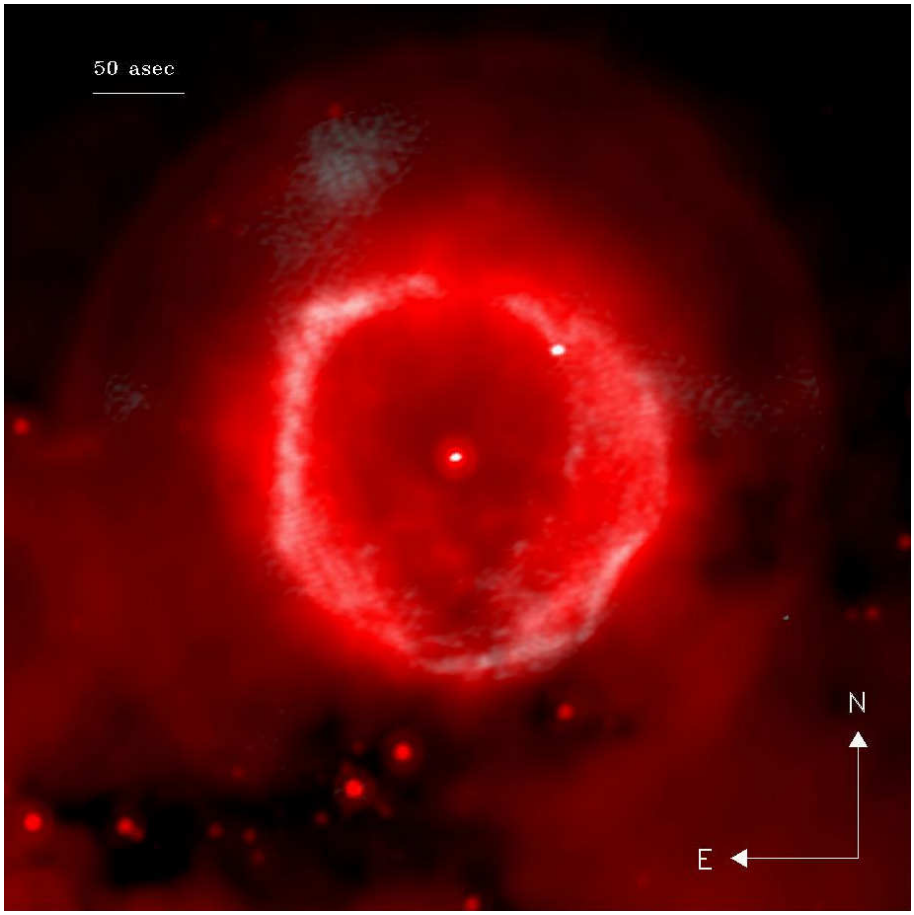

Figure 2.12: 6 cm EVLA map of G79.29+0.46 (grey) superimposed to the MIPS 24 μm map (red). The field of view is $3.5' \times 3.5'$ centred on the LBV position. Figure as in Umana et al. (2011b).

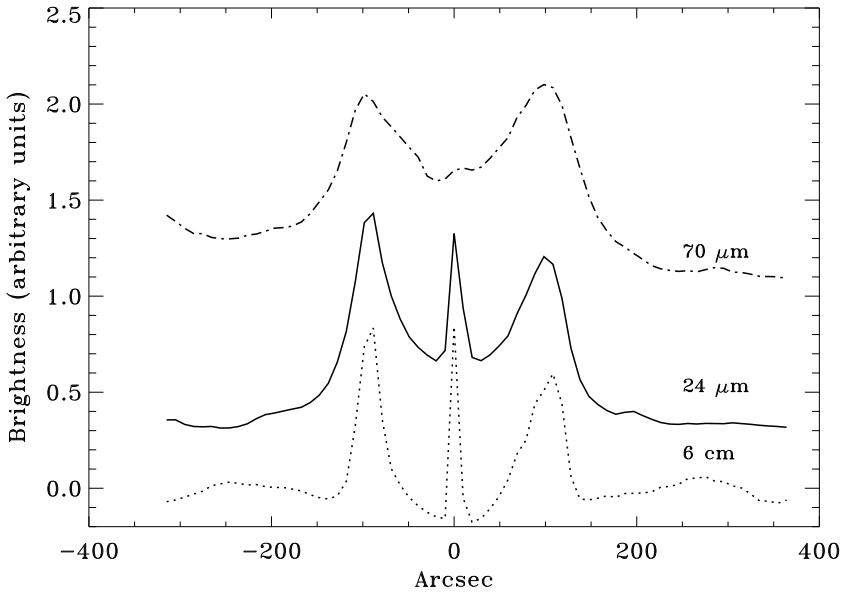

Figure 2.13: Averaged profiles through the nebula at 6 cm (dotted line), 24 μm (continuous line), and 70 μm (dotted slash line). Each profile has been obtained from 18 individual cuts in the corresponding map and has been shifted vertically by an arbitrary quantity for easier comparison. Figure as in Umana et al. (2011b).

spatial resolution.

The direct comparison of the 6 cm and 24 μm maps (that share comparable spatial resolution) indicates that only part of the inner, brighter nebula is ionized, (i.e. the nebula is ionization bounded). The radio nebula shows a sharper profile, depicting regions where probable interaction between the second and the first dusty shells is taking place. This is evident in several regions, most notably in the north-east and in the south-west part of the nebula, where the overall quite regular shell-like morphology is locally disturbed.

2.5.1 Determination of the nebula kinematical age

The dust emission peaks can be related to the epoch when mass-loss took place. Assuming a distance of 1.7 kpc for the star (Schneider et al. 2006; Rizzo, Jiménez-Esteban, & Ortiz 2008), this corresponds to a linear distance of 0.82 pc and 1.64 pc, respectively. This implies, assuming a shell expansion velocity of $\sim 30\,\mathrm{km\,s^{-1}}$ (Waters et al. 1996), that the two mass-loss episodes occurred at most 2.7×10^4 and 5.4×10^4 years ago, or 1.6×10^4 and 3.1×10^4 years ago, if a distance of 1 kpc is used, as suggested by Vink et al. (2008). The timespan for these two violent episodes is of $\sim 2 \times 10^4$ yr. Our results point out that mass-loss can occur in different episodes, for which we derived characteristics timescales, and pose quite strong constraints that stellar evolution models must taken into account (Umana et al. 2011b).

With the current-day mass-loss rate determined in the previous section ($\dot{M} = 1.4 \times 10^{-6}\,\mathrm{M_\odot yr^{-1}}$), the mass ejected in the nebula in the derived timescale of $5.4 \times 10^4\,\mathrm{yr}$ will be of 0.076 $\mathrm{M_\odot}$ and in a time of $3.1 \times 10^4\,\mathrm{yr}$ about 0.043 $\mathrm{M_\odot}$. These estimations are smaller at least two order of magnitudes than the value found in Subsection 2.4.2. This implies that an enhanced mass-loss rate took place to form such a massive nebula, i.e. current-day mass-loss rate can not explain the observed mass. Waters et al. (1996) reported, examining IRAS images, that the nebulae were ejected with a mass-loss rate of $\sim 5 \times 10^{-4}\,\mathrm{M_\odot yr^{-1}}$. By considering our results, we suggest instead an average mass-loss rate of $6.5 \times 10^{-5}\,\mathrm{M_\odot yr^{-1}}$, which is a very common value for LBVs.

2.6 Discussion

In this chapter we presented new radio EVLA and GBT observations of the nebula surrounding the LBV G79.29+0.46. For the first time, we compared the radio emission, which traces the spatial distribution of the ionized gas, with maps recently obtained in the mid-IR, which probes the spatial distribution of the dust component.

Analysis of our improved radio images of G79.29+0.46 and its associated nebula has

allowed us to determine physical properties of both the star and the nebula. Regarding the central object, we have found a spectral index (~ 0.8) which is more consistent with a stellar wind than the value found previously by Higgs, Wendker, & Landecker (1994). We determined the current-day mass-loss ($\sim 1.4 \times 10^{-6}\,M_{\odot}yr^{-1}$) and the current spectral type of the star (B1-B0.5), which is consistent with its position in the H-R diagram provided by Smith, Vink, & de Koter (2004) (see Fig. 1.4). Our estimate of the nebula ionized mass ($M \sim 3.5\,M_{\odot}$) is of the same order of magnitude of the value provided by Higgs et al., but obtained with a different technique. The spectral index analysis on the nebula revealed us that it is consistent with optically thin free-free emission, except in the "spur-emission" region, where the gas is likely denser. Moreover, our radio maps provided us with evidence that the ionized shell is locally modified by interaction with the IRDC in the south-west.

Among other interesting results, the dust distribution observed at 8 μm appears different than the distribution at 24 and 70 μm, revealing the existence of two dust components: a cooler component traced by the 24 and 70 μm emission, and a warmer dust component, probably consisting of smaller grains, traced by the 8 μm emission.

Thanks to a collaboration with the MIPSGAL team, we analysed the MIPS 70 μm map, constructed using the most updated pipeline, and not available in the data archive in the improved version. This map reveals the presence of a second shell very similar to that seen at 24 μm. Such cool component emitting at the longer IR wavelengths is a footprint of an earlier mass-loss episode experienced by the star, as first suggested by Kraemer et al. (2010).

Nebular lines and dust continuum are the main possible contributors to the 24 μm emission from objects embedded in a dusty nebula with a hot central component. This, together with the lack of any prominent emission-line falling within the response curve of the MIPS 24 μm band, as evident from the low-resolution IRS spectrum of the shell (Jiménez-Esteban, Rizzo, & Palau 2010), leaves very little doubt that the shell emission is entirely due to thermal dust emission.

The fact that there are at least two nested shells provides strong constraints on the the origin of the nebula: it is evident that the dusty shells consist of material ejected by the central object in different mass-loss episodes, and not of swept-up ISM material, as instead suggested by Higgs, Wendker, & Landecker (1994).

Analysis of the infrared nebulae around G79.29+0.46 will be discussed in the next chapter.

Acknowledgments

This work is based in part on observations made with the *Spitzer* Space Telescope, which is operated by the Jet Propulsion Laboratory, California Institute of Technology under a contract with NASA. Support for this work was provided by NASA through an award issued by JPL/Caltech, which allowed the author of this thesis to work with the IPAC team for four months.

The EVLA and the GBT are telescopes of the National Radio Astronomy Observatory (NRAO), which is a facility of the National Science Foundation operated under cooperative agreement by Associated Universities, Inc.

Chapter 3

Multiwavelength analysis of the nebula around G79.29+0.46

Abstract

We present a multiwavelength study of the gas and the dust in the nebula around cLBV G79.29+0.46, covering a spectral range from 3 to 160 μm. We analyse the chemical composition of the nebula from *Spitzer*/IRS and *ISO*/LWS and SWS spectra and derive electron densities at different radii from the central star by analysing different line ratios. The values found can be compared with those estimated from analysis of the high-ionized gas, but also allow us to probe the low-ionization potential components of the gas. We also present for first time high-resolution far-IR images, obtained very recently with the space telescope *Herschel*. A photometric analysis of archival IR images is also discussed. From the measured flux densities we determine physical parameters (temperature and mass) related to the dust components. Finally, we model the nebula and the star emission with the code CLOUDY, using as input parameters those estimated from our infrared and radio analysis.

3.1 Introduction

Even though G79.29+0.46 is as yet only a candidate LBV, it appears to be an ideal object to study, for both its proximity and its size. Thanks also to its location in the star forming region Cygnus-X, data archives are full of spectroscopic and photometric datasets, from the UV to the far-IR, probing the stellar component and the nebula. Since we are interested in LBV ejecta, we have retrieved from the archives almost all the datasets at wavelengths ranging from the mid-IR to the far-IR.

Among the datasets acquired with very different instruments, many of them have been discussed only qualitatively in the literature. Here we provide a quantitative analysis,

which leads us to new results.

One of the most challenging aspects of this source, as we saw in the previous chapter, is related to its surroundings, which are rich in interstellar dust and gas. The background (or even foreground) problem becomes more important with increasing wavelength. In particular the environment consists of the radiation originating from the HII region complex called DR15 and from the Cygnus Rift.

In this chapter we first describe all the archive datasets considered in our study (Section 3.2). Then we present our analysis of the mid-IR spectra (Section 3.3) aimed at deriving line ratios useful for electron density diagnostics. In Section 3.5 we analyse the mid-IR images to determine physical properties of the dust components, already presented in the previous chapter. Hence we discuss our photometric analysis in the IR, which we then complement with the radio flux density measurements, in order to compare this information with a model of the Spectral Energy Distribution (SED) obtained in this work with the photoionization code CLOUDY (Section 3.6). Finally, in Section 3.7 we discuss our results.

3.2 The datasets

In order to study different emitting components in the nebula around G79.29+0.46, we have retrieved almost all the data available in the archives, which were obtained in different projects. The considered datasets are summarized in Table 3.1. We present for first time new far-IR images, obtained very recently with the PACS and SPIRE photometers on board of *Herschel*.

The *Spitzer* IRAC and MIPS maps have already been published (Kraemer et al. 2010; Jiménez-Esteban, Rizzo, & Palau 2010; Umana et al. 2011b) and reprocessed in this work as described in Chapter 3.

The ISOPHOT map at 25 μm was presented by Wendker et al. (1998) together with the *ISO* LWS spectra, but they provided only a qualitative discussion of the data and did not consider the poor sensitive 60 and 105 μm maps. The ISOCAM images are briefly discussed in the poster paper of Trams, Voors, & Waters (1998).

The *ISO* SWS spectra appeared for first time in the proceeding of Morris, Morris, & Spitzer WRRINGS Team (2008), but they were not analysed neither discussed. Conversely, for the *MSX* images we did not find any works in the literature.

The IRS spectra were already analysed by Jiménez-Esteban, Rizzo, & Palau (2010) but, despite the interesting study which the authors proposed, they did not consider the off-nebula dataset and hence they did not subtract the background, which instead strongly

Table 3.1: Archival data summary.

Telescope	Instrument	λ (μm)	Project ID
		Photometric data	
Herschel	PACS	70, 100, 160	N/A[a]
Spitzer	IRAC	8	AOR 6050560
Spitzer	MIPS	24, 70	AOR 22508544
MSX	SPIRIT III	8.28, 12.13, 14.65, 21.3	N/A
ISO	CAM01	8.69, 8.99, 9.98, 11.48 12.41, 12.82, 13.53, 15.58, 15.96	TDT35700630
ISO	PHT03	25	PSP 38101802
ISO	PHT32	60, 105	PSP 35201501
		Spectroscopic data	
ISO	SWS06	12.2-13.2	SWS69200901
ISO	SWS06	17-27; 30-34	SWS76802901
ISO	SWS06	34-35	SWS51705105
ISO	LWS02	41.14-178.75	LWS35801003
ISO	LWS02	41.14-178.75	LWS35801005
ISO	LWS02	41.14-178.75	LWS35801007
ISO	LWS02	41.14-178.75	LWS35801008
ISO	LWS02	41.14-178.75	LWS35801011
ISO	LWS02	41.14-178.75	LWS35801014
Spitzer	IRS/SL-LH-SH	5.2-14.5, 18.7-37.2	AOR17333248
Spitzer	IRS/SL-LH-SH	5.2-14.5, 18.7-37.2	AOR17333504

[a] Images were kindly provided to the author of this work by the IPAC team.

Table 3.2: Summary of photometers properties.

Telescope	Instrument	λ_{cent} (μm)	Bandwidth (μm)	FWHM
Herschel	PACS	70	25	5.5”
Herschel	PACS	100	45	6.7”
Herschel	PACS	160	80	11”
Spitzer	IRAC	7.872	2.905	1.71”
Spitzer	MIPS	23.7	4.7	6”
Spitzer	MIPS	71	19	18”
MSX	SPIRIT III	8.28	3.36	6.8”
MSX	SPIRIT III	12.13	1.72	11.1”
MSX	SPIRIT III	14.65	2.23	13.5”
MSX	SPIRIT III	21.3	6.24	18.2”
ISO	CAM01	8.69	0.197	3”
ISO	CAM01	8.99	0.20	3”
ISO	CAM01	9.99	0.26	3.4”
ISO	CAM01	11.48	0.28	4”
ISO	CAM01	12.41	0.29	4.3”
ISO	CAM01	12.82	0.29	4.4”
ISO	CAM01	13.53	0.298	4.7”
ISO	CAM01	15.58	0.31	5.4”
ISO	CAM01	15.96	0.32	5.5”
ISO	PHT03	25	9.1	8.6”
ISO	PHT32	60	25.9	20”
ISO	PHT32	105	39.6	36”

affects the target continuum and line emissions. Moreover, they did not apply corrections for extinction in their diagnostic study. Hence we propose a new analysis.

3.2.1 *Herschel* images

Images at position of G79.29+0.46 have been extracted from HOBYS maps. The “Herschel imaging survey of OB Young Stellar objects” (HOBYS, P.I. Motte F.) is a key project of the *Herschel* satellite, aimed at mapping star forming regions at distance $\sim$ 3 kpc from the Sun. The Cygnus-X region was observed using 2 PACS and 3 SPIRE photometric bands. The observations were carried out in parallel mode, using both instruments simultaneously, acquiring images at 70 μm and 160 μm for PACS and at 250 μm, 350 μm, and 500 μm for SPIRE. Typical spatial resolution of these bands are 5.5”, 11”, 18”, 25” and 37”, respectively. *Herschel* data were reduced with a specialized reduction pipeline (Traficante et al. 2011) optimized for data affected by bright and irregular background, as

typical for regions close to or in the Galactic Plane.

The IPAC team also provided the 100 μm PACS image, with a resolution of 6.7", extracted from the *Herschel* program MESS (Mass-loss of Evolved StarS).

3.2.2 *MSX* images

The images acquired by the instrument SPIRITIII, which was on board of the satellite *MSX*, were retrieved by using the IRSA data archive and the on-line Cutout's Service which is a general tool to create single image cutouts of datasets archived at IRSA. The images were obtained in the bands A, C, D and E and have a field of fiew of 18'×18' and a resolution between 6" and 18". Image properties are summarized in Table 3.2.

The maps are in unit of $\mathrm{W\,m^{-2}\,sr^{-1}}$ and for our analysis we converted them in Jy unit, using the conversion factor suggested in `http://irsa.ipac.caltech.edu/applications/MSX/MSX/imageDescriptions.htm`.

3.2.3 ISOPHOT and ISOCAM images

The ISOCAM observations of G79.29+0.46 were performed as a 3 by 3 raster scan with 90" stepsize and were performed on November 7, 1996 (Trams, Voors, & Waters 1998). The pixel size is 6" and the FOV is about 6.2'×6.2'. The FOV in the ISOPHOT images is 11.45'×11.45' but in the case of the 25 μm map, for which it is 8'×5.7'.

The maps were retrieved as basic science products, using the *ISO* Data Archive (IDA) Interface version 11.1.

3.2.4 *ISO* LWS and SWS spectra

The spectral line *ISO*/SWS observations were made in 1997 with the 33"×20" slit in the position of the central source (in the case of the spectrum with sws69200901 the aperture is 27"×14"), while the *ISO*/LWS observations were made with the 84"×"84 slit at six different positions (one on the star position, two on-nebula and three off-nebula). Unfortunately at the time of the *ISO* observations the second infrared shell was not yet discovered and therefore the off-nebula data are actually on the second shell, as evident in Fig. 3.1.

The LWS instrument covers the wavelength range from 43 to 196 μm and has a resolution $R = \lambda/\Delta\lambda$ that varies (depending on the wavelength) from 140 to 330, while the SWS ones cover range from 2.38 to 45.2 μm with R varying from 1000 to 2500. Here we concentrate the analysis on the spectral ranges listed in Table 3.1.

The spectra are plotted in Fig. 3.3 and 3.4.

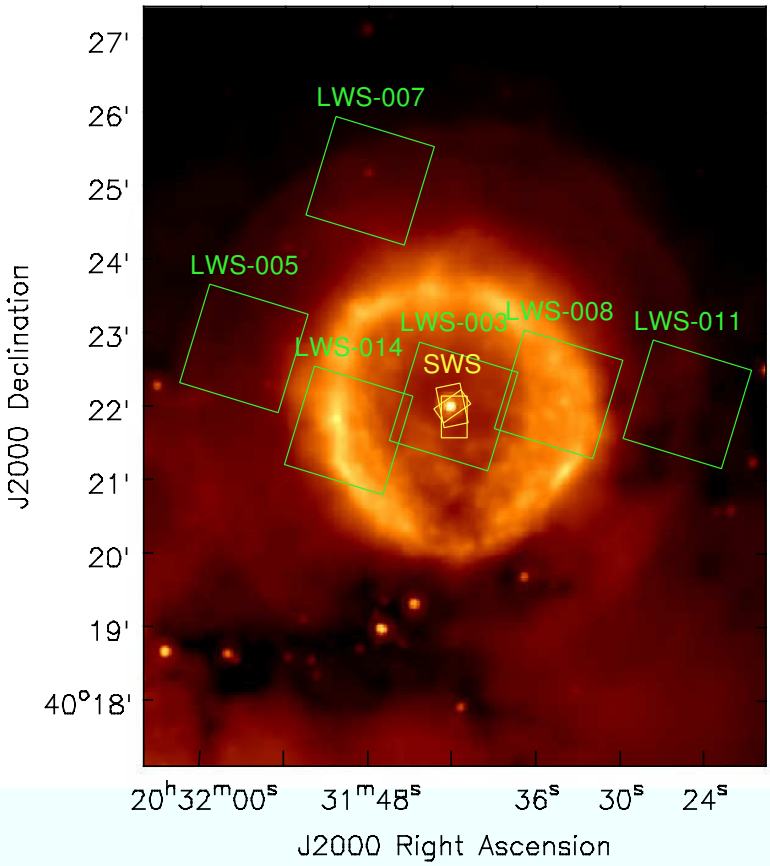

Figure 3.1: MIPS/*Spitzer* 24 μm image of G79.29+0.46 and positions of the LWS/*ISO* (green) and SWS/*ISO* (yellow) slits.

3.2.5 *Spitzer* IRS spectra and IRAC and MIPS images

Spitzer IRS spectra with AORKEY 17333248 were obtained (P.I. Fazio G.) on June 28, 2006, using the following band-passes: Short-High (SH), covering a spectral range from 9.9 to 19.6 μm; Long-High (LH), between 18.7-37.2 μm; Short-Low (SL), between 5.2-14.5 μm. The SH and LH modules were positioned on the central object, covering an area of 4.7"×11.3" and 11.1"×22.3" respectively. The SL module (3.6"×57") was shifted along the SE-NW direction on the nebula to get spectra at each radius. In order to subtract the background emission, off-nebula observations were also performed (AORKEY 17333504) together with the on-nebula and central object observations.

Fig. 3.2 shows the slit positions used in the project described above.

We remind the reader that *Spitzer* IRAC and MIPS images have been already described in Chapter 2.

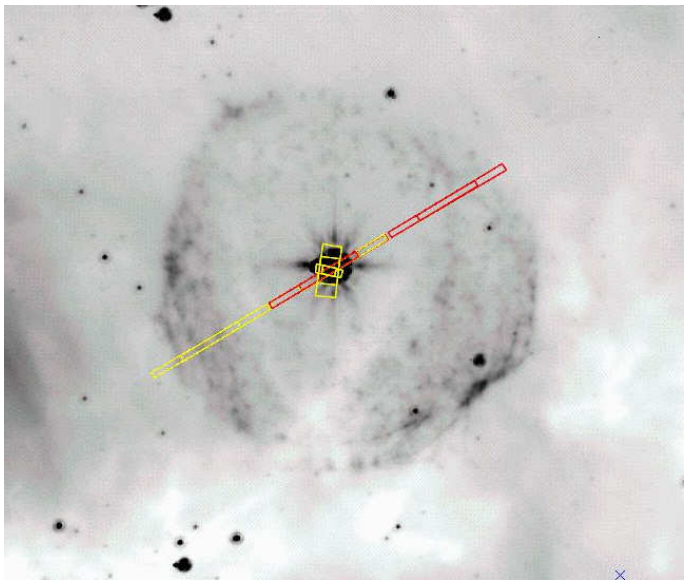

Figure 3.2: IRAC/*Spitzer* 8 μm image of G79.29+0.46 and positions of the IRS-SH and LH/*Spitzer* (center) and IRS-SL/*Spitzer* (nebula) slits.

3.3 Analysis of the mid-IR spectra

In this section we present our analysis of the mid-IR spectra collected by the spectrometers LWS and SWS on board of *ISO* and by the instrument IRS on board of *Spitzer*.

In the case of IRS spectra, we refer to the data obtained after the background subtraction. Data taken at the same channel were also merged in order to work with a spectrum per module.

Since G79.29+0.46 is a heavily reddened object, before to analyse the observed lines, the fluxes must be corrected for extinction along the line of sight. Therefore, we apply the correction to the datasets and then we compare line fluxes before and after the procedure. For the analysis, we will refer only to the corrected fluxes.

3.3.1 Correction for extinction

To evaluate the absorption, we consider as visual extinction the value $A_V = 5.7$ obtained by Albacete Colombo et al. (2007) for OB stars through observations in the X-rays of the Cygnus-X region.

Considering that $\frac{A_K}{A_V} = 0.12$ in the case of a constant total-to-selective parameter $R_V = 3.1$ (typical value for small grains in the Milky Way), then A_K=0.372 and hence the extinction law is $A_\lambda = f(\lambda)A_K$, where $f(\lambda)$ was determined for discrete values of λ

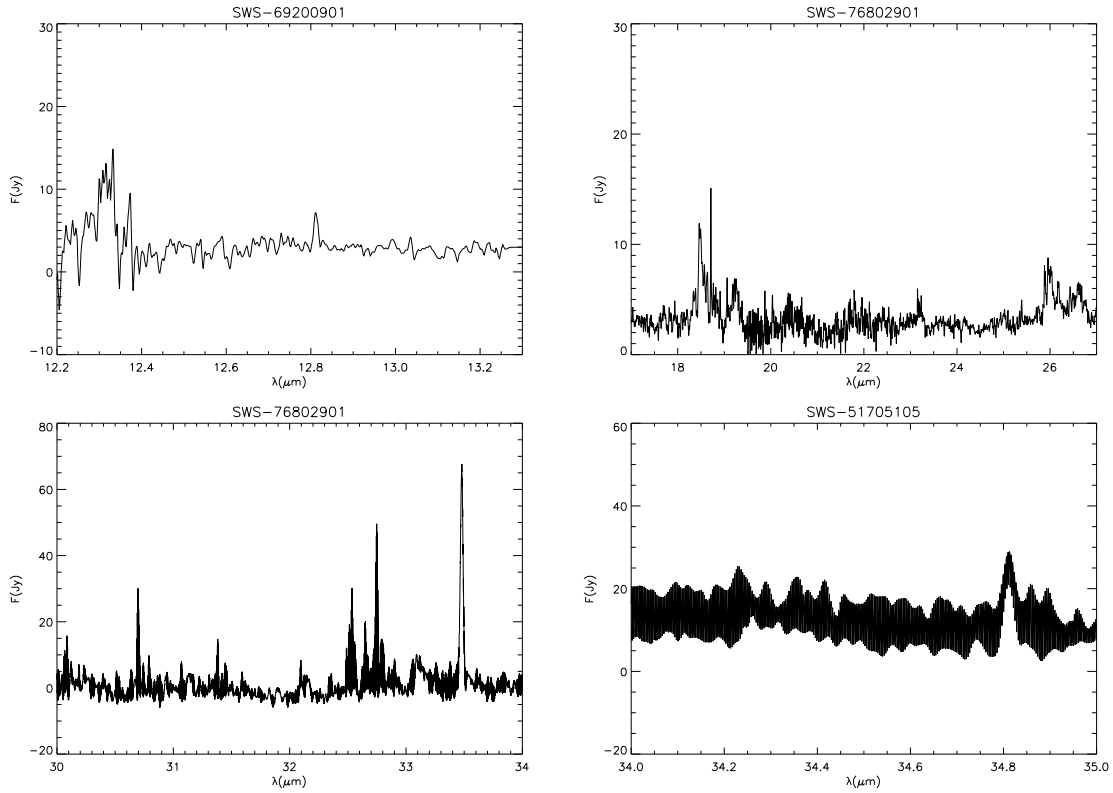

Figure 3.3: *ISO*-SWS spectra taken on the star position as shown in Fig. 3.1.

by Mathis (1990). We used these values and, to correct the line fluxes, we derived A_λ interpolating $f(\lambda)$ at each λ.

Finally, the correction for the flux is given by

$$F_{dereddened} = 10^{\frac{A_\lambda}{0.25}} F_{observed} \tag{3.1}$$

As evident in the tables, interstellar absorption becomes negligible up to 30 μm. On the contrary, at short wavelengths ($\sim 4-18$ μm) the correction is considerable.

We measured line fluxes before and after the extinction correction, as shown in the tables. To derive the fluxes, we used the ISAP package and fitted the lines by using

Table 3.3: SWS line fluxes.

λ_{cent} (μm)	λ_{lab} (μm)	Element	Transition	$F_{observed}$ ($_{10^{-19}}$W cm^{-2})	$F_{dereddened}$ ($_{10^{-19}}$W cm^{-2})	#
12.8121	12.8135	[NeII]	$2P\frac{1}{2}$-$2P\frac{3}{2}$	1.05±0.02	3.2±0.4	sws69200901
18.7123	18.7130	[SIII]	3P2-3P1	1.5±0.1	4.6±0.6	sws76802901
33.4780	33.4810	[SIII]	3P1-3P0	5.4±0.1	6.2±0.2	sws76802901
34.8128	34.8152	[SiII]	$2P\frac{3}{2}$-$2P\frac{1}{2}$	1.3±0.3	1.3±0.1	sws51705105

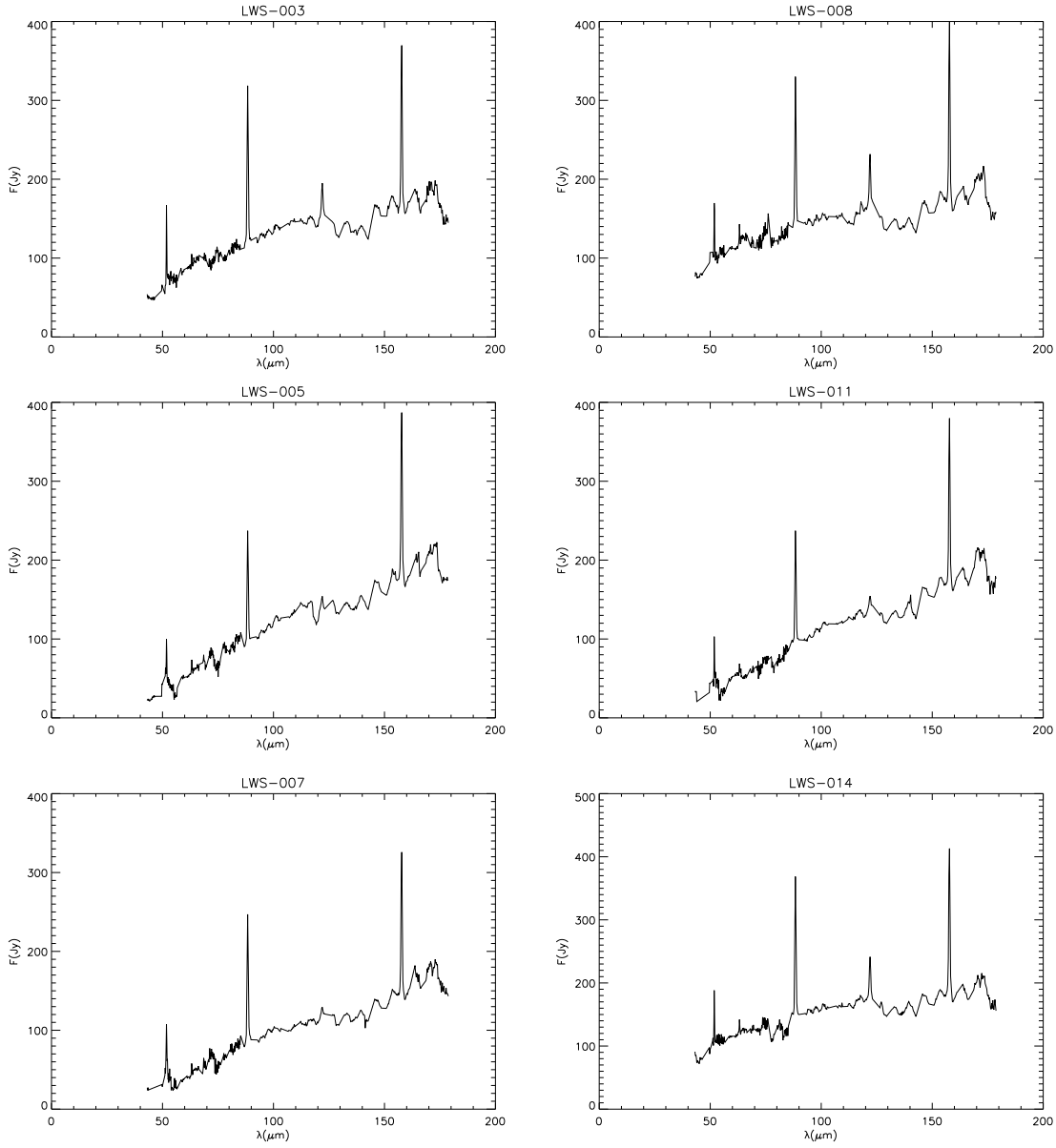

Figure 3.4: *ISO*-LWS spectra taken on the nebula as shown in Fig. 3.1.

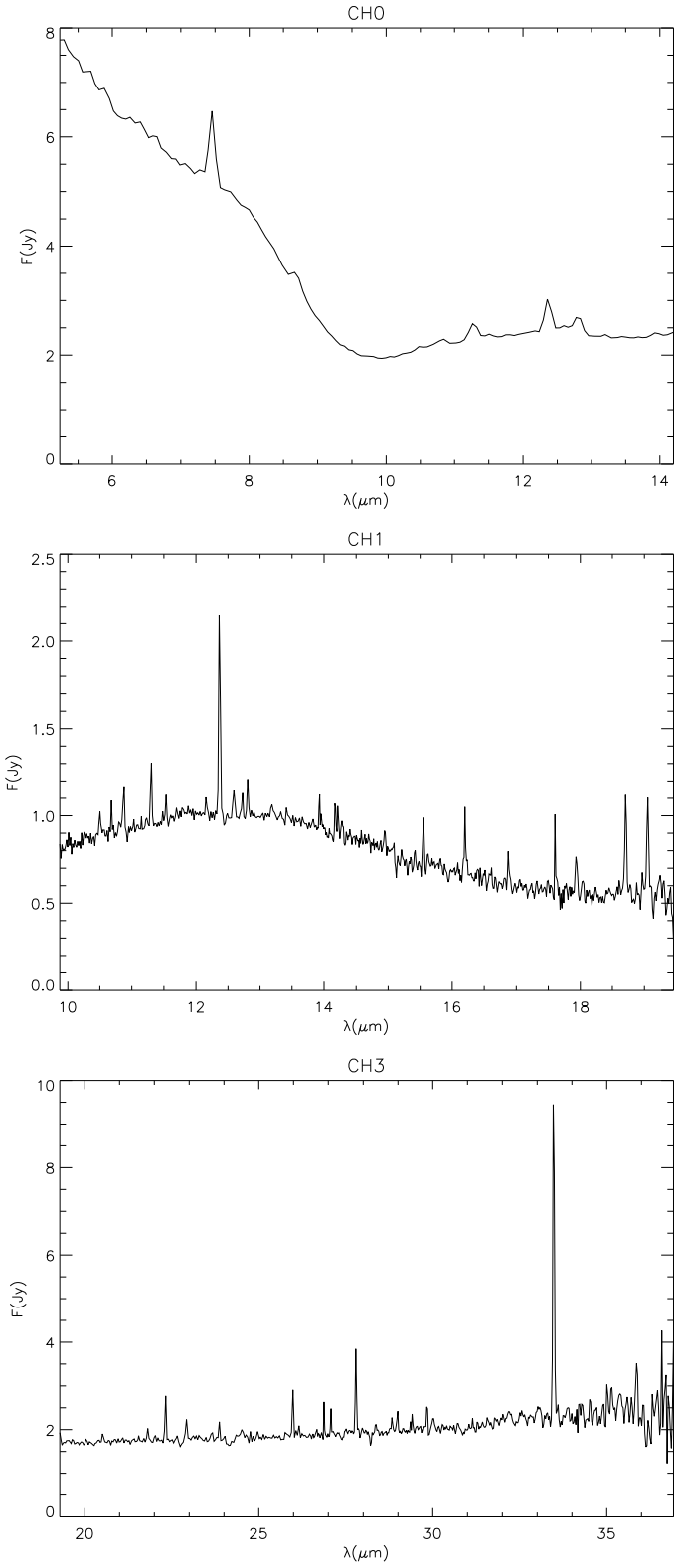

Figure 3.5: IRS SL (CH0), SH (CH1), LH (CH3) spectra after the background subtraction. Data were taken on the star position (CH0) and on the nebula (CH1 and CH3) as shown in Fig. 3.2.

Table 3.4: Derived line fluxes from LWS spectra, obtained at six different position of the slit on the nebula.

λ_{cent} (μm)	λ_{lab} (μm)	Element	Transition	$F_{observed}$ ($_{10^{-19}}$Wcm^{-2})	$F_{dereddened}$ ($_{10^{-19}}$Wcm^{-2})	#
51.8333	51.8145	[OIII]	3P2-3P1	20.1±3.6	28.2±4.8	lws35801011
51.8191				30.8±4.4	55±5	lws35801007
51.7381				38.7±5.5	46±6	lws35801005
51.8234				29.6±2.4	32.6±3.7	lws35801014
51.8471				26±2	28.5±3.1	lws35801008
51.8221				34.4±3.4	38.8±3.4	lws35801003
63.1785	63.1837	[OI]	(3P1-3P2)	4.6±0.8	4.6±1.4	lws35801011
63.1785				3.9±0.3	3.3±1.8	lws35801007
63.2027				3.7±0.8	4.1±1.1	lws35801005
63.1774				5.1±1.2	5.3±1.1	lws35801014
63.1734				5.3±1.8	5.4±2.0	lws35801008
63.1870				3.3±0.3	4.7±2.3	lws35801003
88.4118	88.3560	[OIII]	(3P1-3P0)	40.8±2.7	42±3	lws35801011
88.3803				43.05±1.46	47.7±5.7	lws35801007
88.3960				35±2	37.2±3.6	lws35801005
88.3734				59.4±5.1	61.5±6.1	lws35801014
88.4099				51.2±1.8	51.7±4.2	lws35801008
88.3817				52.2±1.1	53±3	lws35801003
122.1056	121.898	[NII]	(3P2-3P1)	8±1	8.4±2.3	lws35801011
122.0106				3.6±1.2	4.4±1.5	lws35801007
121.6556				4.7±1.7	5.1±1.8	lws35801005
121.9799				12.5±1.5	12.9±2.2	lws35801014
121.9589				14.2±2.5	15±2	lws35801008
121.9886				8.79±0.76	10.0±1.6	lws35801003
157.7338	157.741	[CII]	$2P\frac{3}{2}$-$2P\frac{1}{2}$	17.6±0.1	18.1±2.2	lws35801011
157.7237				15.01±0.35	15.2±1.7	lws35801007
157.7191				18.0±1.5	18.6±1.6	lws35801005
157.7185				20.2±0.6	20.7±1.6	lws35801014
157.7289				18.7±1.2	19.9±2.8	lws35801008
157.7207				17.2±0.4	17.5±1.7	lws35801003

Table 3.5: Line fluxes derived from the IRS/CH3 spectrum, after the background subtraction.

λ_{lab} (μm)	λ_{cent} (μm)	Element	Transition	$F_{observed}$ ($_{10^{-21}}$W cm^{-2})	$F_{dereddened}$ ($_{10^{-21}}$W cm^{-2})
20.5147	20.5207	HI	20-12	6.3±4.0	18.3±11.0
21.8420	21.8065	HI	19-12	6.8±2.8	17.1±8.2
22.3316	22.3191	HI (HeII?)	13-10 (22-18)	24.5±7.7	61.9±14.2
22.9250	22.9165	[FeIII]	5D3-5D4	15.1±5.9	37.5±16.8
23.8680	23.8628	HI	15-11	14.2±4.8	29.3±10.8
25.9883	25.9758	[FeII]	a6D7/2-a6D9/2	24.1±2.9	42.4±15.2
27.0880	27.0756	HI	24-14	7.2±1.5	13.3±5.3
27.7921	27.7887	HeII (HI?)	18-16 (9-8)	30.7±3.3	54.6±7.1
28.2188	28.2137	H_2	(0,0) S(0)	5.2±2.3	8.9±3.5
28.8312	28.8309	HI	14-11	3.5±2.2	8.6±3.5
28.9717	28.9851	HI	19-13	5.3±2.9	13.5±5.0
33.4810	33.4729	[SIII]	3P1-3P0	109.9±6.3	146.5±5.4

Table 3.6: Line fluxes derived from the IRS/CH0 spectrum, after the background subtraction.

λ_{lab} (μm)	λ_{cent} (μm)	Element	Transition	$F_{observed}$ ($_{10^{-21}}$W cm^{-2})	$F_{dereddened}$ ($_{10^{-21}}$W cm^{-2})
7.3177	7.4543	[NaIII] (HeII?)	$2P\frac{1}{2}$-$2P\frac{3}{2}$ (12-10)	962±160	(2.5±1.4)×10^3
8.6645	8.6997	HI	14-8	123.8±40.1	963.8±402.0
10.6822	10.7981	[NiII]	4F7/2-4F9/2	30.2±20.8	not present
11.2429	11.2763	HI ([NiI]?)	23-10 (a3F2-a3F3)	87.6±24.9	452.4±151.0
12.2485	12.3650	HeII ([CoI]?)	25-17 (a4F7/2-a4F9/2)	118.9±29.6	485.7±23.3
12.8135	12.8070	[NeII]	$2P\frac{1}{2}$-$2P\frac{3}{2}$	82.9±10.7	135.3±105.8

Table 3.7: Line fluxes derived from the IRS/CH1 spectrum, after the background subtraction.

λ_{lab} (μm)	λ_{cent} (μm)	Element	Transition	$F_{observed}$ ($_{10^{-21}}$W cm^{-2})	$F_{dereddened}$ ($_{10^{-21}}$W cm^{-2})
10.4992	10.4995	HeII (HI?)	24-16 (12-8)	9.1±3.6	104.1±46.4
10.6822	10.6809	[NiII]	4F7/2-4F9/2	5.6±4.0	88.6±70.1
10.8543	10.8737	HI	25-10	18.3±6.5	131.2±82.1
11.3026	11.3025	HeII (HI?)	23-16 (18-14)	27.8±5.6	165.3±39.9
11.5395	11.5400	HI	15-9	6.3±5.1	34.2±17.3
12.1568	12.1608	HI	20-10	4.9±3.1	18.8±13.3
12.3669	12.3677	HeII (HI?)	14-12 (7-6)	65.4±14.0	275.5±17.7
12.7288	12.7222	[NiII]	(4F5/2-4F7/2)	6.0±2.0	16.8±9.9
12.8135	12.8086	[NeII]	2P1/2-2P3/2	9.9±1.5	40.0±13.0
13.9418	13.9284	HI	17-10	4.7±4.3	12.9±7.7
14.1831	14.1758	HI	13-9	7.6±3.2	17.6±6.6
14.9623	14.9470	HI	16-10	3.3±1.5	16.4±5.6
15.5551	15.5511	[NeIII]	3P1-3P2	11.6±3.4	17.9±3.2
16.2025	16.2009	HeII (HI?)	20-16 (10-8)	10.1±2.2	24.0±3.6
16.8737	16.8760	HeII (HI?)	24-18 (12-9)	4.3±1.1	13.2±3.7
17.6082	17.6030	HI	18-11	2.7±2.4	23.7±6.0
17.9359	17.9358	[FeII]	a4F7/2-a4F9/2	8.1±2.2	24.9±7.0
18.7130	18.7085	[SIII]	3P2-3P1	14.8±1.8	45.6±6.1
19.0541	19.0527	HeII (HI?)	23-18 (8-7)	15.5±3.6	46.9±10.1

single Gaussians, after having estimated the baseline, usually of the first-order but in some cases of the second or third-order. In the tables intensities with signal-to-noise ratio (S/N) larger than 3 are listed. The errors are due to uncertainties in the background fitting procedure and do not take into account the absolute calibration errors. The uncertainty of the extinction curve interpolation at each λ is unknown, however we assigned a standard deviation equal to the 10% of the line flux.

3.3.2 Detected lines and shock-versus-PDR diagnostics

The mid-IR spectra of G79.29+0.46 are rich in ionic and atomic fine-structure lines ([CII], [OI], [SiII], [FeII], [NiII]), similarly to other LBVs (e.g. HR Car, Umana et al. 2009). In our cLBV this was first pointed out by Wendker et al. (1998) and Jiménez-Esteban, Rizzo, & Palau (2010). However, after our background subtraction from the IRS spectra, we find some differences.

For instance, some emission-lines, previously attributed by Jiménez-Esteban, Rizzo, & Palau (2010) to the nebula of G79.29+0.46, disappear. In particular the [ArII] (or [NeII]) 6.97 μm, [FI] 24.75 μm and [SiII] 34.80 μm lines. At about 10.88 μm we found HI (25-10) instead of [NeIII]. We also found [NiII] emission at 12.72 μm and HI (13-10) at 22.31 μm in the nebula, not present in Jiménez-Esteban, Rizzo, & Palau (2010). [ArIII] 8.99 μm is absent, probably because faint and not detected. However, we confirm the presence of other high-ionization potential lines, i.e. [OIII], [NeIII], [SIII] and [FeIII].

Jiménez-Esteban, Rizzo, & Palau (2010) attributed emission-lines in the band of the Unidentified Infrared (UIR) features (centered at $3.3, 6.2, 7.7, 8.6, 11.3\,\mu$m) to Polyciclic Aromatic Hydrocarbons (PAHs). After subtracting the background emission, we find that these features in the IRS/CHO disappear. Therefore we believe that the emission in the PAHs bands observed by Jiménez-Esteban, Rizzo, & Palau (2010) is interstellar.

Conversely, according to Jiménez-Esteban, Rizzo, & Palau (2010), we confirm the absence of [SI] 25.2 μm which, together with [SiII] 34.8 μm, is a discriminant of shocks-versus-PDRs. We also attribute a foreground origin to the rotational absorption line of H_2 at 28.2 μm.

ISO/LWS spectra have strong [OI], [OIII], [NII] and [CII] line emissions. [NII] 122 μm line is indicative of high-ionization regions. Together with the [OIII] 88 μm, it is brighter inside the inner shell, along the east-west direction. However, the presence of both the transitions also in the outer shell indicates an extended nature of the ionized gas. We can not exclude that it is interstellar diffuse gas, because off-nebula observations are not available.

Looking at the [OI] 63.2 μm line fluxes detected with *ISO*/LWS, we can notice that

they are very similar in flux over the nebula. The [OI] emission is typical of shocked regions or of PDRs. This line is the main cooling transition in the dense post-shocked region of dissociative shocks (van Loon et al. 2010; Giannini, Nisini, & Lorenzetti 2001). When [OI] line is fainter than the [OIII] line, it indicates absence of strong interactions (van Loon et al. 2010). Otherwise [OI] line forms in PDRs, while [OIII] is typically strong in high-ionized diffuse gas (Mizutani, Onaka, & Shibai 2002). Therefore, the comparison in our LWS spectra between these two transitions seems to exclude the presence of shocked regions. Another indicator of shocked regions or PDRs is the line pair [OI] 63 μm/[CII] 157.7 μm (Tielens & Hollenbach 1985), being strong [CII] emission typical of PDRs. In particular, when the ratio is less then 10, then the presence of a PDR is favoured. From analysis of this ratio in our LWS we can exclude, therefore, the presence of shocked regions in the area covered by the observations. It is clearly evident that a PDR is present between the HII region, probed by free-free emission (see Chapter 2), and the molecular cloud, probed by rotational CO line emission (Rizzo, Jiménez-Esteban, & Ortiz 2008). However, since for these spectra we do not have background datasets, we can not exclude that this gas belongs to the diffuse interstellar medium.

[OIII] 51.8 μm is particularly brighter in the north-east part of the second shell, next to the radio "spur" emission, first detected by Higgs, Wendker, & Landecker (1994) and present also in our radio maps (see Fig. 2.1 in the previous chapter). Analysis of the radio spectral index in this region showed us a value (0.55) different from optically thin free-free emission. Excluding excitation by a shock, these higher [OIII] emission in the nebula outskirts may be attributed to density clumps.

3.3.3 Electron density from mid-IR line ratios

The mid-IR lines of [SIII] can be used for electron density diagnostics in a nebula. In fact, Houck et al. (1984); Moorwood et al. (1980); Mizutani, Onaka, & Shibai (2002) and then Smith et al. (2009) computed the [SIII] 18.7 μm/[SIII] 33.5 μm line ratio dependence on the electron density. They found that this ratio, temperature-independent, is sensitive to change on the electron density in the range $100 \leq n_e \leq 10^4\,\mathrm{cm}^{-3}$ (see Fig. 3.6). In particular, they found that "the ratio saturates at high densities, when collisions are rapid enough to populate the levels in equilibrium according to their statistical weights, and at low densities, when radiative effects dominate" (Smith et al. 2009).

Hence we have derived the [SIII] 18.7 μm and 33.5 μm line fluxes present in the *ISO* SWS spectrum with TDT number 76802901, positioned at approximately the nebula centre. The two transitions have measured and dereddened fluxes as in Table 3.3. Interstellar absorption is yet important at 18 μm and for this reason we consider the dereddened

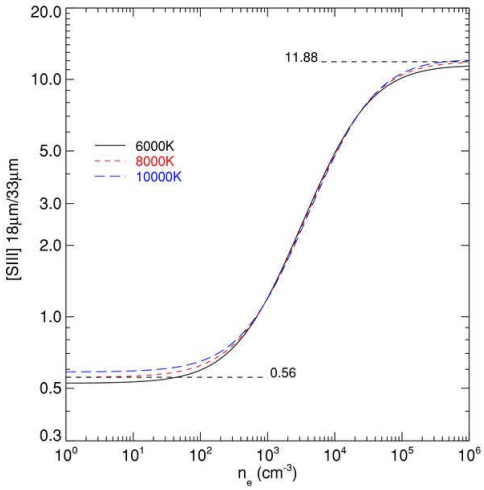

Figure 3.6: [SIII] 18.7 μm/[SIII] 33.5 μm density diagnostics for three representative temperatures (Smith et al. 2009).

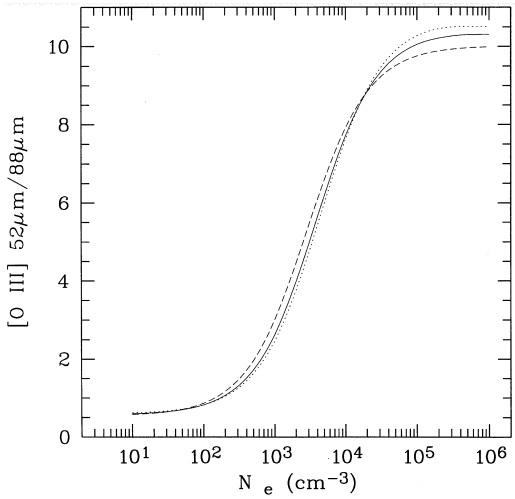

Figure 3.7: [OIII] 51.82 μm/[OIII] 88.36 μm density diagnostics for three representative temperatures (Liu et al. 2001).

values.

The derived line ratio is F(18.7 μm)/F(33.5 μm)= 0.74±0.47 which corresponds to an electron density of $\sim 250\,cm^{-3}$. The error in this ratio is due to the uncertainty in the measured lines and is derived using the error propagation for independent events.

Similarly, by using the same line pair present in the IRS spectra (in particular the line at 33.5 μm from the LH spectrum and the line at 18.7 μm from the SH one), we found a ratio of 1.45 which corresponds to a density of $\sim 10^3\,\mathrm{cm}^{-3}$. We took into account the difference in areas covered by the LH and SH modules, rescaling the flux at 33.5 μm by a factor of $(4.66)^{-1}$.

We notice that the electron density estimate from the IRS line pair is an order of magnitude higher than the values found from the SWS lines. This may be due to the larger area of the SWS slit in respect to the IRS modules: as a consequence the central value is averaged with smaller densities far from the centre. Our estimate is also bigger than those of Jiménez-Esteban, Rizzo, & Palau (2010), which found an electron density of $\sim 500\,\mathrm{cm}^{-3}$. The reason could be the fact that they did not correct for extinction, which is yet important at 18.7 μm.

The [OIII] 88.4 μm-51.8 μm line pair is a more sensitive indicator of the electron density, in respect to the [SIII] 33.5 μm-18.7 μm line pair (Houck et al. 1984). Using the LWS spectra we have determined [OIII] 88.4 μm-51.8 μm line ratios at six different positions on the nebula.

Derived line ratios and electron density estimates are listed in Table 3.8. Only in two cases the ratio is just below the low density limit (0.57, Mizutani, Onaka, & Shibai 2002),

Table 3.8: Line ratios and electron densities.

Slit	Area	Relative position[a]	Line pair	Line ratio	n_e (cm^{-3})
IRS-SH/LH	4.7"×11.3"	0	18.5 μm/33.4 μm	1.45	∼1000
SWS-901	33"×20"	0	18.5 μm/33.4 μm	0.74	∼250
LWS-003	84"×84"	0	51.8 μm/88.4 μm	0.73	150-160
LWS-008	84"×84"	100" W	51.8 μm/88.4 μm	0.55	<100
LWS-014	84"×84"	100" E	51.8 μm/88.4 μm	0.53	<100
LWS-011	84"×84"	200" W	51.8 μm/88.4 μm	0.67	∼100
LWS-005	84"×84"	200" E	51.8 μm/88.4 μm	1.24	>200
LWS-007	84"×84"	200" N-E	51.8 μm/88.4 μm	1.15	∼200

[a] In respect to the star position.

therefore we provide an upper limit for the electron density. The low electron density region coincides with the inner shell (the high-ionized gas, observed also in the radio domain).

We want to highlight the fact that electron densities estimated with this method are quite consistent with the mean values ($41-73\,cm^{-3}$) found from the radio map (which probe the inner shell). This reinforces the geometrical model which we assumed in Section 2.4.2.

We notice that at the position of the star electron density is higher $\sim 1000\,\mathrm{cm}^{-3}$ (from IRS line ratio) and decreases to $\sim 250\,\mathrm{cm}^{-3}$ till $\sim 100\,\mathrm{cm}^{-3}$ next to the inner and outer shell, except in the north-east part of the second shell, where it increases again till $\sim 200\,\mathrm{cm}^{-3}$. In fact in this region [OIII] results particularly bright, as discussed in the previous subsection. This strengthens the indication of high density ($n_e > 100\,\mathrm{cm}^{-3}$) clumps in the vicinity of G79.29+0.46.

Another pair of lines useful for a diagnostic study is the [SiII] 34.8 μm to [SIII] 33.5 μm, that indicates changes in the excitation due to distance from the star (Simpson et al. 2007), but for these lines our SWS dataset cover only the central position on nebula. However, the resulting ratio is ~ 0.21, which is lower than the diffuse interstellar gas value (~ 2.5) and instead is a typical value in HII region (Simpson et al. 2007; Jiménez-Esteban, Rizzo, & Palau 2010). However, we notice that [SiII] emission is absent in the background-subtracted spectrum from IRS, which very probably indicates that the SWS detection at 34.8 μm is interstellar.

3.4 *Herschel* images of G79.29+0.46

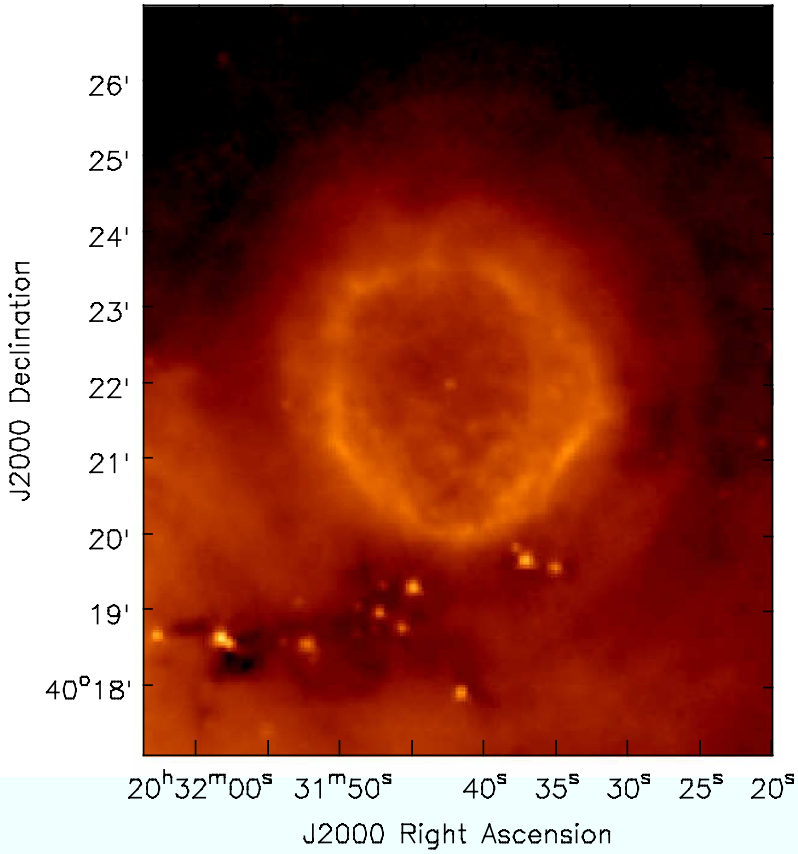

Figure 3.8: *Herschel*/PACS at 70 μm.

The 70 μm and 100 μm images obtained with the instrument PACS on board of the space telescope *Herschel* have a resolution (FWHM) between 5.5" and 6.7" comparable to those of the *Spitzer*/MIPS image at 24 μm, while at 160 μm comparable to those of the MIPS image at 70 μm. As a result, the 70 μm and 100 μm maps resemble the same features of the 24 μm image, probing the colder dust distributed in the inner (with peak at $\sim$ 100") and outer (at $\sim$ 200") shells. At longer wavelengths the nebula is less bright, but the outer shell appears to not suffer strong absorption from the IRDC.

At 160 μm there are hints of the second shell, but confusion is dominant and we can not resolve the outer shell from the background. This is however an indication that colder dust components should be absent in the circumstellar matter of our cLBV. For the photometric analysis, in this case we will concentrate only on the first shell.

At longer wavelengths (up to 160 μm) there are hints of arcs in the position of the first shell, but the IRDC becomes brighter and contaminate the shell emission. For this reason, in our analysis we will refer only to the 70 μm, 100 μm and 160 μm images. These are

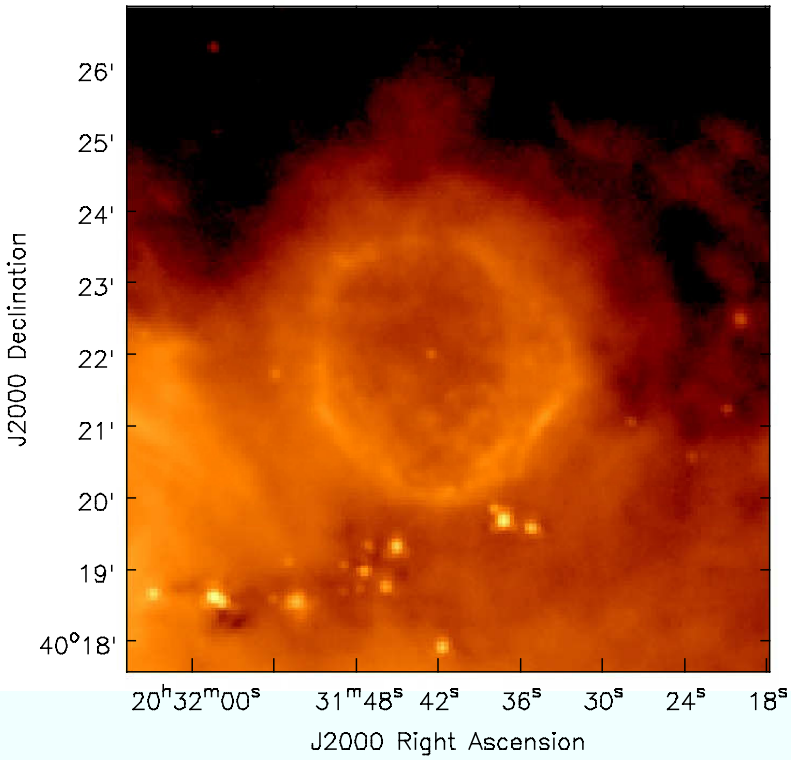

Figure 3.9: *Herschel*/PACS at 100 μm.

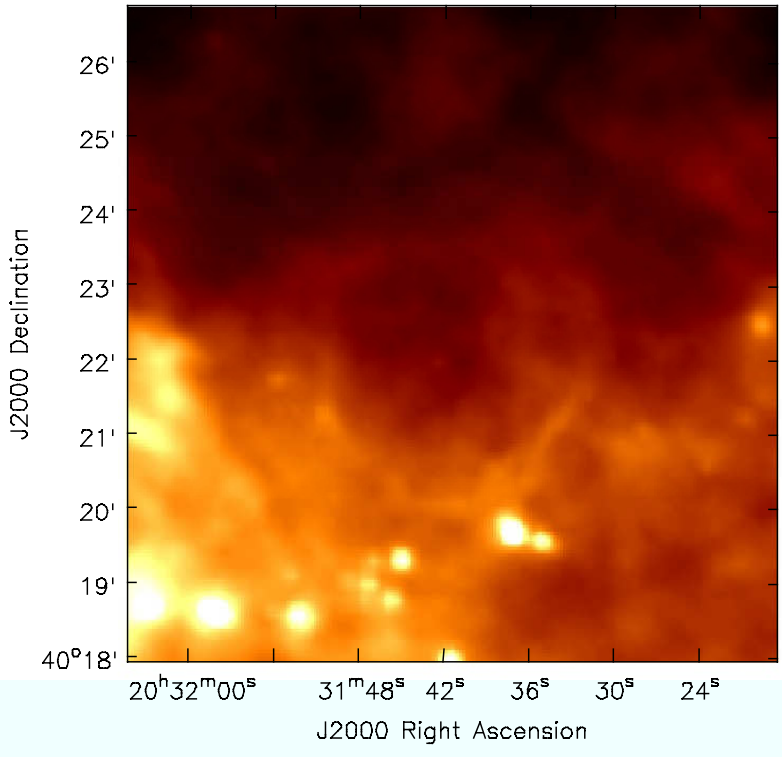

Figure 3.10: *Herschel*/PACS at 160 μm.

shown in Fig. 3.8, 3.9 and 3.10.

3.5 Analysis of the infrared images

In this section we estimate physical parameters related to the dust components in the nebula of our cLBV. As mentioned in the previous chapter, there is a strong evidence that there are at least two populations of dust: the warmer one emitting in the IRAC bands of *Spitzer*, and the colder one emitting in the MIPS bands of *Spitzer* and now also in the PACS bands of *Herschel*.

We have measured flux densities of the nebula around G79.29+0.46 from all the maps available in the data archives, using the package *Skyview*. We remind the reader that these maps are summarized in Table 3.2.

Thanks to the circular shape of the nebula, flux densities were evaluated in circles enclosing the emitting regions to the specific wavelength. In particular, the warm dust (traced at the IRAC wavelengths) is contained in a circle with radius approximately 1.9 arcmin, the emission in the *MSX* and ISOCAM bands in a circle with radius 1.96 arcmin. Up to 15 μm the emission is distributed in a region extended $\pm$2.2 arcmin and at the longest wavelengths (up to 25 μm) it is within a radius of 3.6 arcmin.

Since G79.29+0.46 is located in a region with a strong diffuse emission, it was necessary to evaluate the background, which was hence directly subtracted from the integrated flux densities. In particular, the background was measured in annuli close to the nebular emission and in the same way the standard deviation (*st dev*), which we used to estimate flux density errors. These are expressed as $st\,dev_{[\mathrm{Jy\,sr^{-1}}]} \times sr\,area$, where $sr\,area$ is the region in steradians where flux densities were integrated. Errors due to flux calibration uncertainty are not taken into account. Flux densities and errors at all the wavelengths are reported in Table 3.9 and plotted in Figure 3.12.

Flux density errors are very big (sometimes also up to the 50 per cent). This is due to the low-sensitivity of the old instruments (e.g. ISOCAM, ISOPHOT, SPIRITIII) and also to the diffuse emission in background, which becomes important in the far-IR.

3.5.1 Temperature and mass of the dust

Following a simple method described in Dayal et al. (1998) and in Umana et al. (2010), we estimated the dust temperature and mass for the two dusty shells.

In fact, assuming that the infrared emission observed is due to thermal dust and considering the radiative transfer equation in the case of an optically thin nebula, the brightness

Table 3.9: Photometric observations and flux densities.

λ (μm)	Flux density (Jy)	Flux density error* (Jy)	Instrument	#
8	4.61[a] †	3.1	IRAC	AOR17330688
8.28	8.1[b]	2.7	SPIRITIII	N/A
8.69	7.74[b]	3.81	ISOCAM01	35700630
11.48	11.94[b]	7.74	ISOCAM01	35700630
12.13	2.4⋆	2.1	SPIRITIII	N/A
12.41	8.9[b]	5.4	ISOCAM01	35700630
13.53	9.11[b]	5.26	ISOCAM01	35700630
14.65	14.7[b]	14.5	SPIRITIII	N/A
15.96	20.6[c]	10.5	ISOCAM01	35700630
21.3	90.6[d]	38.7	SPIRITIII	N/A
24	176[d]	49	MIPS	AOR22508544
25	191[e]	51	ISOPHT032	38101802
60	328[d]	252	ISOPHT032	35201501
70	670[d]	590	MIPS	AOR22508544
70	605[d]	454	PACS	N/A
100	500[f]	350	PACS	N/A
105	530[d]	500	ISOPHT032	35201501
160	13[c]	10	PACS	N/A

* Calibration errors are not taken into account
† This measures is probably overestimated because of saturation of the star
a Inside a circle with radius 1.9 arcmin
b Inside a circle with radius 1.96 arcmin
c Inside a circle with radius 2.2 arcmin
d Inside a circle with radius 3.6 arcmin
e Inside a circle with radius 2.9 arcmin (max FOV of the map in DEC)
f Inside a polygonal area about 2.7×10^{-6} sr
⋆ Inside a circle with radius 0.36 arcmin (only central object detected)

is

$$I_\nu \approx B_\nu(T)\tau_\nu \tag{3.2}$$

if the radiation is not absorbed by colder dust along the line of sight. The optical depth τ_ν of the nebula is proportional to the absorption coefficient κ_ν through the following relationship

$$\tau_\nu = \kappa_\nu \rho l \tag{3.3}$$

where ρl is the column density.

If κ_ν is known, then it is possible to derive the average dust temperature interpolating a Planckian distribution $B_\nu(T)$ between two observed brightnesses (or else two flux densities) at wavelengths falling in the same regime (Wien or Rayleight).

The absorption coefficient was computed by Umana et al. (2010) for two different chemical compositions (graphite and silicates) and three grain sizes ($a = 0.01, 0.1, 1\,\mu$m) and the results are illustrated in Fig. 3.11.

The mass of the nebula can be determined as

$$M = \rho l \Omega D^2 \tag{3.4}$$

where ρl is obtained inverting equation (3.3) and ΩD^2 is the area covered by the emitting region.

For the analysis of the warmer dust we consider the *Spitzer*/IRAC map at 8 μm, assuming that PAHs do not contribute to the emission at this wavelength (as revealed by the background-subtracted IRS spectra), and the ISOCAM map at 13.53 μm, which has the same sizes of the IRAC nebula and is the least noisy among the *ISO* maps. From the measured flux densities in Table 3.9 we subtracted the stellar component, because still bright at these wavelengths. We measured the stellar emission by fitting an aperture of about 0.25 arcmin around the central point. After this subtraction we estimated for the nebula the following flux densities: $F(8\,\mu\text{m}) = 5.43\,\text{Jy}$ and $F(13.53\,\mu\text{m}) = 8.11\,\text{Jy}$.

For the analysis of the colder dust component we refer to the *Spitzer*/MIPS 24 μm and the *Herschel*/PACS 70 μm maps, given their similarity. Also in this case we subtracted the stellar component by evaluating its flux density in a circle of 0.25 arcmin. Therefore, the nebula flux density are $F(24\,\mu\text{m}) = 174.15\,\text{Jy}$ and $F(70\,\mu\text{m}) = 603.74\,\text{Jy}$.

By using these flux densities, the solid angle subtended by the source (see Table 3.9) and the model described above, we found for both the warmer and colder dust components the temperature and mass listed in Table 3.10.

In the case of the warmer grains, with an average temperature of 456 K, the resulting mass is very small ($\sim 10^{-7}\,\text{M}_\odot$) and hence negligible. The colder dust has an average

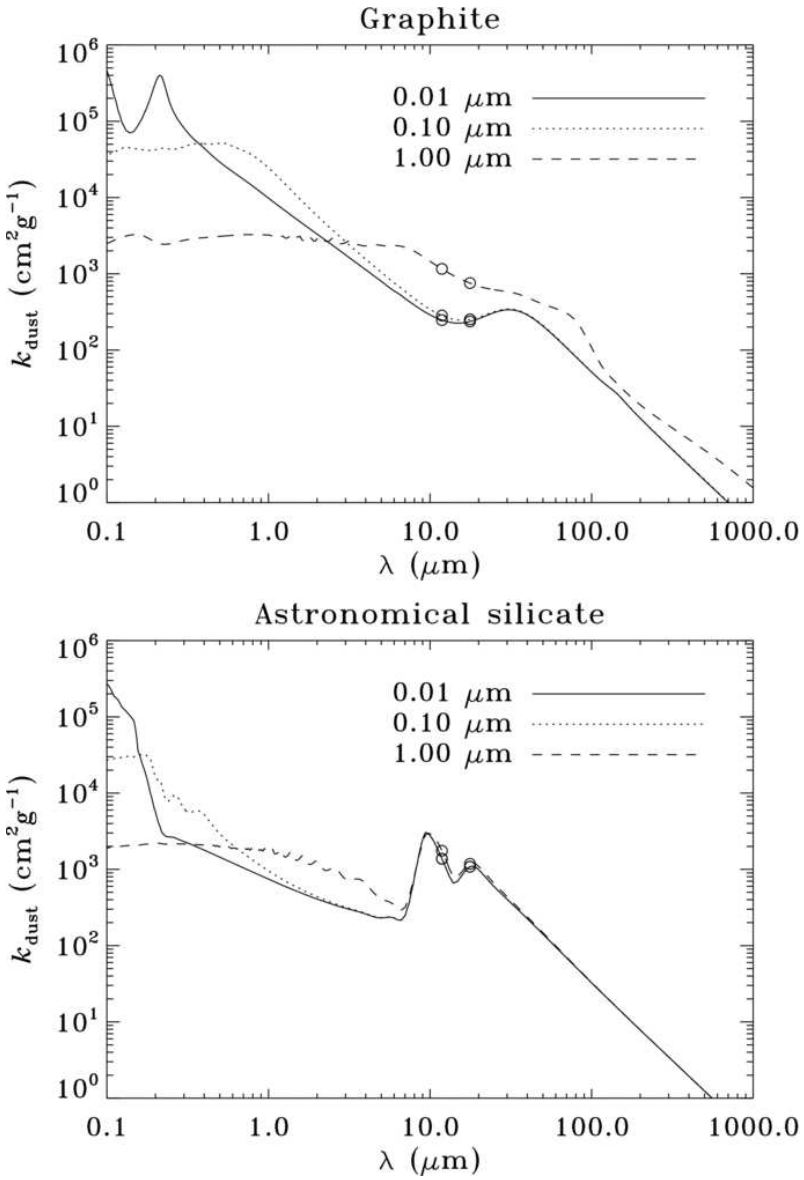

Figure 3.11: Absorption coefficients per mass unit for graphite (upper panel) and astronomical silicates (bottom panel), for different values of the dust grain size (Umana et al. 2010).

Table 3.10: Assumed chemical composition, grain size and absorption coefficient; derived optical depth, temperature and mass of the dust.

Composition and grain size	κ_{ν_1} ($cm^2\,g^{-1}$)	κ_{ν_2} ($cm^2\,g^{-1}$)	τ_{ν_1}	τ_{ν_2}	T (K)	M ($M_\odot$)
Warmer dust						
Silicate (0.01, 0.1, 1 μm)	1000	600	3.1×10^{-9}	4.3×10^{-9}	470	7×10^{-8}
Graphite (0.01, 0.1 μm)	400	250	2.8×10^{-9}	4.0×10^{-9}	485	1.6×10^{-7}
Graphite (1 μm)	2000	1000	5.4×10^{-9}	6.1×10^{-9}	412	6.2×10^{-8}
Colder dust						
Silicate (0.01, 0.1, 1 μm)	647.7	69	4.1×10^{-4}	4.4×10^{-5}	59	0.033
Graphite (0.01, 0.1 μm)	300	107	6.2×10^{-5}	2.2×10^{-5}	73	0.011
Graphite (1 μm)	600	300	3.6×10^{-5}	1.8×10^{-5}	78	0.0032

temperature of 70 K and results to be more massive ($1.6 \sim 10^{-2}\,M_\odot$). In all the cases the dust is optically thin (being $\tau_\nu \ll 1$).

If G79.29+0.46 is oxygen-rich, then it is natural to suppose that the grains are compound by silicates. In this case, we conclude that for the inner warm shell the grain temperature is 470 K and massive only $7 \sim 10^{-8}\,M_\odot$, while for the inner and outer cold shells the average temperature is 59 K. The total budget of the dust mass is $3.3 \sim 10^{-2}\,M_\odot$.

If G79.29.0.46 is carbon-rich the small grains temperature is 485 K in the warm inner shell and at most 78 K in the colder shells, resulting in a total mass of not more than $1.1 \sim 10^{-2}\,M_\odot$.

Modelling the 24 μm and 70 μm emission from the *Spitzer*/MIPS images, Kraemer et al. (2010) found slightly higher temperatures ($87 - 108$ K), in the hypothesis of carbon-rich nebula with amorphous grains and PAHs.

Analysing IRAS images Waters et al. (1996) provided a lower limit for the inner shell temperature of about 65 K and dust mass of $0.14\,M_\odot$. They obtained these values through a "best-fit" model of the IR emission.

3.5.2 Total mass and gas-to-dust ratio

With a dust mass of $3.3 \sim 10^{-2}\,M_\odot$, which includes the warm dust mass (however negligible) and the cold dust mass in case of silicates, and the ionized mass of $3.5\,M_\odot$ (see Section 2.4.2), we derive a total mass of $\sim 3.533\,M_\odot$ for the nebula around G79.29+0.46.

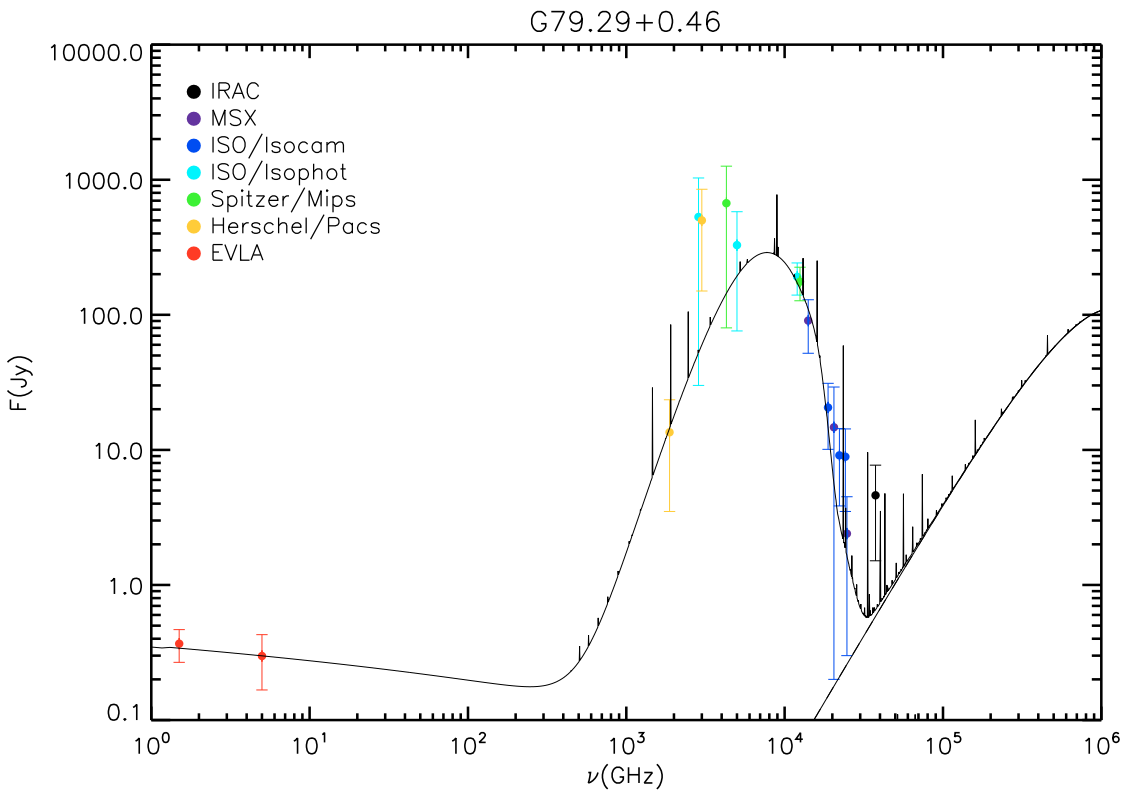

Figure 3.12: Model of the SED and observed Flux Densities of G79.29+0.46 from *Spitzer*, *ISO*, *MSX*, *Herschel* and ELVA observations.

With these values the gas-to-dust ratio is ~ 106, which is consistent with the galactic interstellar case. Assuming a gas-to-dust ratio of 100 and their estimate of the dust mass, Waters et al. (1996) found a total mass of $14\,M_{\odot}$. This value is an order of magnitude larger than our estimate. These discrepancies may be due to the difference in the assumed distances ($D = 2\,$kpc, Waters et al. 1996) or to effects of bad resolution in the IRAS images. In the first case, assuming $D = 2\,$kpc we found a total mass of about 1.4 times bigger than our first estimate. The second possibility, more likely, is that the IRAS low-resolution images caused an overestimation of the shell radius and hence of the area covered by the nebula.

3.6 Spectral Energy Distribution

Using the physical parameters derived in our analysis of the radio and infrared nebulae, we have fitted the SED with the photo-ionization code CLOUDY version c10.00, described by Ferland et al. (1998). In particular, we have imposed for the star a blackbody temperature of 20400 K (consistent with a spectral type B1-B0.5, as derived in Section 2.4.3) and assumed a luminosity $\log L/L_{\odot} = 5.9$. For the nebula we chose a spherical ge-

ometry with inner radius of 100" and external radius 200" (corresponding to the position of the radio and infrared emission peaks) and used a mass of 3.53 $M_{\odot}$ as stopping criterion. The density assumed in this model is constant ($\sim 200\,cm^{-3}$) in the shell and then decreases with a law $\propto r^{-2}$. We included grains of silicates with $a = 1$ μm and graphite with $a = 0.01$ μm. The distance considered is 1.7 kpc. The model is plotted in Fig. 3.12 and the measured fluxes are hence overlaid.

As a result of the model, the temperature of the silicate grains is 82 K closest to the star and 59 K at the edge of the nebula, while for graphite grains it is respectively 96 K and 63 K. These values are quite similar to our estimates from the far-IR images (see Table 3.10), but slightly higher. This could be due to an underestimation of the infrared fluxes, due to possible absorption by the molecular cloud revealed by Jiménez-Esteban, Rizzo, & Palau (2010). Another explanation could be the uncertainty of the distance: in fact if G79.29+0.46 is closer than assumed, then the star will be colder, as well as the nebula. Moreover, our model does not include two distinct infrared shells, but only a nebula extending between 100" and 200". In this model it is assumed that the ionization front reaches the furthest edge of the nebula, heating the dust, whereas actually it stops before half of the second shell.

However, our assumed effective temperature and the determined bolometric luminosity are consistent with Waters et al. (1996) which found similar values for the dust temperature, by assuming the same stellar parameters and by fitting the IRAS infrared images.

3.7 Discussion/Conclusions

Our spectroscopic and photometric analysis in the IR allowed us to identify new findings concerning the nebula associated with the cLBV G79.29+0.49. In particular, analysis of the mid-IR IRS spectra after the background subtraction revealed us that PAHs features attributed to the nebula by Jiménez-Esteban, Rizzo, & Palau (2010) are actually interstellar. The electron density diagnostics at different radii from the star showed that values ($\sim 100\,cm^{-3}$) found from line-pairs analysis are consistent with those ($\sim 73\,cm^{-3}$) estimated in the previous chapter from the radio, concerning the region including the ionized shell. This reinforce the geometry assumed previously (a toroidal-shell with geometrical depth 0.29 pc) and, as a consequence, gives meaning to the estimated ionized mass. Conversely, electron densities estimated from the line-pairs next to the north-east nebula edge are higher ($\sim 200\,cm^{-3}$). This higher density region corresponds to the radio "spur-emission" (observed for first time by Higgs, Wendker, & Landecker 1994). Our spectral

index analysis of this region (see previous chapter), together with the density found here, gives evidence of the presence of density clumps.

We also presented a shock-versus-PDR diagnostic study. Concerning the area covered by the slits, there is no evidence of shock regions over the nebula (the south-west region near the IRDC was not observed). Conversely, it appears evident that physical conditions and chemical composition similar to PDRs are present in the surroundings of the inner shell.

Our photometric analysis provided us with estimates of the temperature and the mass of both the warm and cold dust components in the nebula. In particular, the dust mass, compared with the ionized mass, is consistent with the galactic gas-to-dust ratio.

Finally, adopting as input parameters the values found in this work, we modelled the star and the nebula emission of G79.29+0.46 with CLOUDY. As a result, we found that the star must have a luminosity $\log(L/L_{\odot})$ equal to 5.9.

Acknowledgments

This research made use of data products from the Midcourse Space Experiment. Processing of the data was funded by the Ballistic Missile Defense Organization with additional support from NASA Office of Space Science. This research has also made use of the NASA/IPAC Infrared Science Archive, which is operated by the Jet Propulsion Laboratory, California Institute of Technology, under contract with the National Aeronautics and Space Administration. Support for this work was provided by NASA through an award issued by JPL/Caltech, which allowed the author of this thesis to work with the IPAC team for four months.

This work is also based on observations with *ISO*, an ESA project with instruments funded by ESA Member States (especially the PI countries: France, Germany, the Netherlands and the United Kingdom) and with the participation of ISAS and NASA.

Herschel is an ESA mission with participation from NASA.

Part II

LBVs in the Large Magellanic Cloud

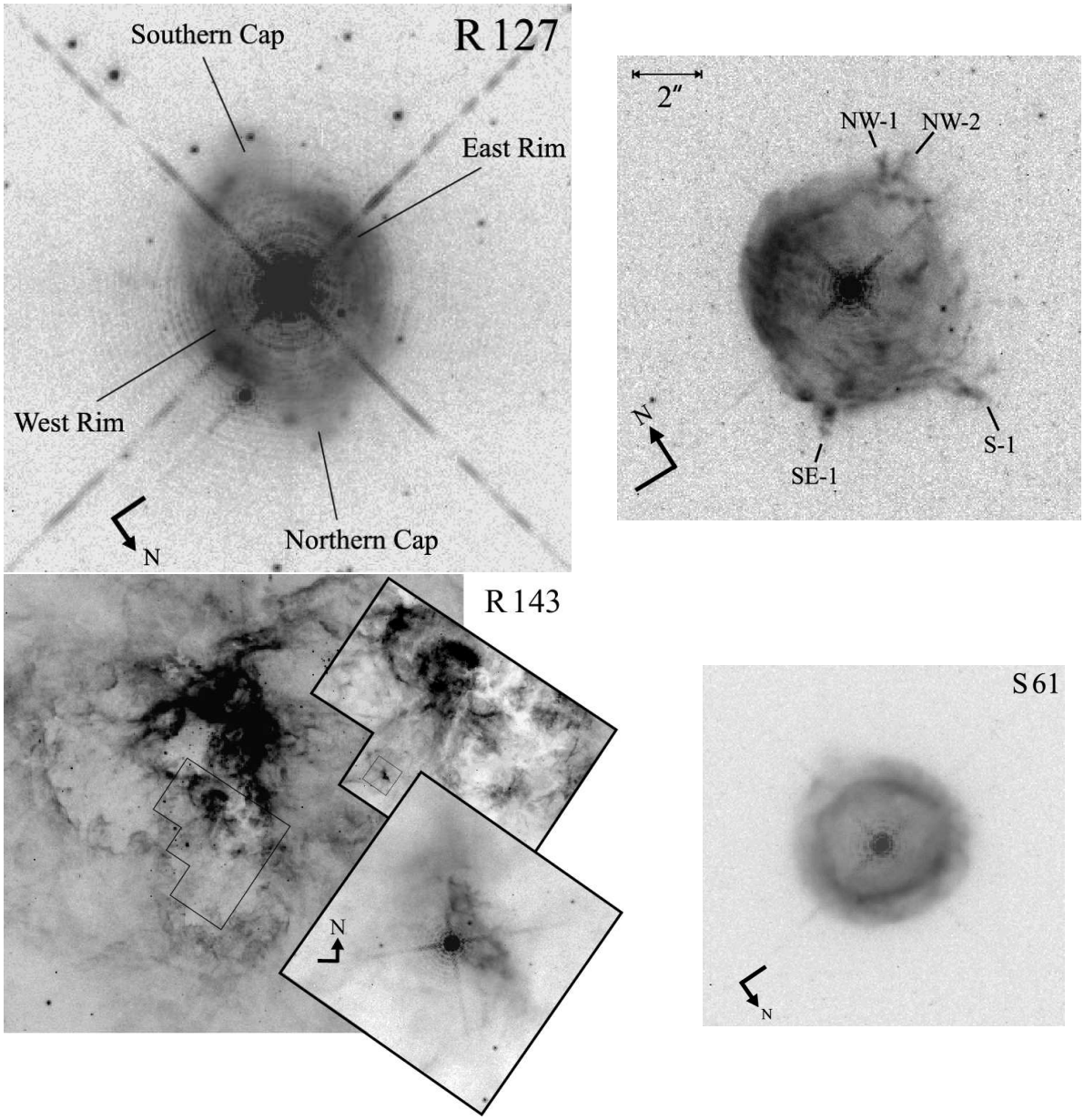

Figure 3.13: Hα *HST* images from the work by Weis (2003) and Weis, Duschl, & Bomans (2003).

Humphreys & Davidson (1994) and later Smith & Owocki (2006) have suggested that the LBV extreme mass-loss occurs via eruptive episodes, driven by metallicity independent mechanisms rather than the usually adopted line-driven stellar wind. If this is the case, LBV stars may have had a paramount importance in the evolution of the early Universe, when massive stars would have been more numerous than in the present epoch, and may have provided, through their ejecta, processed material and dust for future generations of stars.

LBVs have also been considered as possible *dust producers* in high-redshift galaxies (Gall, Hjorth, & Andersen 2011), where the significant amount of dust observed in the sub-mm remains as yet an unanswered question.

A way to explore these possibilities is to study the LBV phenomenon in environments different from the galactic one, i.e. in galaxies with different metallicity. Considering the capabilities of the instruments up to now available, we have started a study at radio wavelengths of LBVNe in the LMC, which is the nearest galaxy (with an accepted distance of $D \sim 48.5\,\mathrm{kpc}$) and with half the solar metallicity ($Z \sim 0.5\,\mathrm{Z}_{\odot}$).

A census of LBVs in the LMC reported 25 confirmed LBVs and candidates (van Genderen 2001; Clark, Larionov, & Arkharov 2005). We have hence searched the literature and the data-archives for evidence of extended nebulae around LBVs and cLBVs and found that most of these objects have a classification based only on ultraviolet, optical and near-IR photometry and spectroscopy (e.g. Stahl 1990; Nota et al. 1991), probing mostly the stellar component. However, evidence of extended nebulae around LBVs in the LMC was reported by Weis (2003) and Weis, Duschl, & Bomans (2003), which performed high-resolution observations of 9 LBVs and cLBVs in the LMC with the Hα filter using the *Wide Field Planetary Camera 2* (WFPC2) on board of the *HST* and with the ESO Multi-Mode Instrument (EMMI). In particular, they found that 5 of these objects show a very well-defined shell in Hα, with sizes in the range $5" - 18"$, indicating the presence of a nebula around them.

Based on these studies we have selected a group of LVBNe that could be detected at radio wavelengths (which allow us to probe the properties of the ionized gas) through the estimation of the radio free-free emission from the observed hydrogen Hα recombination-line. Hence, we observed these LBVNe (namely: cLBVs S61 and S119, plus LBVs R127 and R143) with the ATCA (P.I. Agliozzo C.) at 5.5 and 9 GHz. These observations have allowed us to detect, for the first time, all the 4 LBVs in the radio and provided us with radio maps of their associated nebulae (Chapter 4).

Further observations were performed at ATCA (P.I. Agliozzo C.) at 17 and 23 GHz, in order to achieve higher-resolution images, in order to better understand the radio morphology, to gather spectral information and to determine the current-day mass-loss rate. This time we rejected one of these nebulae (i.e. S119) because it was too faint to be detectable at ATCA at the proposed frequencies. These new observations and related results are presented in Chapter 5.

Chapter 4

Radio detection of nebulae around four LBV stars in the LMC

Abstract

The nebulae associated with four LBVs in the LMC have been observed at 5.5 and 9 GHz using the Australia Telescope Compact Array, and radio emission has been detected for first time in these sources, R127, R143, S61 and S119. The radio maps of the nebulae have an angular resolution of ~ 1.5" and a sensitivity of 1.5-3.0$\times 10^{-2}$ mJy beam^{-1}, and show a very similar morphology to that observed in Hα. This similarity permit us to assume that the Hα emission is not affected by strong intrinsic extinction due to dust within the nebulae. We estimate the masses of the ionized gas in the LBVs nebulae and their values are consistent with those measured in galactic LBVs.

This work has been published in MNRAS (Agliozzo et al. 2012).

4.1 Introduction

In this section we give a description of the most interesting aspects concerning the two LBVs R127 and R143 and the two cLBVs S61 and S119.

Before the observations in the optical, the only study performed on these objects concerned mostly the stellar component, for which a classification based on ultraviolet, optical and near-IR photometry and spectroscopy was provided (e.g. Stahl 1990; Nota et al. 1991).

R127 is located in a compact subgroup of a small, evolved cluster (NGC 2055) containing several mid-O through early-B supergiants and that is devoid of nebulosity, south of 30 Doradus and not far from SN 1987A (Walborn et al. 2008). It was classified as LBV star when it was observed to experience S-Dor type variability (Stahl et al. 1983).

R127 is an important LBV, because in the past decades it experienced different outbursts and it was studied repeatedly between the quiescent and the active states, through spectroscopic and photometric observations (e.g. Walborn 1977, 1982; Stahl et al. 1983; Wolf et al. 1988). A recent study of interest from Walborn et al. (2008) shows the spectroscopic and photometric variations over the last 30 years.

R143 is the only LBV in the cluster of 30 Doradus (Parker et al. 1993). First observations of the star have been published by Feast, Thackeray, & Wesselink (1960), which classified it as a type F7 supergiant. In 1993 Parker et al. analysed UV spectra of the star and determined a spectral type B8-9. In the assumption that the bolometric magnitude was constant ($M_{bol} = -10$ mag), they concluded that the star moved in the H-R diagram over 40 years. Comparing the luminosity and the spectral type with evolutionary tracks of massive stars, they estimated an initial mass for R143 of $\sim 60\,M_{\odot}$.

S61 and S119 are only cLBVs because, since their first observations (Walborn 1977), they have not shown any spectroscopic and photometric variability, while R127 and R143 were observed in both the quiescent and active states. For a comparison, we suggest to check their positions and evolutionary tracks in the H-R diagram (Fig. 1.4).

S61 was classified as a luminous supergiant (Ia) spectral type O8 fpe[1] star by Walborn (1977). They found emission profiles very similar to R127 and absorption lines of SiIV and NIII, indicating the presence of extensive envelopes close to the star.

Walborn (1977) also identified S119 as a Ofpe/WN9[2] supergiant. Originally R127 also belonged to this class and later entered a state of outburst (between 1978-1980, Walborn 1982). The Of features disappeared and the spectrum evolved through an intermediate B-type stage to a peculiar supergiant A-type. In the meantime Of-type emission was discovered during a light minimum of the galactic LBV AG Car (Stahl 1986). Therefore, it has been believed and then accepted that Ofpe stars and LBVs are physically related (e.g., Stahl 1986; Bohannan & Walborn 1989; Smith et al. 1998). In fact, not only the Ofpe spectra seems to resemble the LBV spectra in quiescent states, but also their associated nebulae presented expansion velocities close to that of known LBVNe (e.g. HD 269582 and AG Car, Stahl 1986). Ofpe stars were hence renamed cLBVs.

R127, R143, S61, S119 have shown an associated nebula of gas, observed in the Hα recombination-line emission.

First high-resolution observations of R127 were obtained by Clampin et al. (1993),

[1] In the spectral type notation, "e" indicates the presence of line emissions, "p" means peculiar features, and "f" NIII and HeII line transitions.

[2] WN notation indicates WR type spectra, dominated by He and N emission-lines. Ofpe/WN stars combine in their spectra the Of characteristic with extensive lower-ionization emission features (Bohannan & Walborn 1989).

Table 4.1: ATCA observational summary.

Observation Date	ATCA Config.	Band (cm)	Total integration time (min)			
			S61	R127	R143	S119
11 Apr 18	6-km	3+6	534	534	58	59
11 Apr 21	6-km	3+6	58	59	533	536

which reported the presence of a diamond-shaped nebula around the star. Nota et al. (1994) proposed S119 as a LBV candidate, after the discovery of a nebula around the star (Bohannan & Walborn 1989). The nebula appeared as a shell with a brighter lobe in the north-east direction (Nota et al. 1994). The nebula associated with S61 was first resolved by Pasquali, Nota, & Clampin (1999) and showed a ring-like structure. Finally, the nebula around R143 revealed an unusual shape, triangular, elongated in the north-south direction (Smith et al. 1998).

Recently, Weis (2003) and Weis, Duschl, & Bomans (2003) presented new high-resolution images of such nebulae obtained with the *HST* in the Hα light (Fig. 3.13). These new images, which we reprocessed, constituted the starting point for our radio observations, described in Section 4.2. We compare the radio free-free continuum emission with that of Hα from the morphological and photometric points of view (Sections 4.3 and 4.4). In Section 4.4 we also estimate some physical parameters related to the nebulae and in Section 4.5 we present our final remarks.

4.2 Observations and data reduction

4.2.1 ATCA observations

Radio continuum observations were carried out on April 18 and 20, 2011, at the Australia Telescope Compact Array (ATCA), using the interferometer in the 6km-configuration. Data were acquired with the new back-end system Compact Array Broadband Back-end (CABB), with a maximum bandwidth of 2-GHz in the 3+6 cm band. The observations consisted of 15-min scans on the target, preceded and followed by 2-min scans on the phase calibrator (0530-727), for a total of $\sim$10 h on-source integration time. In order to achieve the best *uv*-coverage, the scans were distributed over 12 values of hour angles. We used 1934-638 for the bandpass and flux calibration. Table 4.1 summarizes the observations.

Datasets were separately edited and reduced by using the MIRIAD software package

(Sault, Teuben, & Wright 1995). After applying the bandpass and time-based gain corrections, the calibrated visibilities were imported into the CASA package (version 3.0.2) and processed for imaging, using the task `CLEAN` and performing a natural weighting to achieve the highest-sensitivity. Dirty images were deconvolved using the Clark algorithm (Clark 1980). The resulting synthetic beam Θ_{syn} is typically 2.5" $\times$ 2.0" at 5.5 GHz and 1.5" $\times$ 1.2" at 9 GHz. For imaging R143, which is located in a very crowded region, we applied a Briggs-type weighting (parameter `robust = 0`) to minimize sidelobe contribution of the brightest sources. This choice represents a good compromise between the highest-resolution and sensitivity achievable at ATCA.

The mean noise obtained on the maps is typically 1.5-2.0$\times 10^{-2}$ mJy beam^{-1}, consistent with the sensitivity of the new broadband back-end system CABB at these frequencies for the integration time used.

4.2.2 *Hubble Space Telescope* data

In order to compare the radio morphology of the nebula with that observed at other wavelengths, Hα images have been retrieved from the STScI data archive. These images have been obtained[3] with the WFPC2 instrument, using the Hα-equivalent filter F656N, and reduced by the standard *HST* pipeline. These data had already been published by Weis (2003) and Weis, Duschl, & Bomans (2003). For each source we combined the data-sets (four images with a 500-s exposure) following a standard procedure in IRAF to remove cosmic-ray artefacts and to improve the S/N.

Finally, we have also recalibrated the *HST* images astrometrically using the Naval Observatory Merged Astrometric Dataset (NOMAD) catalogue (Zacharias et al. 2005), for a corrected overlay with the radio images.

[3]Proposal ID: 6540; P.I. Regina Schulte- Ladbeck.

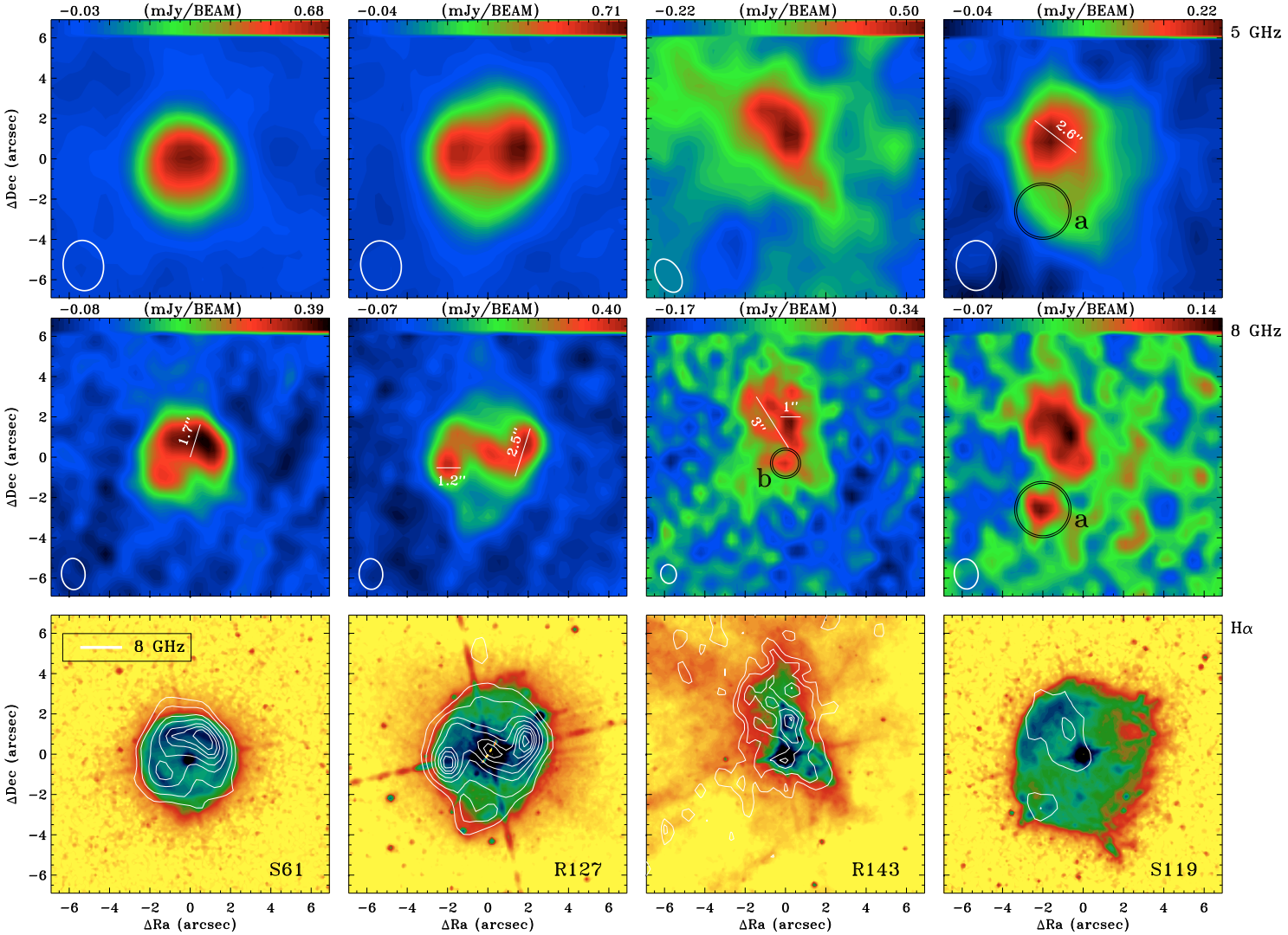

Figure 4.1: Top panels: 5 GHz ATCA maps of S61, R127, R143 and S119 from the left to the right. Middle: 8 GHz ATCA maps in the same order as before. Bottom: Hα WFPC2/*HST* images overlaid with 8 GHz ATCA contours. Contours are chosen at (3, 5, 8, 10, 12, 13, 14, 15)σ. In the radio maps the white ellipses represent the synthetic beam.

Table 4.2: Observed flux densities at 5.5 and 9 GHz, angular sizes at 9 GHz.

Source	S_{obs}(5.5 GHz) (mJy)	S_{obs}(9 GHz) (mJy)	Angular sizes
S61	2.1 ± 0.1	2.2 ± 0.3	5.1"×5.7"
R127	3.1 ± 0.2	3.3 ± 0.4	6.6"×7.5"
R143	2.4 ± 0.9	4.0 ± 0.7	3.7"×3.2"
S119	1.0 ± 0.2	0.9 ± 0.2	8.0"×9.6"[a]

[a] From the map at 5.5 GHz.

4.3 Morphology of the radio nebulae

In this section we give a morphological description of the radio emission compared to the optical (already provided by Weis 2003; Weis, Duschl, & Bomans 2003), obviously limited by the lower-resolution of the radio maps. Fig. 4.1 shows all the maps obtained in this work, compared with the reprocessed *HST* images.

The angular sizes of the emission region were estimated by drawing a box above 3σ on the sources. The maximum and minimum sizes are hence reported in Table 4.2. The estimated values are consistent with the precedent measurements (e.g. Clampin et al. 1993; Smith et al. 1998; Pasquali, Nota, & Clampin 1999; Weis, Duschl, & Bomans 2003; Weis 2003).

S61 presents in the optical a nebula consisting of an inner brighter ring-like structure and larger diffuse emission (Weis 2003). The radio nebula here resembles the Hα one, being roughly spherical (Fig. 4.1). The nebula is fainter in the south-west and the emission is not homogeneous: the brightest part is in the north-east, where the gas might be thicker. Greater diffuse emission all around is evident above 3σ, as well as the outer shell seen in Hα.

R127 High-resolution *HST* image in Weis (2003) revealed a nearly spherical structure in the central region and fainter emission in the northern and southern directions. The shell also presents two brighter rims on the east and the north-west sides.

The radio nebula show two components: a thin, roughly spherical nebula, elongated in the north-south direction, a thicker bipolar nebula, Z-pattern-shaped and centred in the optical stellar position. A hint of the central object is visible in the radio image.

R143 As pointed out by Weis (2003), the optical nebula is concentrated to the west of the star, without a counterpart nebular emission to the east. Four curved filaments close to R143 were noticed by Feast (1961) and then attributed to the nearby HII region by Smith et al. (1998).

The morphology in the radio map is quite similar to the optical one. The overlay with the optical image (Fig. 4.1, bottom panel) shows that the nebula might be contaminated by the near 30 Dor HII region emission, as is the optical one.

Unresolved compact emission at the position of the star is also visible in the map at 9 GHz.

S119 In the *HST* high-resolution images Weis, Duschl, & Bomans (2003) detected small-scale structures, such as filaments and knots, which give the nebula a patchy appearance.

The marked asymmetry of the nebula was explained (Danforth & Chu 2001) as due to a bow-shock interaction with the ISM, since the S119 radial velocity (blue-shifted $\sim$100 $\mathrm{km\,s^{-1}}$ from the LMC systemic velocity, Nota et al. 1994) suggests a runaway nature for the star.

The diffuse emission visible at 6 cm above 3σ (green/blue levels in Fig. 4.1, top panel) is not detected at ATCA 3 cm, but the thicker north-east and south-east parts are well detected and resemble the Hα morphology. In particular the south-east compact region (circle "a" in the figure) is not visible at the lower frequency. This might be due to the presence of an optically thick HII region. We can speculate that this is the result of an interaction between the stellar ejecta and the close ISM.

4.4 Data Analysis

4.4.1 Intrinsic extinction and spectral index

Under typical conditions of the ISM, the optical emission can be affected by extinction due to dust, while radio emission is not. We can establish whether the optical emission of ionized nebulae is affected by intrinsic extinction, following one of the methods for measuring extinction described by Pottasch (1984). This consists of a comparison between the recombination hydrogen line and the radio continuum emission coefficients (which have the same dependence on the nebular density), through the following relation

$$S_\nu = 2.51 \times 10^7 T_e^{0.53} \nu^{-0.1} Y F(\mathrm{H}\beta)_{\mathrm{exp}}\,[\mathrm{Jy}] \tag{4.1}$$

Table 4.3: Electron density, electron temperature, effective temperature available in the literature.

Source	n_e (cm^{-3})	T_e (K)	T_{eff} (K)
S61	400[a]	6120[a]	27600[c]
R127	720[b]	6420± 300[b]	16000[d]
R143	1000[b]	12200± 1500[b]	9700[e]
S119	680[b]	<6800[b]	26200[c]

a Pasquali et al. 1999
b Smith et al. 1998
c Crowther & Smith 1997
d Stahl et al. 1983
e Davies et al. 2005

Table 4.4: Hα line integrated flux, expected free-free flux density at 5.5 and at 9 GHz.

Source	F(Hα) (10^{-14} erg cm^{-2} s^{-1})	S_{exp}(5.5 GHz) (mJy)	S_{exp}(9 GHz) (mJy)
S61	10.6±0.7	1.7±0.1	1.6 ±0.1
R127	20.0±1.7	3.3±0.3	3.2±0.3
R143	3.6±2.1	0.84±0.50	0.80±0.48
S119	6.7±0.7	1.14 ±0.11	1.09±0.11

where T_e is the electron temperature of the nebula in unit of K, ν is the radio frequency in GHz, Y is a factor incorporating the ionized He/H ratios

$$Y = 1 + \frac{n(He^+)}{n(H^+)} + 4\frac{n(He^{++})}{n(H^+)}\frac{ln(4.95\times10^{-2}T_e^{\frac{3}{2}}\nu^{-1})}{ln(9.9\times10^{-2}T_e^{\frac{3}{2}}\nu^{-1})} \tag{4.2}$$

and $F(\mathrm{H}\beta)_{\mathrm{exp}}$ is the expected Hβ flux when the nebula is not affected by intrinsic extinction. For a nebula with electron density less than $10^4 cm^{-3}$ and electron temperature $\sim 10^4$K, $F(\mathrm{H}\beta)_{\mathrm{exp}} = \frac{\mathrm{F(H}\alpha)_{\mathrm{exp}}}{2.85}$ (see Table III-1 in Pottasch 1984). To evaluate the second term in equation (4.2), we consider that in a low-ionization nebula (see T_{eff} in Table 4.3), where the ionization is due mainly to the radiation field of the star, and with small $\frac{n(He)}{n(H)}$ ratios (typically 0.1-0.2 in the nebula, e.g. Lamers et al. 2001), the contribution from $n(He^+)$ to the free-free emission is negligible and consequently also the contribution from $n(He^{++})$.

Hence from the *HST* images we have measured the flux emitted in the Hα. We have

extracted aperture photometry fitting a circle around the star and another around the nebula. For R143, which does not have a rounded shape, we used a polygonal line to select the region in which to measure the flux density. Since we are interested in the recombination-line emission of the ionized nebulae, we have substituted the stellar contribution with the mean brightness around the star. In the case of R127 we have also subtracted the contribution from the external star projected on the nebula. Fluxes in the Hα are reported in Table 4.4.

We have measured the radio flux densities integrating over the entire nebula, by using an interactive tool of CASA. The rms-noise σ has been evaluated far from the targets. Flux densities were therefore compared with the sum of the clean components inside the regions. Since both measures are consistent with each other, we report the values measured with the interactive mode in Table 4.2. Flux density errors are defined as

$$\varepsilon = \sigma\sqrt{N} \tag{4.3}$$

where N is the number of independent beams in the selected region (Brogan et al. 2006). The error due to calibration uncertainty[4] is not taken into account.

Finally, with Y=1 and using as T_e the values found in the literature (Table 4.3), from the measured Hα we have estimated the radio fluxes at the observed frequencies (Table 4) and compared to the observed ones (Table 4.2).

The angular resolution obtained is not sufficient to isolate the stellar objects. Evidence of stellar wind comes from the positive value of the spectral indeces α (Table 4.5), which indicate a contribution to the nebular free-free optically thin emission that is more important at higher frequencies. Despite this, the values that we found indicate that the Hα emission probably does not suffer from strong intrinsic extinction. This is apparently true for both R127 and S119, which have flux densities equal to the expected ones within the errors. Moreover, for R127 we have evidence of a stellar wind contribution at 9 GHz. In the case of S119 we can not assess it because of the sensitivity limit at 9 GHz.

A similar discussion on the central object contribution can be applied to S61 and R143, even if in the last case the spectral index evidently shows that the nebula flux is contaminated by other emission sources (i.e. 30 Dor HII region). Moreover we can not exclude the presence of dust in the vicinity, which may cause optical extinction.

The S61 flux density at both 5.5 and 9 GHz are higher than the values expected from the recombination-line flux estimation. This could be due to an important stellar wind contribution even at the lowest frequencies or to a non-negligible dusty nebular component.

[4] $<$10% for 1934-638.

Table 4.5: Spectral index, emission measure, linear size, geometrical depth, source solid angle, average electron density, ionized mass.

Source	α_{obs}	$< EM >$ [pc cm^{-6}]	Linear size (pc×pc)	s (pc)	Ω_s (arcsec)^2	$< n_e >$ (cm^{-3})	$M_{ionized}$ ($M_\odot$)
S61	0.1	1364	1.2×1.3	0.40	24.5	58	0.78
R127	0.1	1345	1.6×1.8	0.28-0.59	38.1	69-48	1.01-1.46
R143	1.0	1697	0.9×0.8	0.24-0.71	19	85-49	0.52-0.90
S119	-0.2 [a]	222	1.9×2.3	0.61	71	19	1.13

[a] This value must be considered a lower limit.

4.4.2 Mass of the ionized nebula

From the radio free-free emission measurement we can estimate the total ionized mass as the total amount of particles present in the nebula. For a not self-absorbed free-free emission, the electron density in a nebula can be determined through the relation between the emission measure (Equ. 2.11) and the optical depth τ_{ff} (Equ. 2.8). This is evaluated for each pixel from the observed brightness B_ν which, in the optically thin case is $B_\nu = B(T)\tau$, where $B(T)$ is a blackbody with an assumed temperature T equal to the gas temperature T_e (see Table 4.3).

From the mean $< EM >$, measured in the map, inverting equation (2.11), it is possible to estimate a mean value for the particle density $< n_e >$. Assuming that the nebulae are uniform, the emission measure is simply $EM =< n_e >^2 s$, where the geometrical depth s needs a strong hypothesis regarding nebular geometries.

It has been believed that LBVNe are often torus-like, indicating that mass-loss happens in a preferred direction (e.g. Clark et al. 2003; Davies, Oudmaijer, & Vink 2005). If this is true, the nebulae associated with R127, S61 and S119 may be tori seen pole-on and that of R143 may be seen roughly edge-on. Hence we assume a depth equal to the transversal size measured on the maps, chosen where the emission is the 70% of the peak flux density (as shown with white lines in Fig. 4.1). In the cases of R127 and R143 we calculated the electron density and the ionized mass assuming two different geometrical depths (1.2" and 2.5" for R127, 1" and 3" for R143).

Finally the total ionized mass is given by the total amount of particles in the nebula, as in equation (2.13). The volume assumed for each nebula is given by the area over which we have estimated the $< EM >$ and the assumed geometrical depths. The resulting masses are reported in Table 4.5, together with the other physical parameters. The linear sizes in

the table are obtained assuming for the nebulae the distance of the LMC ($D = 48.5\,\mathrm{kpc}$).

From our estimation, the masses range from 0.5 to $1.5\,\mathrm{M}_{\odot}$, which are typical values for nebular masses of the galactic LBVs (in general few solar masses, Humphreys & Davidson 1994; Clark, Larionov, & Arkharov 2005).

4.5 Discussion/Conclusions

The improved sensitivity at ATCA with the new CABB correlator has allowed us to obtain the first radio detections of the nebula around four LBV-type stars in the Large Magellanic Cloud. Even though our highest-resolution can not distinguish angular scales smaller than 1.5" (that means structures of linear sizes ∼0.35 pc at a distance of 48.5 kpc), it was possible to measure the nebular sizes and to compare the radio morphology with the optical one. The linear sizes are consistent with previous estimates at different wavelengths (Hα, Weis 2003; Weis, Duschl, & Bomans 2003) as well as with the galactic examples (e.g. Clark et al. 2003). No evident differences are visible, as expected if the Hα is not intrinsically extinguished. On the contrary, the radio resembles the optical. A similar result was found by Duncan & White (2002), studying four galactic LBVNe and comparing the radio images with the Hα ones. The strict similarity was particularly evident in AG Car.

The radio flux densities were compared here with the extrapolated fluxes from the recombination hydrogen line. The *HST* Hα-equivalent filter F656N has a bandwidth $\approx 28\,\mathring{A}$, with the Hα line in the band centre, and does not cover Hα velocity features higher in magnitude than $640\,\mathrm{km\,s^{-1}}$. However, high-resolution Echelle spectra in Weis (2003) showed that high velocity outflows are not present in such nebulae. On the other hand, the filter can detect signal from [NII] 6548 Å emission. Assuming a mean value for the [NII]6584 Å/Hα (0.6, Smith et al. 1998) and that this is valid also for the [NII] 6548 Å line, and considering that the filter response at 6548 Å is about the 25% of the maximum, then the Hα emission evaluated here may be overestimated by 15% and thus has to be considered an upper limit.

Such contamination of Hα due to [NII] is, however, within the flux errors for most of our sources. If we assume that all the flux falling in the filter is due to Hα, comparison between the radio and optical fluxes does not show any differences and this lead us to suppose that there is not intrinsic extinction, especially in the case of R127 and S119. On the other hand, if there were some extinction this would be attributable to uniformly distributed dust, as the radio morphology resembles the optical one and we may exclude any clumping in the dust distribution.

A similar discussion must be performed with caution in the case of S61, the optical

emission of which could be affected by intrinsic extinction due to dust, and in the case of R143, which is probably affected by emission of the close HII region as well as a likely dusty environment.

The derived spectral indeces indicate a possible contribution from a central object that must be considered and, more specifically, show that current mass-loss from the central star is ongoing.

In addition, values for the ionized mass have been obtained in this work. Estimates for the nebular mass of S119 and R127 have been previously reported. In particular, Nota et al. (1994) and Clampin et al. (1993) provided a mass of $M = 1.7\,\mathrm{M}_{\odot}$ for the nebula of S119 and of $M = 3.1\,\mathrm{M}_{\odot}$ for R127. These results were obtained integrating Hα emission luminosity and adopting values for the electron density of the order $800 - 1000\,\mathrm{cm}^{-3}$, derived from the [SII 6716/6731] Å line ratio, and a temperature of 7500 K. A further value for the mass of R127 was found by Munari et al. (2009) through a photo-ionization modelling of the emission-line spectrum in the range $8400 - 8800$ Å. They found a mass of $1.33 \times 10^{-3}\,\mathrm{M}_{\odot}$.

We are conscious that the ionized mass estimated with this method is very sensitive to the assumed geometry and that we are not taking into account the filling factor correction. If these circumstellar nebulae are not homogeneous as we assumed then the true average density and hence the nebular masses are smaller than the estimates provided here by the value of the filling factor (typically between $\sim 0.2 - 0.7$ for extended nebulae, e.g. Mallik & Peimbert 1988; Boffi & Stanghellini 1994). Both these facts may lead to a discrepancy with the measurements reported in Clark et al. (Table 9, 2003).

The contribution from the stellar wind to the total emission can be neglected. In fact assuming a mass-loss rate of $\dot{M} \sim 10^{-5}\,\mathrm{M}_{\odot}\,\mathrm{yr}^{-1}$ and a stellar wind velocity of $v_{\infty} \sim 100\,\mathrm{km\,s}^{-1}$, which are typical values for galactic LBVs, the flux density due to the stellar wind will be of the order of 0.03 mJy at 9 GHz (Panagia & Felli 1975), i.e. only the 1% of the observed flux density. This means that the overestimation of the mean electron density and the ionized mass are negligible. In the case of R143, an overestimation could be assigned to the close HII region emission. The values reported here must, then, considered only as indicative, but are almost consistent with the values in Clampin et al. (1993) and Nota et al. (1994).

Thanks to its properties, radio emission can be used as a good probe of the ionized gas emission from a nebula around a hot star. This is important when one wants to determine the gas content to establish the total mass budget ejected during the LBV phase and to constrain stellar evolution models of very massive stars. For the moment, the resolution achieved at ATCA in this work does not allow us to separate the nebular and stellar

contributions to the total emission.

To resolve this issue, new higher-resolution observations can provide a more detailed morphological study of the nebula, as well as a possible detection of the central stellar wind and hence the current mass-loss rate, where the optical Hα estimates can be uncertain.

Chapter 5

High-resolution imaging and analysis of LBVNe in the LMC

Abstract

We present first high-resolution ATCA observations of the nebulae around LBV R127 and R143, and cLBV S61. The observations were carried out in band 15 mm and reached angular resolutions between 0.5" and 0.84" and sensitivities of 1.6×10^{-2} mJy beam^{-1}. The radio emission is investigated by analysing the spectral index maps, obtained using our previous radio images at 9 GHz. The nature of the radio emission is optically thin free-free, but there are hints of the presence of density clumps inside the nebulae or of background sources. A study of the central object emission in R127 provides us with the discovery of a recently formed ($\sim 10^3$ yr) mass-ejecta still close to the star. The derived current-day mass-loss rates ($\sim 10^{-5}\,M_\odot\,yr^{-1}$) are consistent with the nebula mass estimated in our previous work and lead us to suppose that the mass-loss in these objects occurs with average winds (with the exception of R143). In this analysis we also include the cLBV S119, which we presented in the previous work. The high-resolutions maps also allow a detailed comparison with the Hα *HST* images revealing, through analysis of the extinction maps, possible compact dusty regions within the nebulae.

5.1 Introduction

The first run of radio observations has allowed us to detect, for the first time, the nebulae associated with four LBVs and cLBVs in the LMC (R127, R143, S61 and S119, see Fig.4.1). Despite the very interesting results, discussed in Chapter 4, the spatial resolution was insufficient to resolve the central objects and thus to gather information on the current-day mass-loss rates. Moreover, high-resolution images in the IR domain do not exist in the data archives, in part due to the limitation in resolution of the present

Table 5.1: ATCA observational summary.

Observation Date	ATCA Config.	Band (mm)	Total integration time (min)		
12 Jan 20	6-km	15	265.3	248.3	243
12 Jan 21	6-km	15	318	345	332
12 Jan 22	6-km	15	315.3	301.7	287.7
12 Jan 23	6-km	15	83.3	82	95.7

telescopes.

Motivated by this, we have re-observed these objects at ATCA with higher-resolutions. Three of the four sources have been observed, rejecting S119, because it was not sufficiently bright to be detected at the proposed frequencies. Observations and the data reduction process are presented in Section 5.2. The nebulae were all detected at 17 GHz and their maps are described in terms of morphology in Section 5.3. A Section (5.4) is dedicated to the investigation of the nature of the radio emission: we discuss the spectral index maps, the nature of the compact object in the star position of R127 and the estimated mass-loss rates. In Section 5.5 we derive extinction maps, which give an indication of the dust distribution in such nebulae. Finally, we comment on our results and provide evidence of the feasibility of future ALMA observations.

5.2 ATCA observations and data reduction

We performed ATCA observations using the array in the most extended configuration (6-km) and the 15 mm receiver in continuum mode. We split the CABB bandwidth in two 2-GHz sub-bands, one centred at 17 GHz and the other at 23 GHz. This set-up was chosen to achieve enough spatial resolution to isolate possible contributions from the central sources and, also, to obtain some spectral information. For this project 36 h were scheduled, divided in three days (12 h per day), but about 7 h were lost because of malfunctioning of the array or because of bad weather. As a result, the total observing time obtained was 28.64 h. The first day we observed the phase calibrator (0530-727) for 1-min, alternatively with 10-min scans on targets. The second and third day we reduced the scan on targets to 7-min, because of poor weather, in order to avoid phase decorrelation. For the bandpass correction we performed observations on the calibrator 1921-293 each day as well as observations of the flux calibrator (1934-638). We also performed reference pointing very frequently (about every 1-2 h) to assure the pointing accuracy of the source

observations. Table 5.1 contains a summary of the observations and the total integration time per source.

Data reduction and imaging were performed by using the package MIRIAD. The datasets were split in two parts (one per central frequency) and hence reduced separately. For the data editing, flagging and calibration we followed the standard calibration recipe suggested for the millimetric band. In particular, data were imported in MIRIAD by using the task `ATLOD`. The opacity correction was applied during this step. Hence, after data checking, baselines that were not working properly were flagged, before calculating corrections for gains. The flagging procedure was more severe on the second and third-day datasets, when the observations were affected by bad weather. In particular the strong wind caused antennae stow during the third day and repeatedly for Antenna 5. Therefore, baselines including Antenna 5 were often removed. Moreover, because of sparse rains, the data at 23 GHz, which are sensitive to weather condition, are very noisy. We estimate that about the $10\% - 15\%$ of 23 GHz data were flagged.

Bandpass calibration was performed using the observations of 1921-293. Bad channels were removed and bandpass solutions improved. These were then transferred to the flux (1934-638) and phase (0530-727) calibrators. Time-based antenna gains were determined from the flux and phase calibrators. In particular, phase gains were obtained by interpolation between scans taken on the secondary calibrator. Finally, after the flux density bootstrapping[1], the corrected visibilities were processed for imaging.

The visibilities were hence inverted by fourier transform using the task `INVERT` in MIRIAD. In general we chose the natural weighting scheme for *uv*-data, for the best sensitivity, but in the case of R143, which is located in a crowded region. In this case we used a Briggs weighting[2], with parameter `robust=0`, in order to minimize sidelobe contribution from the strongest external sources.

The deconvolution of the dirty images (task `CLEAN`) was performed using the Clark algorithm and the selection for the clean components was done manually. After the cleaning procedure, we restored the clean components with a "clean" synthesis beam (task `RESTOR`). Table 5.2 contains information about the synthesis beam, peak flux densities and the noise of the resulting images.

Because of the unstable weather during the observations and the reduced observing time, at 23 GHz the sensitivity achieved is 3.2 times bigger than expected (0.01 mJy beam^{-1}) and we detect only the brightest compact structures. At this frequency we will

[1]The comparison between the primary and secondary gains was made selecting data at the same elevation.

[2]Which allows to produce images with a good match between the noise and the resolution.

Table 5.2: Properties of the radio maps.

Source	Frequency (GHz)	HPBW $(\text{arcsec})^2$	PA (deg)	LAS (arcsec)	Peak on-source (mJy beam^{-1})	rms (mJy beam^{-1})
R127	17	0.823×0.688	-8.0	10.9	0.165	0.016
R127	23	0.620×0.513	-8.0	8.3	0.162	0.032
S61	17	0.836×0.686	-10.6	10.9	0.142	0.016
S61	23	0.628×0.514	-10.8	8.3	0.121	0.032
R143	17	0.836×0.678	-8.8	10.9	0.192	0.016
R143	23	0.59×0.47	-8.8	8.3	0.129	0.032

present only the map of R127, whose analysis provides us with a very interesting finding (Subsection 5.4.2). Conversely, at 17 GHz the rms-noise is satisfactory (0.016 mJy beam^{-1}) and we also detected the most diffuse emission above 3σ. The radio maps at 17 GHz obtained in this work are shown in Fig. 5.1, 5.2 and 5.3, while in Fig. 5.7 we present the central object of R127 detected at 23 GHz.

5.3 Radio maps and morphology of the nebulae

The 17 GHz maps resemble those obtained at 9 GHz (Chapter 4), but with slight differences. The new maps are shown in the figures as raster images. The contour white line represents a level corresponding to 3σ, where σ is the rms-noise listed in Table 5.2. In order to better understand the morphology of the radio emission over the nebulae, we also show in the figures the average surface brightness profiles. These were extracted from 18 cuts in each map and then azimuthally-averaged.

In the map of R127 a hint of the central object is visible, as in the 9 GHz map. Consistently with the Hα and the 9 GHz emission, the radio shell is roughly symmetric with respect to the vertical axis, with bright features in the east and west (*Rims* in Weis 2003) and quite detached components in the north and south (*Caps* again in Weis 2003).

After spectro-polarimetric studies, Schulte-Ladbeck et al. (1993) and Davies, Oudmaijer, & Vink (2005) pointed out that the nebula around R127 is an equatorial disk seen edge-on. They also investigated the stellar wind, finding that the mass-loss is asymmetric and equatorially aligned with the outer nebula. Smith et al. (1998) found two velocity components in the nebula around the star. In particular, the inner part ($\sim 0.6\,\text{pc}$ far from the star) has an expanding velocity $29\,\text{km s}^{-1}$, the outer one has $v_{exp} = 25\,km\,s^{-1}$. Later,

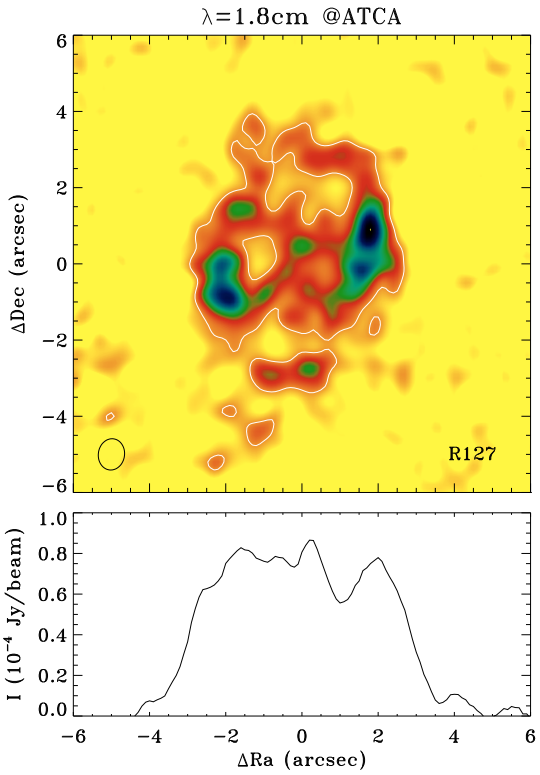

Figure 5.1: Top: ATCA map of R127 at 17 GHz. The beam is 0.823"×0.688" at PA of -8° and it is represented in the bottom left corner with a black circle. The peak flux density on the nebula is 0.133 mJy beam^{-1} and lowest level is equal to the rms-noise (σ=0.013 mJy beam^{-1}). The white contour corresponds to a level of 3σ. Bottom: Average surface brightness profile.

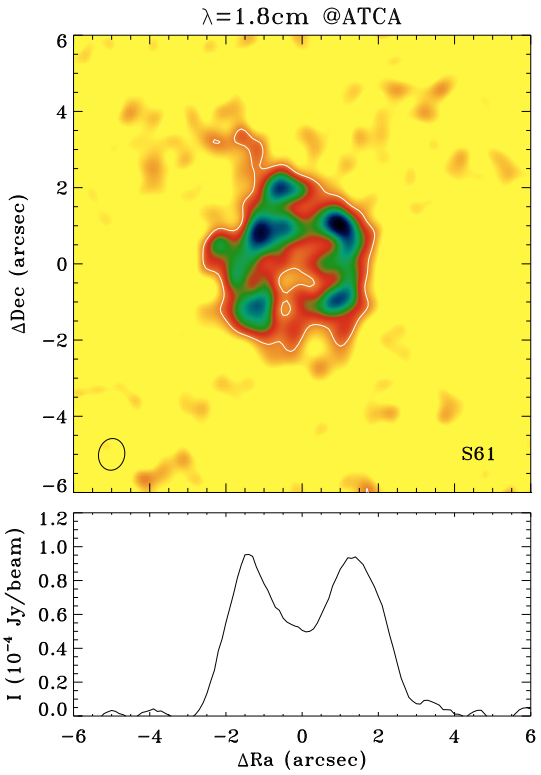

Figure 5.2: Top: Map of S61 at 17 GHz obtained at ATCA. The synthesis beam is 0.836"×0.686" at PA -10.6° (white circle in the left corner). The peak flux density on the nebula is 0.114 mJy beam^{-1} and lowest level is equal to the rms-noise (σ=0.013 mJy beam^{-1}). The white contour corresponds to a level of 3σ. Bottom: Average surface brightness profile extracted from 18 cuts along the nebula.

Weis (2003) noted that the north region is blue-shifted and the south region red-shifted in respect to the centre motion.

Our radio image is consistent with an equatorial disk seen edge-on. We interpret the vertical shift of the peak in the western *rim*, in respect to the eastern one, as an inclination (anticlockwise) of the RA axis. The blue-shifted and red-shifted *caps* indicate a further inclination toward the line of sight in the north. In the position of the two *caps*, Weis (2003) found smaller expansion velocities (at most 15 km s^{-1} in the north and 12.3 km s^{-1} in the south) in respect to the velocity measured in the rest of the nebula (with a peak of $v_{exp} = 31.5$ km s^{-1} near the star). If this is true, then we can speculate that the two *caps*, which are slower and more distant (0.84 pc) than the *rims* (0.69 pc) from the star position, are related to a different and to an older mass-loss episode. They appear to detach from the nebula body.

The nebula of S61 at 17 GHz shows again a roughly spherical symmetry, thinner in the south part than in the north. The central object is not detected, but a new compact

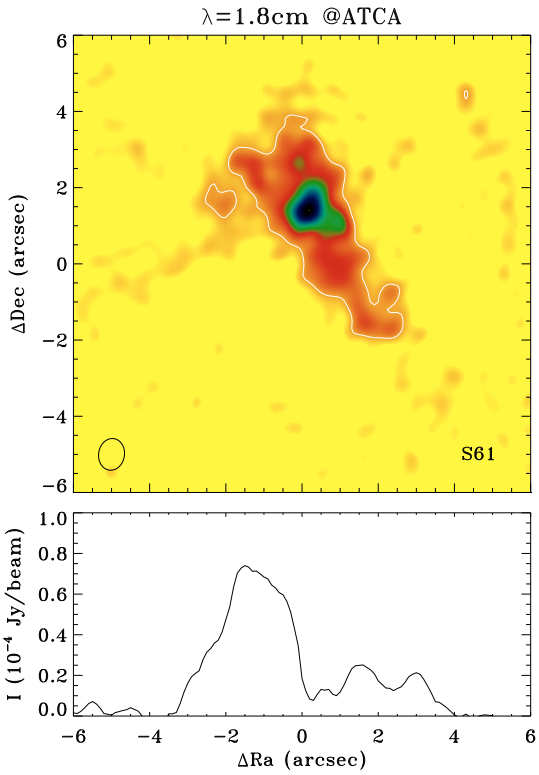

Figure 5.3: Top: ATCA map of R143 at 17 GHz. The beam is 0.836"×0.678" at PA -8.8°. The peak flux density on the nebula is 0.154 mJy beam^{-1} and the rms-noise σ is 0.013 mJy beam^{-1}. The white contour corresponds to a level of 3σ. Bottom: Average surface brightness profile.

region above 3σ appears in the north, close to the nebula. With her kinematical study, Weis (2003) also found that the nebula expansion is spherical (globally $v_{exp} \sim 27\,\mathrm{km\,s^{-1}}$), but slightly red-shifted to the west and blue-shifted to the east. Hence she supposed a geometric distortion in the line of sight.

R143 has the only known irregular nebula. Weis (2003) reported the presence of a nebula in the north-east of the star with two velocity components, one moving at $v_{exp} \sim 19\,\mathrm{km\,s^{-1}}$ and another at $v_{exp} \sim 43\,\mathrm{km\,s^{-1}}$. The radio nebula is triangular-shaped, similarly to the optical emission, and has no counterpart in the east and south-east side of the star, but shares the same asymmetry of the ionized component of LBVNe IRAS 18576+034 (Fig. 1.9). This time the array filtered out the extended emission from the close HII region. We do not detect emission in the position of the star at 17 GHz, whereas in the 9 GHz map there is a hint of the central object (circle "b" in Fig. 4.1).

Table 5.3: Observed flux densities and angular sizes at 17 GHz. Spectral index between measurements[a] at 5.5, 9 and 17 GHz.

Source	S_{obs}(17 GHz) (mJy)	Angular sizes	$< \alpha >$
S61	1.97 ± 0.10	4.5"×4.9"	-0.06±0.06
R127	3.12 ± 0.14	6.0"×7.3"	0.00±0.07
R143	1.44 ± 0.08	2.25"×6.16"	-0.51±0.07

[a] For flux density values at 5.5 and 9 GHz see Table 5.3.

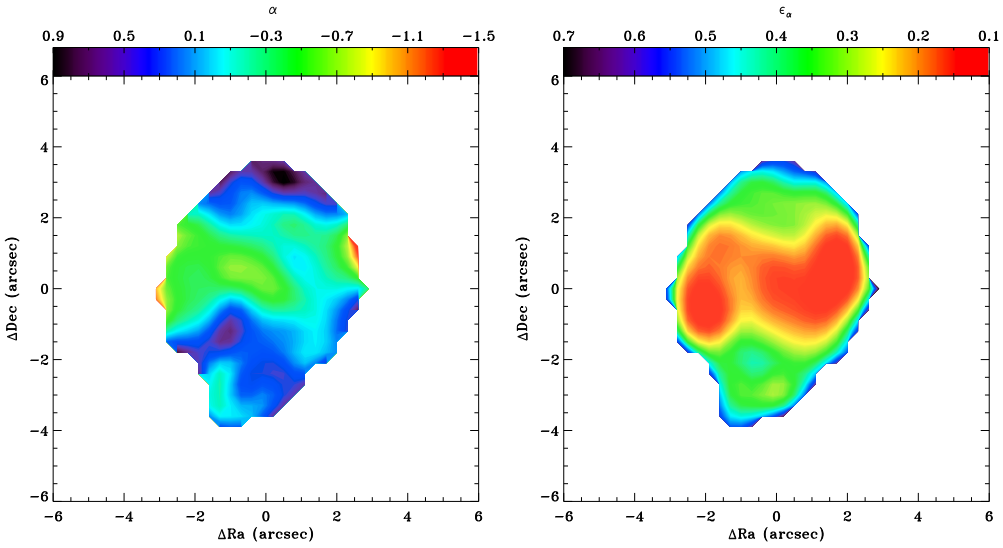

Figure 5.4: Left: Spectral index map of R127 between 9 and 17 GHz. Right: error spectral index map.

5.4 Analysis of the radio emission

From the radio maps we have estimated the flux density and its associated error by using the CASA viewer. In particular, we selected with a polygonal tool the area above 3σ level and integrated the emission over the nebula. The rms-noise in the maps was evaluated in regions free of emission and hence flux density errors were estimated as in equation (4.3). The values found are listed in Table 5.3, together with the estimated nebula angular sizes.

5.4.1 Spectral index analysis

We have derived the average spectral index $< \alpha >$ for each nebula by means of a weighted polynomial fitting of the flux densities at 5.5, 9 (Table 4.5) and 17 GHz. The resulting $< \alpha >$ is in Table 5.3 together with its error. In the case of R127 and S61 the spectral index is consistent with optically thin free-free emission, typical in LBVNe. In the case of R143 it indicates a quite steep SED and may be due to the contribution from the central

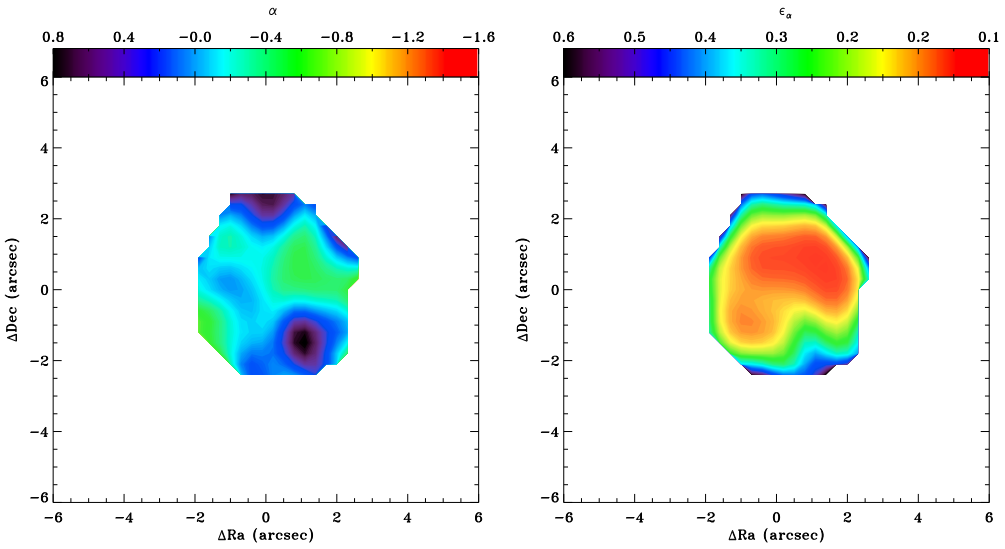

Figure 5.5: Left: Spectral index map of S61 between 9 and 17 GHz. Right: error spectral index map.

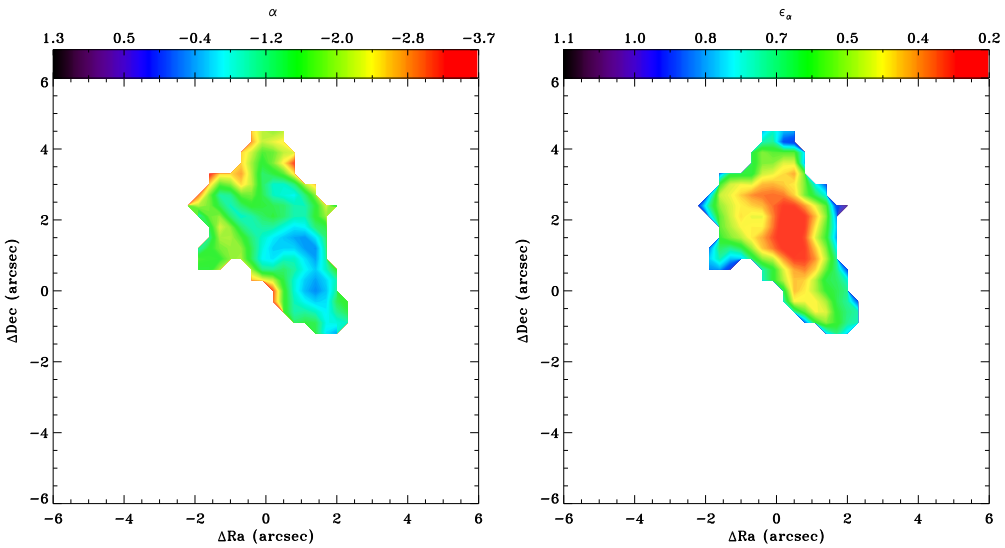

Figure 5.6: Left: Spectral index map of R143 between 9 and 17 GHz. Right: error spectral index map.

object and from the close HII region emission, significant at 9 GHz.

We have also obtained spectral index maps for these sources adopting the method described in Section 2.4. In particular we used the maps at 17 GHz and those at 9 GHz. The highest-resolution maps (17 GHz) were re-gridded in the same grid of the lowest-resolution maps and then convolved with the beam at 9 GHz (with HPBW about 1.5" $\times$ 1.2"). Hence, for each source the spectral index map and its associated error map were obtained following equations (2.6) and (2.7), but this time with 17 GHz instead of 5 GHz and 9 GHz instead of 1.4 GHz. In equation (2.7) the error in each pixel is given by the contribution of the rms-noise in Jy pixel^{-1} unit, since calibration errors are negligible. The result of this procedure is shown in Fig. 5.4 for R127, in Fig. 5.5 for S61 and finally in Fig. 5.6 for R143.

R127 The green and blue levels are consistent with optically thin free-free emission. These values are spread over the nebula, but in the south and north regions (corresponding to the *caps*), where α increases slightly. In the furthest north region and in the middle left part, it reaches values 0.93 ± 0.45, typical of stellar winds or of density clumps.

We exclude that the northern region is an artefact because at the same position we detected two compact objects[3] above 3σ in the 23 GHz map.

S61 In the green and blue levels the average spectral index is -0.28 ± 0.16, yet consistent with optically thin emission. Evidence of density clumps comes from the south-west and the north (but we can not exclude the possibility of emission from background sources, especially in the north position of the nebula). Though the errors are higher here, α_{max} is well above 0.4 (0.79 ± 0.31).

R143 Over the nebula α is very low (< -1). This value is typical of synchrotron emission. If we exclude the presence of strong magnetic fields, the only explanation is that at lower frequency the array did not filter out the extended emission from the background, as R143 is located in a rich environment of nebulosity. However, in the inner region (blue levels) α is consistent with optically thin bremsstrahlung emission.

5.4.2 The nature of the inner object in R127

The highest-resolution map at 23 GHz (Fig. 5.7) shows a compact emission region in the position of the star. To explore the nature of this object we have fitted it with an elliptical

[3]These two compact objects at the position of the north *cap* have peak flux densities respectively 0.11 mJy beam^{-1} and 0.096 mJy beam^{-1}, where the beam is in Table 5.2.

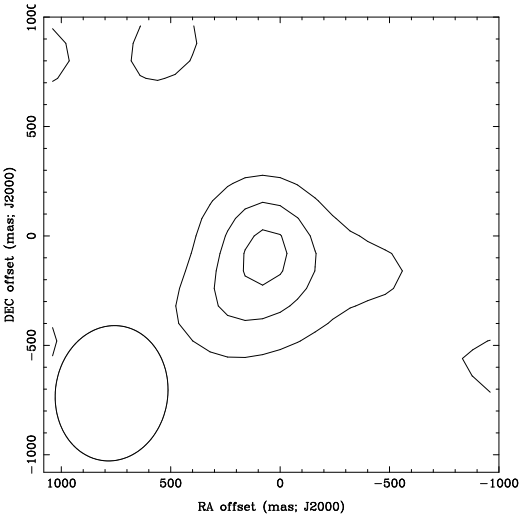

Figure 5.7: Zoomed-in figure of R127 central object from the ATCA 23 GHz map. Contour levels above 3σ are plotted. The circle in the bottom-left corner is the synthetic beam.

Gaussian with HPBW 0.62"×0.51" at PA -8 deg and centred at RA 05:36:43.692 and DEC -69:29:47.631. The function was constrained above the 3σ level of brightness. The derived peak flux density and integrated flux density are respectively 0.148 mJy beam^{-1} and 0.253 mJy, showing that the region is resolved by the array configuration at this frequency. In fact, the deconvolution from the beam gives us angular sizes of 0.568"×0.359" at PA -75.4 deg, with the largest size elongated in the east-west direction. These measurements correspond to 0.13×0.08 pc at an assumed distance of 48.5 kpc.

For a star which is experiencing mass-loss, the mass-loss rate can be determined from the radio flux density F_ν as in equation (2.14).

Assuming as terminal velocity of the wind $v_{exp} = 110\,\mathrm{km\,s^{-1}}$ (Stahl et al. 1983), D the distance in kpc of the LMC and the flux density obtained at 23 GHz, the corresponding mass-loss rate is $2.98 \times 10^{-5}\,\mathrm{M_\odot\,yr^{-1}}$, which is a typical value for LBVs and it is still consistent with the value ($6 \times 10^{-5}\,\mathrm{M_\odot\,yr^{-1}}$) obtained by Stahl et al. (1983) by fitting the Balmer lines and modelling the IR fluxes.

Using our value we have determined the theoretical sizes of this compact object at 23 GHz, to compare them with those observed. For stars undergoing mass-loss, Panagia & Felli (1975) determined the effective radius of the emitting region as a function of $\dot{M}$, as in equation

$$R(\nu) = 6.23 \times 10^{14} \left(\frac{\nu}{10\,\mathrm{GHz}}\right)^{-0.7} \left(\frac{T_e}{10^4\,\mathrm{K}}\right)^{-0.45} \left(\frac{\dot{M}}{10^{-5}\,\mathrm{M_\odot\,yr^{-1}}}\right)^{2/3} \left(\frac{v_{exp}}{10^3\,\mathrm{km\,s^{-1}}}\right)^{-2/3} [\mathrm{cm}] \tag{5.1}$$

in the assumption that the gas is mostly hydrogen. Adopting as electron temperature T_e=6420 K (Smith et al. 1998) we find a radius of 3.83×10^{15} cm, i.e. a linear dimension

of 1.2×10^{-3} pc, which is about 100 times smaller than the observed sizes.

This result indicates that the central object in the position of the star is an inner shell, which we can estimate to be formed at most 1200 years ago (if we assume a kinematical expansion of $110\,\mathrm{km\,s^{-1}}$ equal to the terminal wind velocity) or 4500 years ago (assuming $v_{exp} = 29\,\mathrm{km\,s^{-1}}$, Smith et al. 1998). In fact, Schulte-Ladbeck et al. (1993) and Smith et al. (1998) found hints of the presence of circumstellar matter close to the star, expanding at higher velocity ($v_{exp} = 29\,\mathrm{km\,s^{-1}}$) in respect to the outer shell ($v_{exp} = 25\,\mathrm{km\,s^{-1}}$). Through a spectroscopic analysis in the optical, Weis (2003) found [NII] line emission with a velocity similar to those of the star. She explained it as a possible shell close to the star but could not support this hypothesis with the optical images, because the Hα emission from the star saturated the central part of the image. Our work allows to confirm the presence of a shell of recent formation.

In this case, the mass-loss rate provided above is overestimated. We can calculate an upper limit considering F_ν in equation (2.14) the peak flux density (0.148 mJy beam^{-1}). In this case we find $\dot{M} = 2\times10^{-5}\,\mathrm{M_\odot\,yr^{-1}}$.

We also derived the ionized mass contained in such shell. Adopting equation (2.11), we derive $< EM >= 1029\,\mathrm{pc\,cm^{-6}}$. We assume a geometrical depth of the shell (which is very likely an equatorial torus) equal to the smaller size (0.359"), and hence we find $< n_e >= 110\,\mathrm{cm^{-3}}$. The mass is obtained by using equation (2.13), where the torus volume is approximated by a box of sizes equal to the measurements provided above. The value found is $M_{ion} = 2.6\times10^{-3}\mathrm{M_\odot}$. Considered the current-day mass-loss rate, this gives us a lower limit for the epoch of its formation, which occurred at least 130 years ago.

5.4.3 Nebula mass versus $\dot{M}$

Though we did not detect any compact objects in the stellar position of R143 and S61, we can constrain their current-day mass-loss providing an upper limit. In fact, considering the sensitivity achieved at 23 GHz ($\sim 0.032\,\mathrm{mJy\,beam^{-1}}$) and assuming for each star the terminal wind velocity in literature (as in Table 5.4), we derive $\dot{M} < 1.4\times10^{-5}\,\mathrm{M_\odot\,yr^{-1}}$ for S61 (consistently with Crowther & Smith 1997, who report $\dot{M} = 1.1\times10^{-5}\,\mathrm{M_\odot\,yr^{-1}}$) and $\dot{M} < 7\times10^{-6}\,\mathrm{M_\odot\,yr^{-1}}$ for R143. These values are summarized in Table 5.4, together with those of R127, estimated in the previous subsection, and of S119, found in the literature.

Adopting the nebular expansion velocity in the literature and considering the nebula size in the expansion direction, we derived the kinematical ages, which provide us an upper limit to the epoch of the mass-loss (as in Table 5.5). The nebula of S119 is the

Table 5.4: Terminal wind velocity, mass-loss rate, UV flux, spectral type.

Source	v_∞ $(\mathrm{km\,s^{-1}})$	$\dot{M}$ $(\mathrm{M_\odot\,yr^{-1}})$	log(FUV)	Spectral Type
S61	250[a]	$< 1.4 \times 10^{-5}$	45.67	B2-B3
R127	110[b]	$< 2 \times 10^{-5}$	46.41	B1
R143	130[c]	$< 7 \times 10^{-6}$	45.9	B2-B3
S119		1.34×10^{-5} [a]	47.37	B0.5-B1

[a] Crowther & Smith (1997)
[b] Stahl et al. (1993)
[c] Smith et al. (1998)

Table 5.5: Size, expansion velocity, kinematical age.

Source	size (pc)	v_{exp} $(\mathrm{km\,s^{-1}})$	t_{nebula} $(\times 10^4\,\mathrm{yr})$
S61	1.17	27[a]	4.2
R127 (inner shell)	0.57	30[b]	0.12
R127 (outer shell)	1.65	30[b]	5.4
R143	0.59	24[c]	2.4
S119	1.90	25.5[d]	7.2

[a] Nota et al. (1994); Weis, Duschl, & Bomans (2003)
[b] Stahl & Wolf (1986)
[c] Weis (2003)
[d] Nota et al. (1994); Weis, Duschl, & Bomans (2003)

oldest one and this is consistent with its gas distribution, which appears to be dispersed. S61 and R127 share similar kinematical ages, while R143 appears to be the most recent formed (excluding the inner shell of R127).

With the current-day mass-loss rate estimated above and the kinematical ages derived for the nebula, we find that the nebula mass should be $1.1\,M_\odot$ (R127), $0.6\,M_\odot$ (S61), $0.2\,M_\odot$ (R143) and $1\,M_\odot$ (S119). These values, compared with the masses derived in Section 4.4.2, indicate that these stars lost mass with quite constant and conspicuous rates ($\sim 10^{-5}\,M_\odot\,yr^{-1}$). The only exception is R143, which has a lower current-day mass-loss ($< 7\times10^{-6}\,M_\odot\,yr^{-1}$) and has a nebula mass three-four times bigger than those produced at this rate. This means that R143 had to suffer higher mass-loss rates in the past and may be consistent with a scenario where the star is moving toward the quiescent state.

5.4.4 Spectral type of the stars

We also derive the spectral type of these stars, by considering the ionized budget in the nebulae. Following the method described in Section 2.4.3 and using equation (2.16), we derive the ionizing photon flux and hence the spectral type for these stars (see Table 5.4). The considered average electron densities and ionized mass are those estimated in Section 4.4.2.

The hottest star is S119, which contains the oldest nebula among our sub-sample of LBVs. Currently the star has been classified as Ofpe/WN9 because any spectroscopic or photometric variability was not observed. Together with S61, it seems however to be cooler than expected by the spectral classification. This might mean that these objects are moving toward the active state. Only further spectroscopic observations can help with this understanding.

About R127, Walborn et al. (2008) analysed the spectroscopic and photometric variations of the star over the last 30 years. After the first observed outburst (between 1978 and 1980) R127 started a path toward the quiescent state, when it became the brightest star in the LMC (Walborn et al. 2008) at the end of the 80s. These authors also argued that the star has probably begun its decline from the last outburst. According to the last spectral and photometric observations, we can confirm from the radio measurements that the spectral type associated with R127 is B1.

Parker et al. (1993) classified R143 as LBV, after they studied the spectroscopic and photometric variations of the star over the past 40 yr. They pointed out that at the time of the last observation the star was moving toward the red and appeared to be a late B supergiant. If our estimation is correct, then R143 already passed the active state and it is now in its minimum.

5.5 Extinction maps: evidence of dust?

Up to now, the available mid-IR telescopes have not been suited to sufficiently high-resolution and high-sensitivity observations of nebulae at the distance of the LMC. Motivated by this fact, we have compared pixel by pixel the highest-resolution radio emission (17 GHz) with those in the Hα, analysed in the previous Chapter 4, to investigate possible extinction of the optical light. Before this, we subtracted the optical stellar emission from each Hα image and substituted it with average nebular brightness evaluated in annuli around the star. We re-gridded the *HST* images to the same grid of the radio maps and converted the former ones in Jy pixel^{-1} unit, according the procedure described in Section 2.4.

Hence, we convolved the optical images with the radio beam, modelled with a Gaussian distribution with $\sigma^2 = \frac{1}{8ln2} HPBW^2$ (HPBW as in Table 5.2).

Adopting the same values for the electron temperature as in Table 4.3 and equation (4.1), we derived for each source the expected radio map from the Hα recombination-line emission. Since the *HST*/WFPC2 images are in counts$/$(pixel Å) unit and the optical flux in equation (4.1) must be expressed in erg cm^{-2} s^{-1}, we multiplied them for $2.9 \times 10^{-16} \times$ 21.5 (where 21.5 is the F656N filter bandwidth in *Å*).

Finally, the extinction map was derived as the ratio between the observed radio map and those expected from the recombination-line in each pixel with brightness above 3σ (where this time σ was evaluated in free-emission regions of the final images). As a result of this procedure, we obtained the extinction maps illustrated in Fig. 5.8, 5.9 and 5.10.

The most extinguished nebula is those of R143, where extinction is evident over all the region, with evidence of compact clumps inside the nebula.

R127 suffers very slightly of intrinsic extinction, but interesting are the dark regions, in the positions of the *caps*. These regions resulted to be slower in the expansion motion (Weis 2003), more distant from the star and, in our map, also detached. Bonanos et al. (2009) reported a mid-IR excess of the star through photometric SAGE observations obtained with *Spitzer*. Therefore, to explain the SAGE observations and the extinction map, we can speculate that the radio nebula is surrounded by a dusty component, similarly for example to the galactic G79.29+0.46, which has multiple dust shells outer of the ionized gas. If this is true, this dust nebula may be related to a previous mass-loss episode.

In the case of S61, strong intrinsic extinction results in the northern part (where the spectral index is above 0.4), as well as in the south-west part. The extinction map resembles the dusty nebula around the LBV 18576+034 (Fig. 1.9, Buemi et al. 2010).

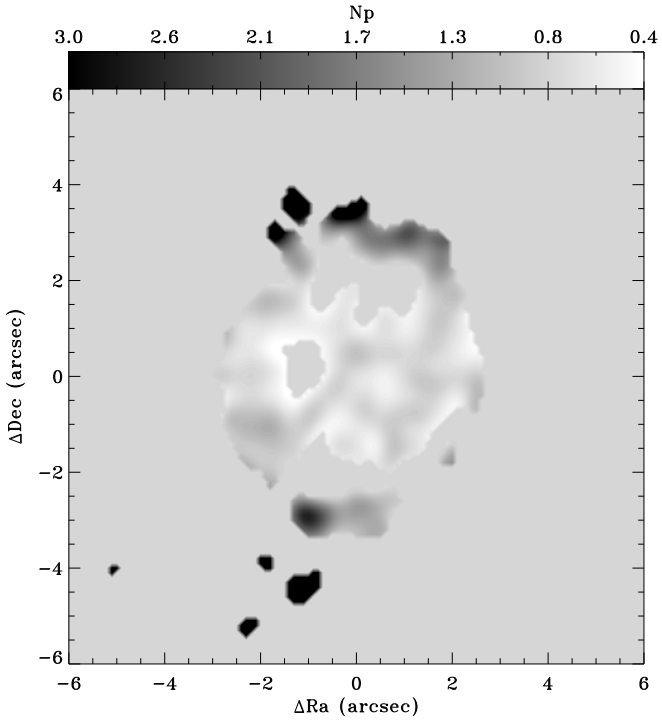

Figure 5.8: Extinction map of R127. Levels in black are equal or greater than 3.

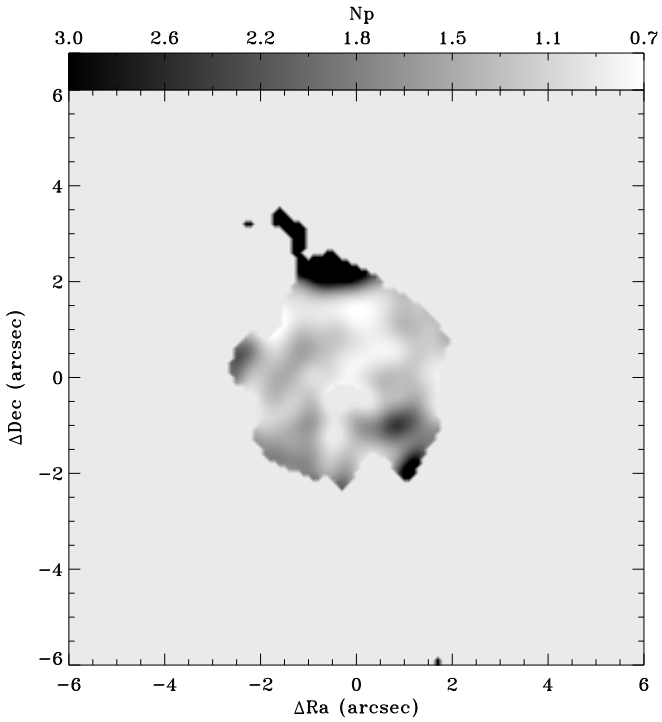

Figure 5.9: Extinction map of S61.

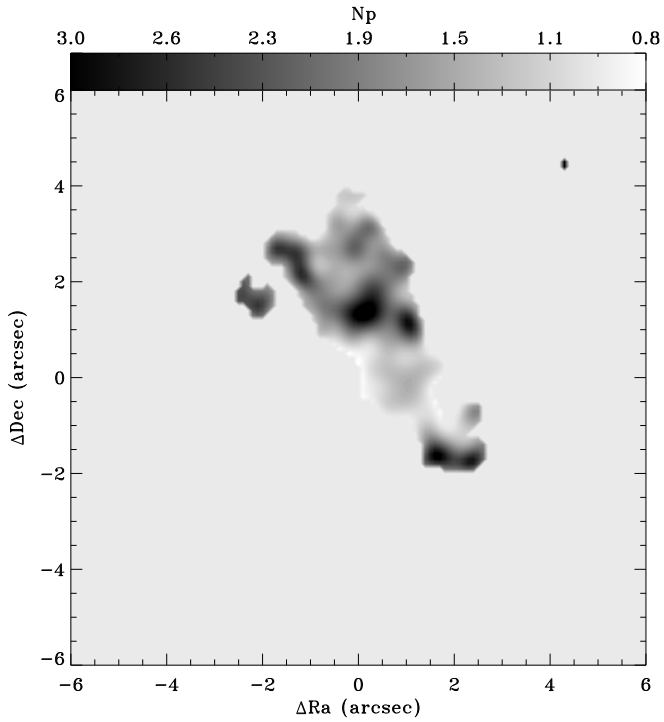

Figure 5.10: Extinction map of R143.

5.6 Discussion/Conclusions

Our high-resolution maps of R127 at 17 and 23 GHz reveal the presence of an ionized region (~ 0.13 pc) close to the star, torus-like shaped, as showed by the elongation of the emission in the east-west direction, and seen edge-on, supporting the geometry presented by Schulte-Ladbeck et al. (1993), where the mass-loss is ongoing through an asymmetric and equatorial wind and the old shell was formed in such way. We support this geometry, adding evidence of the presence of a recently ($\sim 10^3$ yr) formed shell and two expanding *caps*, probably ejected before the torus-disk. The radio emission is consistent with optically thin free-free radiation, but the spectral index in the north *cap* and in the south of the disk indicates the presence of density clumps. We can not exclude, however, the contribution of background sources (for instance, stellar winds). Interesting may be the possibility that R127 is in a binary system, as supposed by Schulte-Ladbeck et al. (1993) and in analogy with the galactic HR Car (White 2000).

As already reported by Walborn et al. (2008), which analysed the spectroscopic and photometric variations of the star over the last 30 years, the track in the H-R diagram of R127 indicates that it is ongoing toward the quiescent state. Walborn et al. (2008) also argued that the star has likely begun its decline from the last outburst. We confirm from the radio measurements that the spectral type associated with R127 is B1. Considering that the last observed outburst was experienced by the star in the decade 1986-1998, it is

likely that the star is declining toward the minimum, quiescent state Ofpe, where it was observed in 1975 (Walborn 1977).

R127 was recently observed within the *Spitzer* SAGE Infrared Photometry survey in the LMC (Bonanos et al. 2009). In this work the authors report the detection of R127 at 70 μm and attribute it to a dusty environment around the star (though they did not resolve it). Based on our observations, we can assess that the nebula is not strongly extinguished and we suggest that if a dusty nebula is attributable to R127, this must be distributed outer than the ionized gas. This is consistent with the galactic cLBV G79.29+0.46 (Chapter 2), for example, which has a second and outer shell emitting in the far-IR, while the gas is concentrated in the inner shell.

We confirm that R143 nebula is strongly irregular, without a counterpart in the opposite side of the star. The spectral index of the radio emission indicates a quite steep SED for the nebula, but we believe that this is due to the fact that at 9 GHz we do not resolve out the background emission related to the close HII region.

Comparison between the derived spectral type (B2-B3) and the last report in Parker et al. (1993) lead us to suppose that the star is moving toward the quiescent state. This is confirmed by the mass-loss rate, which we estimated to be $< 7 \times 10^{-6} \mathrm{M}_{\odot}\,\mathrm{yr}^{-1}$.

The nebula of R143 appears to be extinguished by dust. Since R143 is located in a region of nebulosity, we can not determine if the extinction is intrinsic or due to interstellar dust. Unfortunately, our spectra index map can not help with the understanding of the nature of the bright compact radio emission in the north of the star position, which is also strongly extinguished.

S61 has a morphology that resembles in the optical a spherical disk, but in the radio it is not well-drawn. It might be a torus-like shell seen face-on. In this case, it may be similar to the ejecta of R127, but at an younger stage, since it has a kinematical age and nebula sizes a bit smaller than R127. S61 has not been observed in active state, and for this reason it is still a candidate LBV. Its radio emission is consistent with optically thin free-free emission, but analysis of the spectral index in the north and in the south part of the nebula indicates the presence of density clumps (or of background sources). Very interesting is the extinction map obtained in this work, which reveals very likely the presence of a dusty optically thin nebula, probably more extended than the ionized gas, whose morphology resembles those of the galactic LBV IRAS 18576+034 (Fig. 1.9, Buemi et al. 2010).

The spectral type derived for the star corresponds to an object colder (B2-B3) than what found (O supergiant) with a spectroscopic study in 1997 by Walborn et al. This may indicate that the star is moving toward the active state, but only further spectroscopic

observations can confirm it.

The estimated current-day mass-loss rate for all the sources are consistent with the observed mass (excluding the case of R143), indicating that these objects are losing mass with constant winds. Conversely, the current-day mass-loss rate of R143 does not explain the estimated mass. Hence we believe that the bulk of the nebula mass is related to a more conspicuous mass-loss episodes occurred in the past.

5.7 Outlook

Up to now we have been far to obtain high-resolution images of infrared LBV nebulae in the Magellanic Clouds. The smallest angular scales achieved by *Spitzer* are 2" in the IRAC bands and 6" in the MIPS bands (precisely at 24 μm). This resolution are good enough to resolve a possible dusty shell, but the star is very bright, especially at the IRAC bands, and obscures any possible nebular component. However, a *Spitzer* infrared photometric survey (SAGE) of massive stars in the LMC included the observation of R127. Bonanos et al. (2009) report the detection of this star at 70 μm and an infrared excess in respect to the IRAC-bands emission, which may imply that a dusty environment exists around this star.

Conversely, our analysis reveals that the nebula of R127 does not suffer of strong intrinsic extinction, except in the north-south direction. Therefore, if dust is present, it must be optically thin, otherwise the dusty nebula should be located at outer radii in respect to the ionized gas distribution. If this is true, optical and radio observations can not provide any evidence of the whole dust content in R127.

In this Section we create a model of dust for R127 and provide a simulation of ALMA observations, which represents the future for far-IR and sub-mm wavelengths with angular resolutions never achieved in these bands.

5.7.1 Modelling the dust nebula in R127

The extinction map in Fig. 5.8 shows that mostly the whole nebula is not intrinsically extinguished, except in the north and south *Caps*, where the optical flux may be. Hence we guess that we do not see extinction because the dust is optically thin or because it is distributed in an external shell.

We assume that a torus of optically thin dust is present in the north-south direction, thicker in the positions of the two *Caps* and seen edge-on, with a size of 8" in the north-south direction and 2" in the east-west (green, in Fig. 5.11) and that the dust emission is thermal, described by a Planckian distribution of temperature $T \sim 100\,\mathrm{K}$. We consider

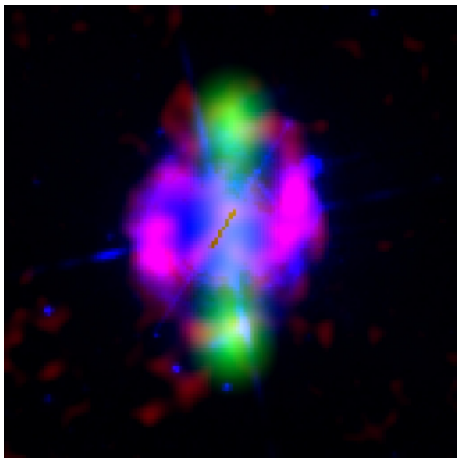

Figure 5.11: R127 composite image. Red: ATCA 17 GHz observed map. Green: our model for the dust. Blue: Hα *HST* observed image.

to possible cases for the dust composition: graphite or silicates. Using the absorption coefficients for graphite and silicates computed by Umana et al. (2010) (Fig. 3.11), we can derive the optical depth for the dust pixel per pixel, at a given wavelength, in both the cases as

$$\tau_{dust}(\nu) = \frac{\kappa_{dust}}{\kappa_{\mathrm{H}\alpha}} \times \tau_{\mathrm{H}\alpha} \tag{5.2}$$

In the sub-mm range, $\kappa_{graphite} \sim 2\,\mathrm{cm^2\,g^{-1}}$ and $\kappa_{silicates} \sim 1\,\mathrm{cm^2\,g^{-1}}$, while in the optical range the absorption is more important, with $\kappa_{graphite} \sim 2 \times 10^4\,\mathrm{cm^2\,g^{-1}}$ and $\kappa_{silicates} \sim 10^3\,\mathrm{cm^2\,g^{-1}}$. By using these values we can obtain the optical depth maps in the case of graphite and silicates. We computed these maps at 350 and 700 GHz, which fall respectively in the ALMA band 3 and 9. Then we derived the brightness that we expect in the sub-mm by using the radiative transfer equation, in the case of an optically thin nebula, not absorbed along the line of sight.

5.7.2 Simulation of ALMA observations

We simulated ALMA observations by using the task `SIMDATA` of the CASA package, version 3.4. We used as input a model image of dust in a torus-like configuration, seen edge-on (green, in Fig. 5.11). The pixel of the image was chosen arbitrarily equal to 0.1". In the task `SIMDATA` we assigned for the antenna positions those in the compact configuration, available in ALMA Cycle 0. The task requires the surface brightness of the brightest pixel. In particular, this brightness peak was derived where the optical depth is maximum (corresponding to the north and south edges of the torus, Fig. 5.11), at frequencies of our interest (for instance, 345 GHz and 700 GHz).

For the simulation, we chose the worst case for detection, i.e. the graphite case. In

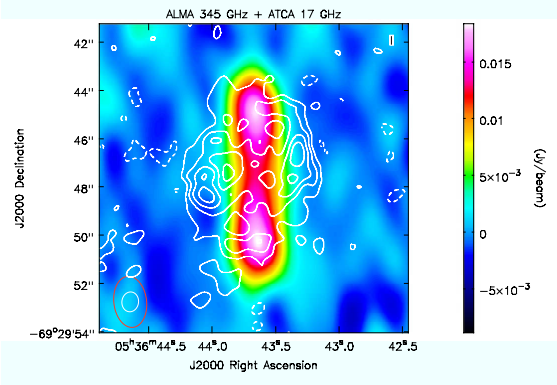

Figure 5.12: Raster image: dust emission at 345 GHz, simulated with ALMA Cycle 0 in the compact configuration. Contours: ionized gas emission at 17 GHz observed with ATCA in this work.

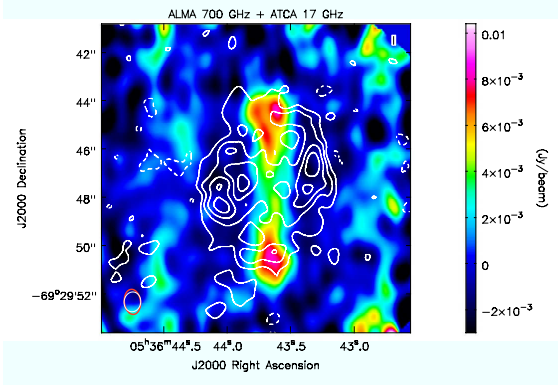

Figure 5.13: Raster image: dust emission at 700 GHz, simulated with ALMA Cycle 0 in the compact configuration. Contours: ionized gas emission at 17 GHz observed with ATCA in this work.

fact, in this case, the Hα absorption coefficient is greater than for silicates (see $\kappa_{\mathrm{H}\alpha}$). The expected brightness will be smaller than in the case of silicates. Then, in the case of graphite, $I_{peax}(345\,\mathrm{GHz}) = 2.06 \times 10^{-5}\,\mathrm{Jy/pix}$ and $I_{peak}(700\,\mathrm{GHz}) = 8.45 \times 10^{-5}\,\mathrm{Jy/pix}$. In the simulation, we also added the thermal noise by using default values provided in the task.

With a beam of $(1.55")^2$ in the compact configuration of ALMA, $I_{peax}(345\,\mathrm{GHz}) = 5.6\,\mathrm{mJy\,beam^{-1}}$. Hence we found that, with a total integration time on source of 20 s, we will obtain a sensitivity of about $1\,\mathrm{mJy\,beam^{-1}}$. The simulation obtained with `SIMDATA` provide a collection of visibilities that can processed for imaging. We used the task `CLEAN` for fourier trasforming the visibilities and for cleaning the dirty image.

The resulting map is showed in Fig. 5.12. In the bottom left corner of the maps we represent with an elliptical shape the ALMA beam in red and the ATCA one in white.

Simulating the highest frequency available at ALMA during the Cycle 0, that means a beam of $(0.8")^2$ in the compact configuration, $I_{peak}(700\,\mathrm{GHz}) = 6\,\mathrm{mJy\,beam^{-1}}$, and an total integration time on source 30 m, we will obtain a sensitivity of about $2\,\mathrm{mJy\,beam^{-1}}$ (Fig. 5.13). The beam obtained in this last case is comparable to the resolution of the ATCA map at 17 GHz.

We excluded from the model the free-free emission contribution at this range of frequencies, because we wanted to focus the discussion on the detection of dust.

Once obtained the map for the dust, we will be able to estimate the mass and dust temperature, hence the total budget for the nebular mass. The gas-to-dust ratio will be also considered and compared with the interstellar value. Finally, it will be possible to recover the mass-loss history in the LBVNe of the LMC by analysing the distribution of different emitting components.

Acknowledgments

The Australia Telescope Compact Array is part of the Australia Telescope National Facility which is funded by the Commonwealth of Australia for operation as a National Facility managed by CSIRO. This research has made use of the SIMBAD database, operated at CDS, Strasbourg, France. It is also based on observations made with the NASA/ESA Hubble Space Telescope, and obtained from the Hubble Legacy Archive, which is a collaboration between the Space Telescope Science Institute (STScI/NASA), the Space Telescope European Coordinating Facility (ST-ECF/ESA) and the Canadian Astronomy Data Centre (CADC/NRC/CSA).

Discussion and Conclusions

A way to comprehend the LBV phenomenon is to study the circumstellar matter ejected during the LBV phase, since these nebulae contain the fingerprints of the mass-loss history, including different mass-loss episodes occurred during this quite intriguing evolutionary phase of massive stars.

In this work we investigated the mass-loss phenomenon in a sub-sample of LBV stars, through a multiwavelength analysis of their ejecta, probing the current-day mass-loss of the star and the mass lost in previous events.

One of the goal of this thesis was to investigate the mass-loss history of the candidate LBV G79.29+0.46, which is one among the most interesting objects in our Galaxy. Therefore, we presented an example of multiwavelength study, performed by considering photometric and spectroscopic data, ranging from the mid-IR to the radio domain, that allowed us to probe different emitting components coexisting in the nebula. Similar investigation may be then used as template to identify new objects by analysing their ejecta.

Among the motivations of this thesis there was also the possibility that the LBV phenomenon is metallicity independent. We have hence started a pilot study at the radio wavelengths of LBV ejecta in the LMC, which is the closest galaxy to the Milky Way and has half the solar metallicity. We investigated the mass-loss history of four sources in the LMC through analysis of the ionized gas emission, and also provided evidence of dusty components.

We summarize the main results of this thesis in the next sections, together with a discussion focused on the comparison between G79.29+0.46 and other galactic objects. Hence we discuss a preliminary comparison between magellanic and galactic objects and give a suggestion on how to extend this work.

The galactic cLBV G79.29+0.46

The multiwavelength approach adopted to study the LBVN around G79.29+0.46 allowed us to determine many physical properties related to the ejecta and the mass-loss experience of the star. In particular, analysis of interferometric and single-dish centimetric data has provided the physical conditions of the high-ionized gas. At an average distance of 0.8 pc from the star, there is, in fact, an ionized shell very likely in a torus-like configuration, seen face-on. Our analysis of the spectral index map revealed that the gas emits optically thin free-free radiation, even though a slight increase of the spectral index in some regions indicates the presence of density clumps (such the "spur-emission" in the north-east, observed for first time by Higgs, Wendker, & Landecker 1994) and interaction with the interstellar medium (i.e. the density clump observed at CO millimeter wavelengths in the south-west by Rizzo, Jiménez-Esteban, & Ortiz 2008). In support of this interaction, our high-resolution radio map shows brighter filaments in the south-west region that appear to frame the shocked clump.

Radio measurements also allowed us to determine the current-day mass-loss of the star ($\sim 1.4 \times 10^{-6}\,M_{\odot}yr^{-1}$) and the spectral index of the central object, which we find to be consistent with stellar wind (~ 0.8). With the assumption of optically thin nebula, we determined the ionized mass in the nebula ($\sim 3.5\,M_{\odot}$) and, from the UV flux, the spectral type for the star (B1-B0.5).

As discussed previously by other authors, the nebula of G79.29+0.46 also consists of dusty components, that emits in the mid-IR bands of the instrument IRAC and the far-IR of MIPS on board of *Spitzer*. The highest-resolution map obtained at EVLA permitted in this work, for first time, a detailed comparison with the infrared emission, revealing that actually the dusty components which are present in the nebula are different in nature. For instance, there is a warmer dust component (probed in the mid-IR), probably consisting of smaller grains, distributed in a shell inside the radio nebula, and a colder dust (probed in the far-IR) in two concentric bubbles (at a distance of 0.82 and 1.64 pc respectively). The second and outer shell discovered at 24 μm by Kraemer et al. (2009); Jiménez-Esteban, Rizzo, & Palau (2010) was attributed to a previous event of mass-ejection. We confirm this and also provide evidence for its detection at 70 μm, first through our re-processed MIPS image and then through the recent image obtained at 70 μm and 100 μm with the PACS instrument on board of *Herschel*.

By considering the measured flux densities obtained from the *Spitzer* and *Herschel* images, together with those obtained from archive data of the space telescope *ISO*, we have determined the temperature and the mass of the dust components. The warmer dust

is optically thin, has an average temperature of about $\sim 450\,\mathrm{K}$ and negligible mass. The colder dust, also optically thin, has an average temperature of $\sim 70\,\mathrm{K}$ and a mass at most of $\sim 3.3 \times 10^{-2}\,\mathrm{M}_{\odot}$. The resulting gas-to-dust ratio is 106, which is consistent with the galactic interstellar case.

The current-day mass-loss determined from the radio measurements can not explain the observed mass, meaning that the matter in this nebula was not ejected with average winds, but higher mass-loss rates must have occurred in the past, consistently with most of the known LBVs (η Car, AG Car, Pistol star). Because of these properties, we believe that G79.29+0.46 is a dormant LBV.

Our spectroscopic analysis of mid-IR *ISO* and *Spitzer* spectra shows that around G79.29+0.46 there are emission lines that are common in PDRs. Our shock-versus-PDR diagnostics confirms that these lines originate in physical and chemical conditions typical of PDRs. Moreover, we also performed electron density diagnostics as a function of the nebula radius. The average electron density $< 100\,\mathrm{cm}^{-3}$ is consistent with that ($\sim 73\,\mathrm{cm}^{-3}$) estimated from the the radio emission, concerning the region including the ionized shell. This reinforces the geometry assumed for the ionized gas distribution (a toroidal-shell with geometrical depth 0.29 pc) and, as a consequence, gives meaning to the estimated ionized mass. Conversely, electron densities estimated from the line-pairs next to the north-east nebula edge are higher ($\sim 200\,\mathrm{cm}^{-3}$). This higher density region corresponds to the radio "spur-emission". Our spectral index analysis of this region together with the density found here gives evidence of the presence of density clumps, likely not associated to G79.29+0.46.

Finally, adopting as input parameters the values found in this work, we modelled the star and the nebula emission of G79.29+0.46 with CLOUDY. As a result, we found that the star must have a luminosity $\log(\mathrm{L}/\mathrm{L}_{\odot})$ equal to 5.9.

The same approach used in this work but applied to other LBVs will provide us important clues useful to put strong constraints on massive star evolution. Moreover, in the case that other LBVNe present similar features, properties of such nebulae may be proposed as sufficient condition to be a star classified as LBV. In fact, it has been widely believed that related transition objects (OIafpe) are dormant LBVs, but because they are observed in the quiescent state it is not possible at the moment to give them the LBV classification.

G79.29+0.46 as template to identify new LBVs

Recent IR galactic plane surveys have discovered many circumstellar ejecta around massive stars (e.g., Carey et al. 2009; Gvaramadze, Kniazev, & Fabrika 2010; Mizuno et al. 2010; Wachter et al. 2010), increasing the number of candidate LBVs. However, most of

these sources must be yet classified or identified. These sources are usually sparse in the galactic plane and long term monitoring to observe possible S Dor variability would be expensive (Clark et al. 2012). An attempt to identify or classify LBVs could be, thus, to study their ejecta following the multiwavelength approach and comparing their properties with a good template of LBVN.

The number of LBVNe studied in details following this approach is still very limited. Similar works are those performed on IRAS 18576+0341 (Umana et al. 2005; Buemi et al. 2010), HR Car (Umana et al. 2009), HD168625 (Umana et al. 2010). Other LBVNe have been analysed, but often their nebular components have been singularly investigated by different authors, based possibly on different assumptions and making difficult the comparison between the observed properties.

G79.29+0.46 contains together features observed in other LBVNe. As a matter of fact, it is one among the known sources with multiple shells, evidence of different mass-loss episodes. Other galactic objects are: η Car, which is an unique object as yet and certainly not useful as template; AG Car, which show two nested, concentric shells (Nota et al. 1996a); Sher 25, with a ring of gas and bipolar outflows, but yet poorly studied.

G79.29+0.46 contains in its nebula different emitting components (ionized gas, two populations of dust, possible PDR and CO) observed in other LBVNe: for example, dust and gas have been observed in HR Car (White 2000; Umana et al. 2009), AG Car (Waters et al. 1998; White 2000), HD168625 (Umana et al. 2010). In respect to these sources, G79.29+0.46 has a mass-loss history more meaningful, with evidence that LBVs can lose matter different times and with impressive mass-loss episodes.

G79.29+0.46 has also evidence of a PDR, possibly associated to its ejecta. The presence of PDRs around LBVs has been poorly investigated as yet. The first investigation concerns the nebula of HR Car (Umana et al. 2009), where for first time low-excitation fine structure lines were observed.

Features found in G79.29+0.46 (multiple-shells, typical kinematical ages, observed mass and size, mass-loss rate, chemical composition rich in CN or CNO cycle products) may be searched in sources of the new IR catalogues and complemented with radio measurements, in order to identify new cLBVs. In this sense, G79.29+0.46 could be a good template of LBVN.

However, we admit that, despite these aspects, some physical parameters (e.g. mass, temperature) related to the nebula of G79.29+0.46 may be uncertain because of its location. We remind that strong interstellar emission contaminates the nebula flux densities in the radio and in the IR and affects our measurements.

LBVs in the LMC

In order to understand if the LBV phenomenon is independent of metallicity and if the observed nebular properties are similiar to galactic examples, we have started a study of LBVNe at the radio wavelengths in the LMC. In this work we presented a pilot study by observing and analysing the radio emission of four sources in the LMC (namely LBVs R127 and R143 and cLBVs S61 and S119). Thanks to its properties, radio emission can be used as a good probe of the ionized gas emission from a nebula around a hot star. This is important when one wants to determine the gas content to establish the total mass budget ejected during the LBV phase and to constrain stellar evolution models of very massive stars.

We performed ATCA observations at the centimetric wavelengths aimed at detecting the radio emission in these nebulae. These first observations allowed us to detect for first time the selected LBVs and cLBVs in the LMC. With the adopted ATCA configuration, we were able to resolve the nebula sizes, which span between 0.87 pc and 2.1 pc, depending on the sources. These values are consistent with those of galactic LBVNe (e.g., G24.73+0.69, G26.47+0.02, Clark et al. 2003; Umana et al. 2012). The radio nebulae show a very similar morphology to that observed in Hα. This similarity leads us to assume that the Hα emission is not affected by strong intrinsic extinction due to dust. We confirmed the irregular shape of the nebula around R143 also in the radio.

The average spectral indeces indicate in almost all the cases optically thin free-free emission. With this assumption, we have hence derived the ionized gas mass, which ranges from 0.8 to 1.5 $M_{\odot}$, small but still consistent with galactic LBVNe masses. With a second campaign of observations at ATCA, this time using higher-frequencies, we obtained high-resolution maps of three of these sources, which can be compared with the optical Hα *HST* images. We have hence derived extinction maps, in order to investigate the possibility of intrinsic extinction due to dust. We found again that such nebulae are not strongly extinguished by dust, but there is evidence of dust in both an optically thin configuration and/or density clumps in at least two sources.

Analysing the highest-resolution map, we discovered the presence in R127 of a recently formed ($\sim 10^3$ yr) shell close (0.13 pc) to the star (while the outer shell extends till 1.65 pc), which is evidence that R127 has recently suffered outbursts. This supports the spectroscopic and photometric variations analysed by Walborn et al. (2008) over the last 30 years, when the star has been observed in outburst at different times.

An upper limit for the current-day mass-loss rate was derived for each source and in general varies between $\sim 10^{-6} - 10^{-5} M_{\odot} yr^{-1}$. Comparing this mass-loss rate with

the derived kinematical ages (of the order of $\sim 10^4$ yr) we conclude that the observed nebula masses are compatible with masses formed by average winds. The only exception is R143, which needs a higher mass-loss rate to explain its mass.

Finally, we derived the spectral type for each source. For S119 and S61, which are classified as cLBVs, we found that the stars may be colder (B0.5-B1 and B2-B3 respectively) than observed (late O) at the end of the 70s by Walborn (1977). If this is true, it might indicate that these object are moving toward the active state, but only further spectroscopic observations can confirm this. Based on our analysis, R127 is B1, consistently with the last report by Walborn et al. (2008), which argued that the star has probably begun its decline toward the quiescent state. The spectral type for R143 (B2-B3) and its low mass-loss rate $< 7 \times 10^{-6}\,M_{\odot}yr^{-1}$ suggest that this star is also moving toward its minimum.

In contrast to G79.29+0.46 and other galactic objects, LBVNe in the LMC have been poorly observed as yet and data archives are lacking in IR spectroscopic and photometric data suitable for our multiwavelength analysis. However, our work can be the starting point for future observations in the IR, aimed at studying the dust component in such nebulae, at deriving the total nebula budget and at recovering the mass-loss history of these stars, analogous with the galactic examples (e.g. G79.29+0.46). For this reason, we have provided evidence for the feasibility of observations with ALMA, which is well-suited for resolving and detecting in the far-IR and sub-mm regimes the colder dust also in LBVNe at the distance of the LMC.

Differences and similarities between galactic and magellanic LBVs

The magellanic LBVNe in our sample appears to share nebular properties very similar to G79.29+0.46 and other galactic objects.

Nebula sizes in the LMC range from 0.59 to 1.90 pc, consistently with G79.29+0.46 (the outer shell is 1.64 pc from the star) and other galactic objects (for example, 0.8 pc for the nebula of AG Car[4], 0.26 for HR Car[5] and 2.2 for Wra 17-96[6]). Concerning only the ionized gas shells, the magellanic R127, S61 and S119 are bigger (up to 1.2 pc) than the ionized nebula of G79.29+0.46[7] (0.8 pc). They also show higher current-day mass-loss. These two facts are related to the stellar bolometric luminosity, as shown in Figure 5.14, which is a plot of the mass-loss rate versus the bolometric luminosity of the objects in our sample and of other sources taken from the literature.

[4] Voors et al. (2000).
[5] Voors et al. (1997); White (2000).
[6] Egan et al. (2002).
[7] In the assumption that the adopted distance for G79.29+0.46 is correct.

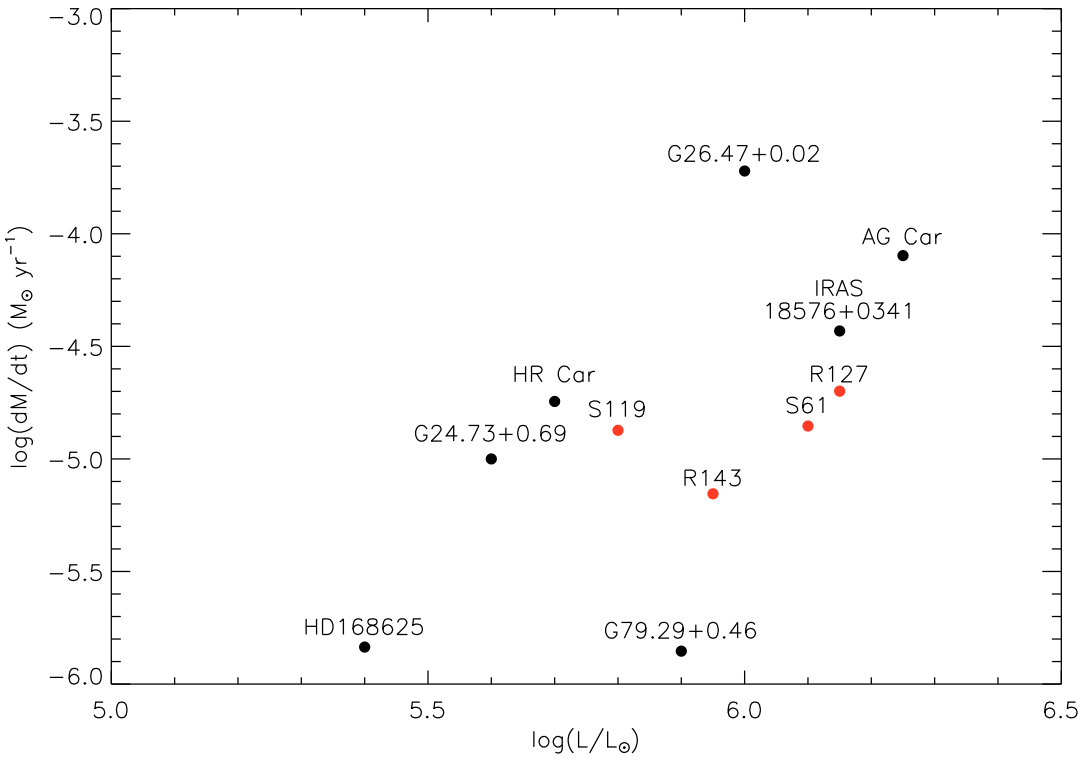

Figure 5.14: Current mass-loss rate versus bolometric luminosity. Red circles: magellanic objects. Black circles: galactic objects. Current mass-loss rates of G79.29+0.46, S61, R127, R143 as derived in this work; HD168625 from Umana et al. (2010); IRAS 18576+0341 (Umana et al. 2005); G26.47+0.02 (Umana et al. 2012), S119 (Crowther & Smith 1997). Luminosity: G79.29+0.46 (this work); HD168625 (Nota et al. 1996b); G26.47+0.02 (Clark et al. 2003); IRAS 18576+0341 (Humphreys & Davidson 1994); HR Car (Nota et al. 1995; Voors et al. 2000); R143 (Parker et al. 1993); R127 (Stahl et al. 1993; Davies, Oudmaijer, & Vink 2005); S119 (Crowther & Smith 1997); S61 (Wolf, Stahl, & Seifert 1987). Mass-loss rate and luminosity of: AG Car as in (Voors et al. 2000); G24.73+0.69 as in (Clark et al. 2003).

Kinematical ages are of the order of 10^4 yr and provide a lower limit for the LBV phase. In our sample, the youngest LBVNe is that of R143 while the oldest is that of S119, which appears to be dispersed and does not show ejecta formed recently.

G79.29+0.46 and R127 have strong evidence that they experienced outbursts different times, in analogy with other known LBVs (such as η Car, Sher-25). Timescales between these mass-loss episodes are of 2×10^4 yr (G79.29+0.46) and $\sim 5 \times 10^4$ yr (R127).

Almost all the nebulae which we considered are quite similar in geometry. R127 has an equatorial torus-like shell seen edge-on (proven through spectro-polarimetric studies by Schulte-Ladbeck et al. 1993; Davies, Oudmaijer, & Vink 2005). The ionized nebula of S61 and G79.29+0.46 are also consistent with this geometry, with the torus seen face-on. This geometry might be an indication that the shaping of such nebulae is not determined by the environment which hosts them, as R127 and S61 are located in a region devoid of nebulosity, while G79.29+0.46 is very likely immersed in a place rich in interstellar gas and dust. Conversely, the shape of the ejecta seems to be connected with the wind

direction. Equatorial ejecta indicate asymmetry in the mass-loss. However, this has been proven only in R127 (Schulte-Ladbeck et al. 1993) among the sources in our sample.

There is also evidence of slight differences between the magellanic and the galactic objects. For instance, the magellanic LBVNe considered in this work are smaller in mass (at most $\sim 1.5\,M_\odot$) than G79.29+0.46 ($\sim 3.5\,M_\odot$) and other galactic objects ($\sim 17\,M_\odot$, G26.47+0.02[8]; $8.9\,M_\odot$, AG Car[9]; $10\,M_\odot$, Wra 17-96[10]). Furthermore, the magellanic S61, S119 and R127 have current-day mass-loss rates ($\sim 10^{-5}\,M_\odot\,yr^{-1}$) larger than the galactic G79.29+0.46 ($\sim 10^{-6}\,M_\odot\,yr^{-1}$), but smaller in respect to the value derived in G26.47+0.02 ($\sim 10^{-4}\,M_\odot\,yr^{-1}$, Umana et al. 2012), needed to explain most of the galactic nebula masses. Moreover, we have derived that the magellanic sources (except R143) expelled mass with average winds, while G79.29+0.46 (together with other galactic LBVs) needed higher mass-loss rates than the current-day one to explain the formation of such a massive nebula. In Fig. 5.15 we represent the nebula mass and the current-day mass-loss rate of our sources plus other objects from the literature. Nebulae formed with average winds are linear with the mass-loss rate, while G79.29+0.46 and HD168625 must have expelled mass with mass-loss rates higher than that observed. However, we are conscious that both the parameters (nebula mass and mass-loss rate) strongly depend on the assumed distance ($M_{nebula} \propto D^3$ and $\dot{M} \propto D^{3/2}$) and that uncertainty of the distance is more important in galactic objects than those magellanic. As a consequence this comparison must be done with caution.

Evidences and implications of this work

Though the magellanic metallicity is not significantly different from that in our Galaxy and though we have studied only a sub-sample of LBVNe in the LMC, we conclude for the moment that properties of their ejecta are similar to those galactic.

The possibility that the LBV phenomenon occurs in the same way in different galaxies supports the theory that the bulk of LBVNe arises from mass-loss mechanisms which are independent of the metallicity (e.g., hydrodynamic explosions Humphreys & Davidson 1994; Smith & Owocki 2006). If this is true, then the LBV phenomenon may have a paramount importance in the evolution of galaxies (providing UV radiation, mechanical energy and processed material to the interstellar medium) and in the evolution of the early Universe (when massive stars were more numerous than in the present epoch). Moreover, since many galactic LBVs show evidence of dusty nebulae, they may have contributed

[8] Umana et al. (2012).
[9] Voors et al. (2000).
[10] Egan et al. (2002).

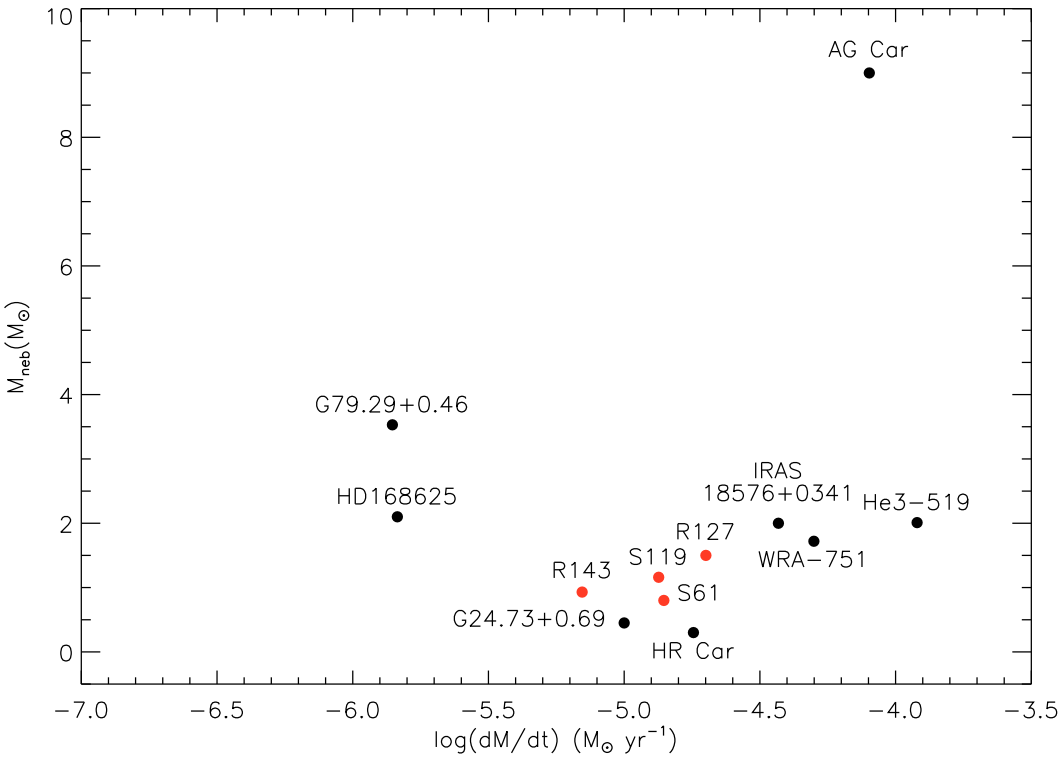

Figure 5.15: Nebula mass versus current-day mass-loss. Red circles: magellanic objects in this work. Black: galactic objects: G79.29+0.46 (this work); IRAS 18576+0341 (Umana et al. 2005; Buemi et al. 2010); HD168625 (Nota et al. 1996b; Umana et al. 2010); He3-519 (Duncan & White 2002; Smith, Crowther, & Prinja 1994); WRA-751 (Duncan & White 2002; Voors et al. 2000); AG Car (Voors et al. 2000); HR Car (Duncan & White 2002); G24.73+0.69 (Clark et al. 2003).

to the dust production in high-redshift galaxies, where the significant amount of dust observed is as yet unexplained.

To resolve these issues, observations of LBVNe in galaxies with different metallicities are needed.

Future work

Now that we have proven the feasibility of radio observations (with the ATCA) and sub-mm observations (with the upcoming ALMA, see Section 5.7), this work can be complemented with observation and analysis of the whole sample of LBVs in the LMC (which counts further 21 LBVs and cLBVs), following the multiwavelength analysis performed on G79.29+0.46. This will allow a better understanding of the mass-loss phenomenon during the LBV phase and to point out any differences in the magellanic and galactic sources.

This study can be extended also to other galaxies, such as M33 and M31, where other LBVs and cLBVs have been recently discovered with the space telescope *Herschel* (e.g.,

Clark et al. 2012). These recent observations can be complemented with investigation of both the free-free and the dust emissions, by using future generation of radiotelescopes, such as the upcoming ALMA and SKA.

Bibliography

Abbott D. C., Conti P. S., 1987, ARA&A, 25, 113

Agliozzo C., Umana G., Trigilio C., Buemi C., Leto P., Ingallinera A., Franzen T., Noriega-Crespo A., 2012, MNRAS, 426, 181

Albacete Colombo J. F., Flaccomio E., Micela G., Sciortino S., Damiani F., 2007, A&A, 464, 211

Arnett D., Meakin C., Young P. A., 2005, ASPC, 332, 75

Benaglia P., Vink J. S., Martí J., Maíz Apellániz J., Koribalski B., Crowther P. A., 2007, A&A, 467, 1265

Boffi F. R., Stanghellini L., 1994, A&A, 284, 248

Bohannan B., Walborn N. R., 1989, PASP, 101, 520

Bonanos, A. Z., Massa, D. L., Sewilo, M., et al. 2009, AJ, 138, 1003

Boyer M. L., et al., 2010, A&A, 518, L142

Brogan C. L., Gelfand J. D., Gaensler B. M., Kassim N. E., Lazio T. J. W., 2006, ApJ, 639, L25

Bromm V., Larson R. B., 2004, ARA&A, 42, 79

Buemi C. S., Umana G., Trigilio C., Leto P., Hora J. L., 2010, ApJ, 721, 1404

Carey S. J., et al., 2009, PASP, 121, 76

Castor J. I., Abbott D. C., Klein R. I., 1975, ApJ, 195, 157

Castor J. I., Lamers H. J. G. L. M., 1979, ApJS, 39, 481

Chevalier R. A., 1982, ApJ, 259, L85

Chevalier R. A., 1982, ApJ, 259, 302

Chiosi C., Maeder A., 1986, ARA&A, 24, 329

Clampin M., Nota A., Golimowski D. A., Leitherer C., Durrance S. T., 1993, ApJ, 410, L35

Clark B. G., 1980, A&A, 89, 377

Clark J. S., Egan M. P., Crowther P. A., Mizuno D. R., Larionov V. M., Arkharov A., 2003, A&A, 412, 185

Clark J. S., Larionov V. M., Arkharov A., 2005, A&A, 435, 239

Clark J. S., Castro N., Garcia M., Herrero A., Najarro F., Negueruela I., Ritchie B. W., Smith K. T., 2012, A&A, 541, A146

Clayton D. D., 1979, Ap&SS, 65, 179

Conti P. S., Frost S. A., 1976, BAAS, 8, 340

Cornwell T., Braun R., Briggs D. S., 1999, ASPC, 180, 151

Crowther P. A., Smith L. J., 1997, A&A, 320, 500

Crowther P. A., Lennon D. J., Walborn N. R., 2006, A&A, 446, 279

Dale D. A., et al., 2007, ApJ, 655, 863

Danforth C. W., Chu Y.-H., 2001, ApJ, 552, L155

Davidson K., Dufour R. J., Walborn N. R., Gull T. R., 1986, ApJ, 305, 867

Davies B., Oudmaijer R. D., Vink J. S., 2005, A&A, 439, 1107

Dayal A., Hoffmann W. F., Bieging J. H., Hora J. L., Deutsch L. K., Fazio G. G., 1998, ApJ, 492, 603

Draine B. T., 2003, ARA&A, 41, 241

Duncan R. A., White S. M., 2002, MNRAS, 330, 63

Fazio G. G., et al., 2004, ApJS, 154, 10

Feast M. W., Thackeray A. D., Wesselink A. J., 1960, MNRAS, 121, 337

Feast M. W., 1961, MNRAS, 122, 1

Feder J., Russell K. C., Lothe J., Pound G. M., 1966, AdPhy, 15, 111

Ferland G. J., Korista K. T., Verner D. A., Ferguson J. W., Kingdon J. B., Verner E. M., 1998, PASP, 110, 761

Frank A., Balick B., Davidson K., 1995, ApJ, 441, L77

Egan M. P., Clark J. S., Mizuno D. R., Carey S. J., Steele I. A., Price S. D., 2002, ApJ, 572, 288

Frew D. J., 2004, JAD, 10, 6

Gall C., Hjorth J., Andersen A. C., 2011, A&ARv, 19, 43

Giannini T., Nisini B., Lorenzetti D., 2001, ApJ, 555, 40

Gvaramadze V. V., Kniazev A. Y., Fabrika S., 2010, MNRAS, 405, 1047

Heger A., Fryer C. L., Woosley S. E., Langer N., Hartmann D. H., 2003, ApJ, 591, 288

Herrero A., Garcia M., Uytterhoeven K., Najarro F., Lennon D. J., Vink J. S., Castro N., 2010, A&A, 513, A70

Higgs L. A., Wendker H. J., Landecker T. L., 1994, A&A, 291, 295

Hora J. L., et al., 2004, SPIE, 5487, 77

Hora, J. L., Gutermuth, R. A., Carey, S. et al. 2010, in *Reionization to Exoplanets: Spitzer's Growing Legacy*, ASP Conf. Series, in press

Houck J. R., Shure M. A., Gull G. E., Herter T., 1984, ApJ, 287, L11

Humphreys R. M., Davidson K., 1984, Sci, 223, 243

Humphreys R. M., Davidson K., 1994, PASP, 106, 1025

Humphreys R. M., Davidson K., Smith N., 1999, PASP, 111, 1124

Hutsemekers D., 1997, ASPC, 120, 316

Jiménez-Esteban F. M., Rizzo J. R., Palau A., 2010, ApJ, 713, 429

Joss P. C., Salpeter E. E., Ostriker J. P., 1973, ApJ, 181, 429

Kochanek C. S., 2011, ApJ, 743, 73

Kotak R., Vink J. S., 2006, A&A, 460, L5

Kraemer, K. E., et al. 2009, Bulletin of the American Astronomical Society, 41, 467

Kraemer K. E., et al., 2010, AJ, 139, 2319

Krauss, M., Hanson, M., & Voors, R. H. M. 2000, Bulletin of the American Astronomical Society, 32, 1473

Lamers H. J. G. L. M., Snow T. P., Lindholm D. M., 1995, ApJ, 455, 269

Lamers H. J. G. L. M., et al., 1996, A&A, 315, L225

Lamers H. J. G. L. M., Nota A., Panagia N., Smith L. J., Langer N., 2001, ApJ, 551, 764

Lamers H. J. G. L. M., Nugis T., 2002, A&A, 395, L1

Lang C. C., Johnson K. E., Goss W. M., Rodríguez L. F., 2005, AJ, 130, 2185

Leitherer C., Robert C., 1991, ApJ, 377, 629

Liu X.-W., et al., 2001, MNRAS, 323, 343

Lucy L. B., 2007, A&A, 474, 701

Maeder A., 1983, A&A, 120, 130

Mallik D. C. V., Peimbert M., 1988, RMxAA, 16, 111

Mathis J. S., 1990, ARA&A, 28, 37

Meaburn J., 2001, ASPC, 233, 253

Mercer, A., Chizek, M., Lang, C. C., Figer, D. F., & Najarro, P. 2006, Bulletin of the American Astronomical Society, 38, 1046

Mill J. D., et al., 1994, JSpRo, 31, 900

Miroshnichenko A. S., et al., 2000, A&AS, 147, 5

Mizuno D. R., et al., 2008, PASP, 120, 1028

Mizuno D. R., et al., 2010, AJ, 139, 1542

Mizutani M., Onaka T., Shibai H., 2002, A&A, 382, 610

Moffat, A. F. J., Drissen, L., & Robert, C. 1989, IAU Colloq. 113: Physics of Luminous Blue Variables, 157, 229

Molinari, S., Swinyard, B., Bally, J., et al. 2010, PASP, 122, 314

Moorwood A. F. M., Baluteau J.-P., Anderegg M., Fitton B., Coron N., Biraud Y., 1980, ApJ, 238, 565

Morris P., Morris, Spitzer WRRINGS Team, 2008, IAUS, 250, 361

Morse J. A., Davidson K., Bally J., Ebbets D., Balick B., Frank A., 1998, AJ, 116, 2443

Munari U., et al., 2009, A&A, 503, 511

Najarro F., Hillier D. J., Stahl O., 1997, A&A, 326, 1117

Nazé Y., Rauw G., Hutsemékers D., 2012, A&A, 538, A47

Nota A., et al., 1994, cmls.conf, 89

Nota A., Livio M., Clampin M., Schulte-Ladbeck R., 1995, ApJ, 448, 788

Nota A., Clampin M., García-Segura G., Leitherer C., Langer N., 1996, swhs.conf, 398

Nota A., Pasquali A., Clampin M., Pollacco D., Scuderi S., Livio M., 1996, ApJ, 473, 946

Nota A., Smith L., Pasquali A., Clampin M., Stroud M., 1997, ApJ, 486, 338

Nota A., Pasquali A., Marston A. P., Lamers H. J. G. L. M., Clampin M., Schulte-Ladbeck R. E., 2002, AJ, 124, 2920

Paladini, R., Noriega-Crespo, A., Carey, S. J. et al. (in preparation)

Panagia N., 1973, AJ, 78, 929

Panagia N., Felli M., 1975, A&A, 39, 1

Parker J. W., Clayton G. C., Winge C., Conti P. S., 1993, ApJ, 409, 770

Pasquali A., Nota A., Clampin M., 1999, A&A, 343, 536

Pauldrach A. W. A., Puls J., 1990, A&A, 237, 409

Pottasch, S. R. 1984, *Planetary Nebulae: A Study of Late Stages of Stellar Evolution*, (Dordrecht: D. Reidel)

Puls J., Vink J. S., Najarro F., 2008, A&ARv, 16, 209

Rest A., et al., 2012, Natur, 482, 375

Rizzo J. R., Jiménez-Esteban F. M., Ortiz E., 2008, ApJ, 681, 355

Sault R. J., Teuben P. J., Wright M. C. H., 1995, ASPC, 77, 433

Schaller G., Schaerer D., Meynet G., Maeder A., 1992, A&AS, 96, 269

Schulte-Ladbeck R. E., Leitherer C., Clayton G. C., Robert C., Meade M. R., Drissen L., Nota A., Schmutz W., 1993, ApJ, 407, 723

Schuster M. T., Marengo M., Patten B. M., 2006, SPIE, 6270,

Sedlmayr E., 1994, LNP, 428, 163

Setia Gunawan D. Y. A., de Bruyn A. G., van der Hucht K. A., Williams P. M., 2003, ApJS, 149, 123

Simpson J. P., Colgan S. W. J., Cotera A. S., Erickson E. F., Hollenbach D. J., Kaufman M. J., Rubin R. H., 2007, ApJ, 670, 1115

Smith J. D. T., Rudnick L., Delaney T., Rho J., Gomez H., Kozasa T., Reach W., Isensee K., 2009, ApJ, 693, 713

Smith L. J., Crowther P. A., Prinja R. K., 1994, A&A, 281, 833

Smith L. J., 1997, ASPC, 120, 310

Smith L. J., Nota A., Pasquali A., Leitherer C., Clampin M., Crowther P. A., 1998, ApJ, 503, 278

Smith N., Davidson K., Gull T. R., Ishibashi K., Hillier D. J., 2003, ApJ, 586, 432

Smith N., Vink J. S., de Koter A., 2004, ApJ, 615, 475

Smith N., 2005, MNRAS, 357, 1330

Smith N., 2006, ApJ, 644, 1151

Smith N., Owocki S. P., 2006, ApJ, 645, L45

Smith N., 2008, ASPC, 388, 129

Smith N., Chornock R., Li W., Ganeshalingam M., Silverman J. M., Foley R. J., Filippenko A. V., Barth A. J., 2008, ApJ, 686, 467

Smith N., 2011, BSRSL, 80, 322

Smith N., Li W., Silverman J. M., Ganeshalingam M., Filippenko A. V., 2011, MNRAS, 415, 773

Schneider N., Bontemps S., Simon R., Jakob H., Motte F., Miller M., Kramer C., Stutzki J., 2006, A&A, 458, 855

Stahl O., 1986, A&A, 164, 321

Stahl O., Wolf B., Klare G., Cassatella A., Krautter J., Persi P., Ferrari-Toniolo M., 1983, A&A, 127, 49

Stahl O., Wolf B., 1986, A&A, 158, 371

Stahl O., Mandel H., Wolf B., Gaeng T., Kaufer A., Kneer R., Szeifert T., Zhao F., 1993, A&AS, 99, 167

Stahl O., Jankovics I., Kovács J., Wolf B., Schmutz W., Kaufer A., Rivinius T., Szeifert T., 2001, A&A, 375, 54

Sterken C., van Genderen A. M., Plummer A., Jones A. F., 2008, A&A, 484, 463

Tielens A. G. G. M., Hollenbach D., 1985, ApJ, 291, 722

Traficante A., et al., 2011, MNRAS, 416, 2932

Trams N. R., Waters L. B. F. M., Voors R. H. M., 1997, ASPC, 120, 351

Trams N. R., Voors R. H. M., Waters L. B. F. M., 1998, Ap&SS, 255, 195

Umana G., Buemi C. S., Trigilio C., Leto P., 2005, A&A, 437, L1

Umana G., Buemi C. S., Trigilio C., Hora J. L., Fazio G. G., Leto P., 2009, ApJ, 694, 697

Umana G., Buemi C. S., Trigilio C., Leto P., Hora J. L., 2010, ApJ, 718, 1036

Umana G., Buemi C. S., Trigilio C., Leto P., Hora J. L., Fazio G., 2011a, BSRSL, 80, 335

Umana G., Buemi C. S., Trigilio C., Leto P., Agliozzo C., Ingallinera A., Noriega-Crespo A., Hora J. L., 2011b, ApJ, 739, L11

Umana G., Ingallinera A., Trigilio C., Buemi C. S., Leto P., Agliozzo C., Noriega-Crespo A., Flagey N., Paladini R., Molinari S., 2012, MNRAS, *in press*

van Boekel R., et al., 2003, A&A, 410, L37

van Dyk S. D., 2005, ASPC, 332, 47

van Genderen A. M., 2001, A&A, 366, 508

van Loon J. T., et al., 2010, AJ, 139, 68

Vink J. S., de Koter A., Lamers H. J. G. L. M., 1999, A&A, 350, 181

Vink J. S., 2000, PhDT,

Vink J. S., de Koter A., Lamers H. J. G. L. M., 2000, A&A, 362, 295

Vink J. S., de Koter A., 2002, A&A, 393, 543

Vink J. S., 2008, NewAR, 52, 419

Vink, J. S., de Koter, A., & Kotak, R. 2008, Mass Loss from Stars and the Evolution of Stellar Clusters, 388, 47

Vink, J. S., Drew, J. E., Steeghs, D., Wright, N. J., Martin, E. L., Gänsicke, B. T., Greimel, R., & Drake, J. 2008, MNRAS, 387, 308

Vink J. S., 2009, arXiv, arXiv:0905.3338

Vink J. S., 2011, Ap&SS, 336, 163

Voors R. H. M., Waters L. B. F. M., Trams N. R., Kaeufl H. U., 1997, A&A, 321, L21

Voors R. H. M., Geballe T. R., Waters L. B. F. M., Najarro F., Lamers H. J. G. L. M., 2000, A&A, 362, 236

Wachter S., Mauerhan J. C., Van Dyk S. D., Hoard D. W., Kafka S., Morris P. W., 2010, AJ, 139, 2330

Walborn N. R., 1976, ApJ, 204, L17

Walborn N. R., 1977, ApJ, 215, 53

Walborn N. R., 1982, ApJ, 256, 452

Walborn N. R., et al., 2008, IAUC, 8913, 1

Walborn, N. R., Stahl, O., Gamen, R. C., et al. 2008, ApJL, 683, L33

Waters L. B. F. M., Izumiura H., Zaal P. A., Geballe T. R., Kester D. J. M., Bontekoe T. R., 1996, A&A, 313, 866

Waters L. B. F. M., Morris P. W., Voors R. H. M., Lamers H. J. G. L. M., Trams N. R., 1998, Ap&SS, 255, 179

Weiler K. W., Panagia N., Montes M. J., Sramek R. A., 2002, MmSAI, 73, 1144

Weis K., 2003, A&A, 408, 205

Weis K., Duschl W. J., Bomans D. J., 2003, A&A, 398, 1041

Weis K., 2008, cihw.conf, 183

Weis K., 2011, BSRSL, 80, 440

Wendker H. J., Higgs L. A., Landecker T. L., 1991, A&A, 241, 551

Wendker H. J., Higgs L. A., Landecker T. L., 1994, AGAb, 10, 35

Wendker H. J., Molthagen K., Heske A., Higgs L. A., Landecker T. L., 1998, Ap&SS, 255, 187

Werner M. W., et al., 2004, ApJS, 154, 1

White S. M., 2000, ApJ, 539, 851

Wolf B., Stahl O., Seifert W., 1987, A&A, 186, 182

Wolf B., Stahl O., Smolinski J., Casatella A., 1988, A&AS, 74, 239

Wolf B., 1989, ASSL, 157, 91

Wolf B., 1989, A&A, 217, 87

Young P. A., Meakin C., Arnett D., Fryer C. L., 2005, ApJ, 629, L101

Zacharias N., Monet D. G., Levine S. E., Urban S. E., Gaume R., Wycoff G. L., 2005, yCat, 1297, 0